Development and characterization of low affinity glutamate fluorescent indicators

Inaugural-Dissertation

zur Erlangung des Doktorgrades
der Mathematisch-Naturwissenschaftlichen Fakultät
der Heinrich-Heine-Universität Düsseldorf

vorgelegt von

Kateryna Ryndia

aus Kyjiw, Ukraine

Jülich, Februar 2023

aus dem Institut für Biologische Informationsprozesse 1 (IBI-1)
des Forschungszentrums Jülich
und der Mathematisch-Naturwissenschaftlichen Fakultät
der Heinrich-Heine-Universität Düsseldorf

Gedruckt mit der Genehmigung der
Mathematisch-Naturwissenschaftlichen Fakultät der
Heinrich-Heine-Universität Düsseldorf

Berichterstatter:

1. Referent: Prof. Dr. Christoph Fahlke
2. Korreferent: Prof. Dr. Michael Bott

Tag der mündlichen Prüfung: 05. Juni 2023

“In the middle of difficulty lies opportunity”

Albert Einstein

Dedicated to my family

Contents

Abbreviations

Å	Angstrom
ABC	ATP-binding cassette
ADP	Adenosine diphosphate
Ala (A)	Alanine
ALS	Amyotrophic lateral sclerosis
AMPA	α-amino-3-hydroxy-5-methyl-4-isoxazolepropionic acid
Arg (R)	Arginine
Asp (D)/ Asp^-	Aspartic acid/ Aspartate
ATP	Adenosine triphosphate
BNPI	Brain-specific Na^+-dependent inorganic phosphate transporter
Ca^{2+}	Calcium
Cl^-	Chloride
CNS	Central nervous system
cp	Circularly permuted
Cys (C)	Cysteine
Da	Dalton
DEBP	Aspartate/glutamate binding protein
DMSO	Dimethylsulfoxide
DNA	Deoxyribonucleic acid
DTT	Dithiothretiol
E. coli	Escherichia Coli
EAAT	Excitatory amino acid transporter
eGFP	Green fluorescent protein
EM	Energy minimization
EOS	Glutamate optical sensor
FRET	Förster resonance energy transfer
g	Gram
GABA	γ-aminobutyrate
GEGI	Genetically encoded glutamate indicator
GLT	Glutamate transporter
Glu (E)/ Glu^-	Glutamic acid/ Glutamate
GluBP	Bacterial periplasmic aspartate/glutamate binding protein
H^+	Hydrogen
His (H)	Histidine
IANBD ester	N-((2-(iodoacetoxy)ethyl)-N-methyl)amino-7-nitrobenz-2-oxa-1,3-diazole
iGluR	Ionotropic glutamate receptors
IRF	Instrument response function
K	Kelvin

K^+	Potassium
Kan	Kanamycin
kg	Kilogram
l	Liter
Leu (L)	Leucine
M	Molar mass
m	Meters
m-/µ-/n-/p-	Mili-/micro-/nano-/pico-
MD	Molecular dynamics
Met (M)	Methionine
mGluR	Metabotropic glutamate receptors
MS	Mass
Mut	Mutant
Na^+	Sodium
NBD	7-nitrobenz-2-oxa-1,3-diazol-4yl
NMDA	N-methyl-D-aspartate
NPT	Isothermal-isobaric ensemble
P	Pressure
PAG	Phosphate-activated glutaminase
PBP	Periplasmic binding protein
PCR	Polymerase chain reaction
P_i	Inorganic phosphate
RMSD	Root mean square deviation
RT	Room temperature
s	Seconds
SEM	Standard error of the mean
Ser (S)	Serine
SLC	Solute carriers
SLMV	Synaptic-like microvesicles
SNARE	Soluble N-ethylmaleimide sensitive fusion protein attachment receptor
SV	Synaptic vesicle
T	Temperature
TCSPC	Time-correlated single-photon counting
Thr (T)	Threonine
Tyr (Y)	Tyrosine
V	Volts
V-ATPase	Vacuolar H^+-ATPase
VAChT	Vesicular acetylcholine transporter
VEAT	Vesicular excitatory amino acid transporter
VGAT	Vesicular GABA transporter
VGLUT	Vesicular glutamate transporter
VMAT	Vesicular monoamine transporter

VNUT	Vesicular nucleotide transporter
VPAT	Vesicular polyamine transporter
WT	Wild type
xCT	Glutamine-cysteine exchanger
ΔpH	H^+ gradient
ΔΔG	Gibbs free energy difference
$\Delta\mu H^+$	Electrochemical proton gradien
Δψ	Membrane potential
[]	Concentration

List of figures

List of tables

Abstract

L-Glutamate is an intermediate of primary metabolism and the predominant excitatory neurotransmitter in the vertebrate central nervous system. It is crucial for maintaining normal brain function and contributes to the pathophysiology of various neuropsychiatric diseases. Vesicular glutamate transporters (VGLUTs) harness the electrochemical proton gradient generated by primary active H^+-ATPases to accumulate glutamate inside the synaptic vesicle, permitting the regulated glutamate release from the presynaptic terminal through exocytosis. Glutamate concentration in synaptic vesicles have a significant impact on the strength of glutamatergic synapses. Whereas various genetically encoded nanosensors were developed to detect local concentration changes in the synaptic and perisynaptic space, sensors that report on glutamate accumulation inside synaptic vesicles are still missing. Since synaptic vesicles exhibit an acidic lumen and since glutamate accumulation is associated with changes of cation and anion concentrations, such a sensor needs to have a pH-, cation- and anion-unaffected affinity to glutamate. Moreover, low affinity is required to report on high mM concentrations in synaptic vesicles.

To engineer and characterize a glutamate sensor capable of following glutamate accumulation in synaptic vesicles, I combined molecular dynamics (MD) simulations with protein biochemistry and fluorescence spectroscopy. Through atomistic MD simulations of the bacterial periplasmic aspartate/glutamate binding protein *ybeJ*, I studied ligand binding to the sensory domain and its interaction with Na^+ / K^+ ions. Computational results suggested that glutamate binding is salt-independent. Using the fast-switching alchemical transformations method, I predicted mutants that significantly decrease the affinity to glutamate (T91V and T92V).

In order to test the predictions of these simulations, low affinity variants of the novel glutamate fluorescent sensor Fl-GluBP (Fl-GluBP-T91V and Fl-GluBP-T92V) were expressed, purified, fluorescently labeled with IANBD ester and tested by steady-state fluorescence spectroscopy. Such experiments revealed that the Fl-GluBP-T92V variant has a K_d for glutamate of ~ 120 mM and is virtually pH-, Na^+- and K^+- independent. Additional glutamate binding kinetics studies and fluorescence lifetime measurements for this variant showed a small fluorescence dynamic range that makes it unsuited for absolute glutamate concentration measurements inside synaptic vesicles. Despite this, the Fl-GluBP-T92V sensor currently represents the best candidate for following the time course of glutamate accumulation inside

synaptic vesicles. The use of Fl-GluBP-T91V variant (K_d of ~ 49 mM) in synaptic vesicles is impaired by its pH-dependent affinity to glutamate. However, its wide fluorescence dynamic range, glutamate affinity at pH 7.5 and salt stability, qualifies it for the direct quantification of absolute glutamate levels in neuronal cytoplasm. For this, the selectivity between aspartate and glutamate must be improved.

Altogether, in this thesis I have engineered a glutamate fluorescent biosensor: Fl-GluBP-T92V, which may lead to new insights and better understanding of vesicular glutamate accumulation and refilling dynamics. Additionally, I proposed Fl-GluBP-T91V as a promising candidate sensor for future absolute glutamate measurements inside the neuronal cytoplasm.

Zusammenfassung

L-Glutamat ist ein Zwischenprodukt des Primärstoffwechsels und der wichtigste exzitatorische Neurotransmitter im zentralen Nervensystem von Wirbeltieren. Es ist notwendig für die Aufrechterhaltung einer normalen Gehirnfunktion und spielt in der Pathophysiologie verschiedener neuropsychiatrischer Erkrankungen eine wichtige Rolle. Vesikuläre Glutamattransporter (VGLUTs) nutzen den elektrochemischen Gradienten für Protonen, der durch primär aktive H^+-ATPasen erzeugt wird, um Glutamat in synaptischen Vesikeln zu akkumulieren, und ermöglichen so die regulierte Glutamatfreisetzung aus dem präsynaptischen Terminal durch Exozytose. Die Glutamatkonzentration in den synaptischen Vesikeln hat einen erheblichen Einfluss auf die Stärke der glutamatergen Synapsen. Während verschiedene genetisch kodierte Nanosensoren entwickelt wurden, um lokale Konzentrationsänderungen im synaptischen und perisynaptischen Raum zu erfassen, fehlen Sensoren, mit denen man der Glutamatakkumulation in synaptischen Vesikeln folgen kann. Da synaptische Vesikel ein saures Lumen aufweisen und die Glutamatakkumulation mit Änderungen der Kationen- und Anionenkonzentration einhergeht, muss ein solcher Sensor eine pH-, kationen- und anionenunabhängige Affinität zu Glutamat aufweisen. Außerdem ist eine geringe Affinität erforderlich, um hohe Konzentrationen in synaptischen Vesikeln zu erfassen.

Um einen Sensor für Glutamat im synaptischen Vesikel zu entwickeln und zu charakterisieren, habe ich Molekulardynamiksimulationen (MD) mit Proteinbiochemie und Fluoreszenzspektroskopie kombiniert. Durch atomistische MD-Simulationen des bakteriellen periplasmatischen Aspartat/Glutamat-bindenden Proteins *ybeJ* untersuchte ich die Ligandenbindung an die sensorische Domäne und ihre Interaktion mit Na^+ / K^+-Ionen. Meine Ergebnisse zeigen, dass die Glutamatbindung salzunabhängig ist. Mit Hilfe schneller alchemistischer Transformationen habe ich Mutanten vorhergesagt, die die Affinität zu Glutamat verringern (T91V und T92V).

Um die Vorhersagen dieser Simulationen zu testen, wurden Varianten des neuartigen Glutamat-Fluoreszenzsensors Fl-GluBP (Fl-GluBP-T91V und Fl-GluBP-T92V) mit niedriger Affinität exprimiert, gereinigt und mit IANBD-Ester fluoreszenzmarkiert und durch stationäre Fluoreszenzspektroskopie getestet. Diese Experimente zeigten, dass die Fl-GluBP-T92V-Variante einen K_d-Wert für Glutamat von ~ 120 mM hat und praktisch pH-, Na^+- und K^+-unabhängig ist. Zusätzliche Studien zur Glutamatbindungskinetik und Messungen der

Fluoreszenzlebensdauer zeigten einen geringen dynamischen Fluoreszenzbereich, der für die Messung absoluter Glutamatkonzentration in synaptischen Vesikeln nicht ideal ist. Allerdings scheint der Fl-GluBP-T92V-Sensor der beste Sensorkandidat, um die Glutamatakkumulation im synaptischen Vesikel zu beschreiben, zu sein. Die Fl-GluBP-T91V-Variante (Kd von ~ 49 mM) weist einen breiten dynamischen Fluoreszenzbereichs, eine Glutamataffinität bei pH 7,5 und eine Salzstabilität auf, die die direkte Quantifizierung der absoluten Glutamatspiegel im neuronalen Zytoplasma möglich machen. Allerdings muss die Selektivität zwischen Aspartat und Glutamat noch verbessert werden.

Zusammenfassend habe ich in dieser Arbeit einen fluoreszierenden Glutamat-Biosensor entwickelt, Fl-GluBP-T92V, der in der Lage ist, die Glutamatakkumulation in synaptischen Vesikeln zu beschreiben, was zu neuen Erkenntnissen und einem besseren Verständnis der Dynamik der vesikulären Glutamatakkumulation und -auffüllung führen kann. Darüber hinaus habe ich mit Fl-GluBP-T91V einen vielversprechenden Sensor-Kandidaten für absolute Glutamatmessungen im neuronalen Zytoplasma identifiziert.

Chapter 1. Introduction

1.1 Glutamate

L-Glutamate (L-Glu) is an anionic form of dicarboxylic glutamic acid (Figure 1.1) [1]. It is synthesized in the human body and thus classified as a non-essential amino acid. Glutamate together with aspartate, γ-aminobutyrate (GABA), glycine and D-serine carries a neurotransmitter function in the vertebrate central nervous system (CNS) [2].

More than 80 years ago the ubiquitous distribution of glutamate amino acid in the mammalian brain was discovered. Initially glutamate was assumed to serve only metabolic function [3]. Later work reported [4] that levels of extracellular glutamate are tightly regulated allowing glutamate to function as the major excitatory neurotransmitter in the CNS. In addition to its main role, glutamate also serves as a metabolic precursor to GABA (main inhibitory neurotransmitter) [5, 6], a source of energy and ammonia [7] and is a component of the antioxidant glutathione and polyglutamated folic acid [8]. Changes in glutamate and GABA metabolism may play important roles in the control of cortical excitability.

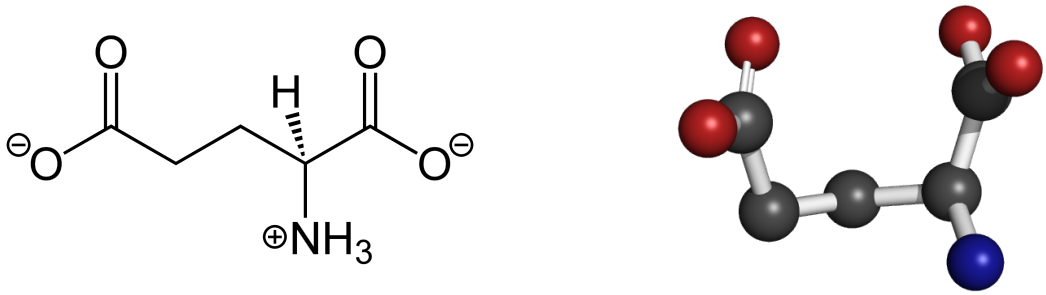

Figure 1.1. L-glutamate molecule. Skeletal formula (left) and a ball-and-stick model (right). From [9, 10].

Nowadays, it is universally recognized that glutamate is broadly distributed not only within the human body but in all living beings as a building block for protein. Brain tissue contains the biggest amount of glutamate (5-15 mmol/kg [11]) that is mostly found in more than 80 % of all neurons [12]. Therefore, glutamate is involved in various cognitive (learning and memory), emotional and endocrine processes, and plays an important role in several human motor system pathways. Metabolic studies have reported that almost all the glucose that enters the CNS is eventually converted to glutamate [13].

1.2 Glutamatergic neurotransmission

All tissues within living organisms depend on intercellular chemical signals. One of the most important signaling processes between cells is carried in the brain.

Communication between neurons in the central nervous system occurs by the combination of electrical and chemical signals through the microscopic gaps (~ 20 nm wide [14]) called synaptic clefts. To cross the synaptic cleft, the electrical signal is converted into a chemical one, which is rapid (occurring in ms) and tightly regulated [15]. This conversion happens when the depolarization of the presynaptic neuron opens voltage-activated Ca^{2+} channels allowing Ca^{2+} influx. The increase of intracellular [Ca^{2+}] triggers the fusion of neurotransmitter-filled vesicles with the cellular membrane with the consequent release of neurotransmitters into the synaptic cleft, where they bind to receptors on the postsynaptic surface [16, 17]. Activated receptors allow ions to flow across the cell membrane generating postsynaptic electrical signals (Figure 1.2). Excitatory (glutamate and aspartate) neurotransmitters lead to a postsynaptic influx of cations that causes postsynaptic depolarization. Ligand-gated channel receptors that are permeable to positive ions are called excitatory. In turn, inhibitory neurotransmitters (GABA, glycine) activate Cl^--selective ion channels causing Cl^--influx into the postsynaptic cell and thus hyperpolarizes the neuron. Receptors that are permeable to anions are called inhibitory [18]. The energy-costly glutamatergic neurotransmission requires multiple regulatory processes, high levels of glucose and oxygen consumption [5].

1.3 Synaptic Vesicles

Signal transduction between neurons at chemical synapses involves the release of neurotransmitters, their diffusion across the synaptic cleft and binding to postsynaptic receptors. Under resting conditions, neurotransmitters are stored inside small spherical organelles (r ~ 20 nm), called synaptic vesicles (SVs), in the cytoplasm of the nerve terminal [19]. SVs play a key role in synaptic transmission, as they are responsible for neurotransmitters' storage and release.

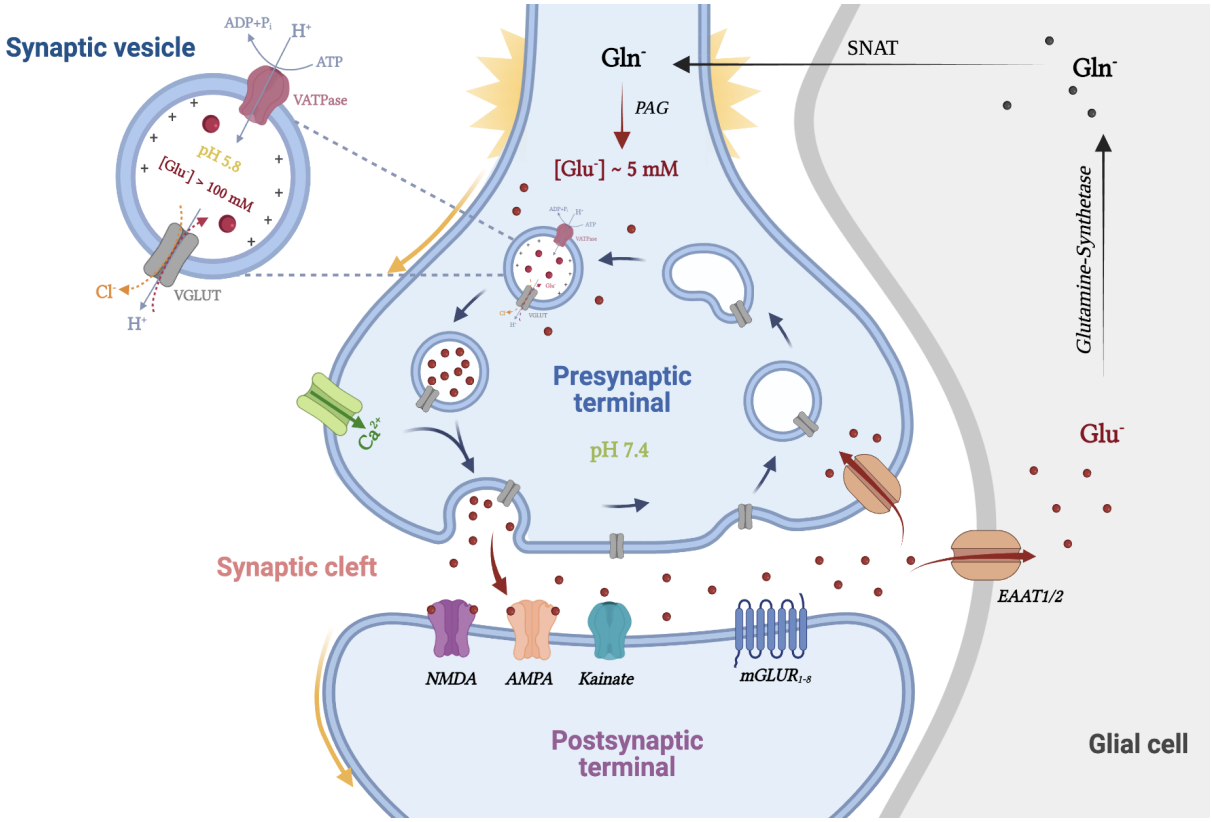

Figure 1.2. Schematic diagram of excitatory neurotransmission at a glutamatergic synapse. Under normal physiological conditions, glutamate is synthesized from glucose or glutamine in the presynaptic space and is stored inside the synaptic vesicles. Ca^{2+} influx triggers the synaptic vesicles fusion with the presynaptic membrane with the following glutamate release into the synaptic cleft and its binding to postsynaptic receptors. EAATs also play an important role in glutamate clearance and glutamate transport inside the glial cells, where it is metabolized to glutamine and transported back to the neurons. The scheme is created with BioRender.com by modifying [5, 20, 21].

1.3.1 Synaptic Vesicle Recycle

Membrane depolarization and following Ca^{2+} influx initiate neurotransmitter release from presynaptic nerve terminals via exocytosis of synaptic vesicles. SV exocytosis is mediated by SNARE proteins [22] and proceeds in 3 steps: docking, priming and fusion (Figure 1.3) [23]. During the docking step SVs are prepared for synaptic exocytosis and connected to the active zone. Priming is the ATP-dependent process, by which vesicles become fusion competent waiting to respond to a Ca^{2+} triggering signal. At the moment, when the action potential depolarizes the presynaptic membrane, Ca^{2+} channels open and increase $[Ca^{2+}]$ at the active zone with the following glutamate release [24]. After exocytosis the synaptic vesicle membrane is rapidly retrieved by endocytosis (mediated by clathrin [23]) and reused for the formation of

a synaptic vesicle, which will be refilled by neurotransmitters for a new round of exocytosis [25]. This cycle can be repeated many times.

The vesicle refilling process is energy-dependent, driven by the primary active of H^+-ATPase (V-ATPase) and carried out via the activity of vesicular glutamate transporters (VGLUTs) [20] (see more in chapter 1.3.4). The electrochemical gradient ($\Delta\mu H^+$) across the vesicle membrane that is required for the transport of neurotransmitters into the synaptic vesicle acidifies the vesicular lumen to ~ pH 5.8 [26]. At the beginning of SV recycling, there is no proton gradient, and the pH value is around 7.3 [27]. The re-acidification cycle continues ~ 15 seconds [26], which is in agreement with time courses of glutamate refilling into SVs obtained in experiments at the calyx of Held [28].

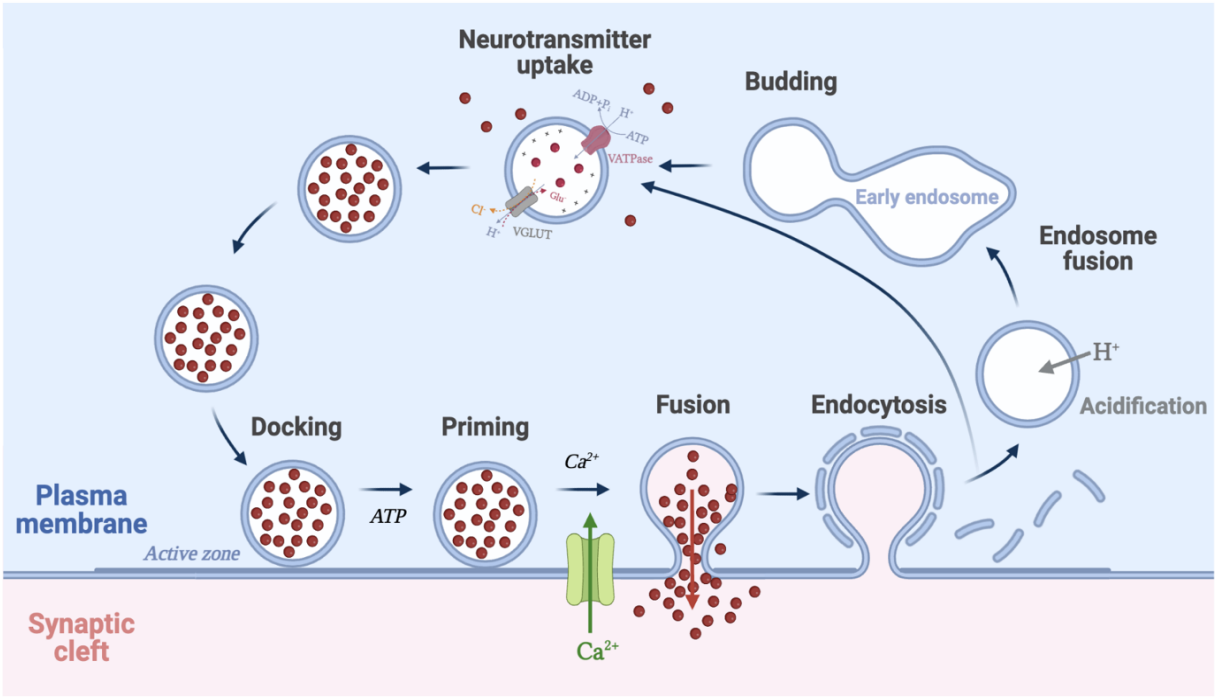

Figure 1.3. The synaptic vesicle recycling pathway. After docking and priming in the active zone, vesicles fuse to the membrane under a Ca^{2+} trigger and release glutamate into the synaptic cleft. After exocytosis new synaptic vesicles are re-endocytosed, recycled directly or via early endosome and refilled with neurotransmitters for another round. Scheme is created with BioRender.com from [23, 24].

1.3.2 The Synaptic Vesicle Composition

The protein composition of SV was successfully analyzed by mass spectrometry (MS) by Takamori et al. in 2006 [19]. They found that a typical SV contains 70 synaptobrevins, 32 synaptophysins, 9-14 neurotransmitter transporters, 10 Rab3As, 8 synapsins, 15 synaptotagmin and 1 V-ATPase. Also, it was reported that the vesicular membrane is ~ 4 nm thick and consists

of phospholipids and a high amount of cholesterol (~ 40 %). The inner volume of an average vesicle is 19.86 × 10^{-21} l, corresponding to approximately 1790 molecules of glutamate at a luminal concentration of 150 mM, that is almost 10 times higher than the cytoplasmic glutamate concentration (~ 10 - 15 mM) [29–31]. Earlier studies of immunoisolated synaptic vesicles from rat cerebral cortex and rat medulla oblongata concluded that not only glutamate, but also GABA and glycine are major amino acid neurotransmitters stored in synaptic vesicles [32].

1.3.3 Vesicular Glutamate Transporters

Different glutamate transporters families are involved in the glutamatergic signaling pathway, they include the vesicular glutamate transporters (VGLUTs), the plasma membrane excitatory amino acid transporters (EAATs) and the glutamate-cysteine exchanger [21, 33].

Vesicular glutamate transporters (VGLUTs) together with vesicular excitatory amino acid transporter (VEAT) and vesicular nucleotide transporter (VNUT) are members of the family of solute carrier 17 (SLC17) that transport anionic neurotransmitters such as glutamate inside the synaptic vesicle. The SLC18 (VMATs, VAChT, VPAT) and SLC32 (VGAT) families transport cationic neurotransmitters and GABA, respectively [34]. Three isoforms of mammalian VGLUTs have been identified: VGLUT1 (SLC17A7), VGLUT2 (SLC17A6) and VGLUT3 (SLC17A8) [35]. VGLUT1 was cloned as brain-specific Na^+-dependent inorganic phosphate transporter (BNPI) in 1994 [29, 36] and later found to serve as vesicular glutamate transporters [37]. Subsequently, additional VGLUTs that share ~ 75 % sequence identity with each other were identified and got their name in order of discovery [38, 39].

The vesicular glutamate transporters have very different properties from other glutamate transporters. VGLUTs exhibit strict selectivity and do not recognize D-, L-aspartate and glutamine as a substrate [40]. VGLUTs are characterized by exclusive distribution patterns in the brain with very limited overlap. VGLUT1 was found to be strongly expressed in neurons in the cerebral cortex, hippocampus and cerebellar cortex (regions associated with a low release probability), while VGLUT2 was detected mostly in subcortical regions (high release probability). VGLUT3, by contrast to two predominant isoforms, is mostly expressed in non-glutamatergic neurons. Lately, after the broad examination of VGLUTs distribution, it was revealed that VGLUT1/2 could also be expressed in non-glutamatergic neurons [29] as well as in synaptic-like microvesicles (SLMVs) in astrocytes [41].

1.3.4 Glutamate filling of SV's and acidification

Glutamate accumulation in SVs requires an energy-dependent mechanism. ATP provides the energy for generating an electrochemical proton gradient across the vesicle membrane ($\Delta\mu H^+$) via V-ATPases. $\Delta\mu H^+$ is composed of the luminal positive membrane potential ($\Delta\psi$) and the H^+ gradient (ΔpH) [42]. ATPase converts cytosolic ATP into ADP, P_i and H^+, which are then transported into the vesicle lumen and generate a strong positive potential $\Delta\psi$ and a small ΔpH between the vesicular lumen and the cytoplasm. The transport of different transmitters appears to utilize distinct components of $\Delta\mu H^+$. Cationic transmitters depend on the chemical component ΔpH, whereas glutamate uses the electrical component $\Delta\psi$ as the main driving force [34]. Whether VGLUTs operate as Glu^-/H^+ exchangers [27], Glu^-/Cl^- exchangers [43, 44], or as an electrogenic Glu^- uniporter [35] is still under debate, but the contribution of the luminal H^+ to $\Delta\psi$ component and synaptic vesicles filling with glutamate is clear.

As this process is electrogenic, it requires a charge balance for the V-ATPase. Luminal Cl^- functions as a counter ion and buffer H^+ ions allowing proton accumulation inside the vesicle, simultaneously participating in the acidification process. Activation of glutamate uptake in synaptic vesicles occurs at ~ 4 mM of Cl^- [44, 45]. High $[Cl^-]$ dissipates the $\Delta\psi$ component and increases ΔpH that inhibits vesicular glutamate accumulation [46, 47]. The estimated $\Delta\psi$ of typical secretory vesicles is 50-100 mV [34].

1.3.5 VGLUTs as K^+, P_i and Cl^- ions transporters

Additionally to VGLUTs main role as glutamate transporters, they could also transport Cl^-, P_i and K^+ ions [48]. Cl^- transport in SVs is quite controversial and proposes two main theories on how Cl^- is regulated in synaptic vesicles: via the Cl^-/H^+ exchanger (e.g., ClC) or it is mediated by VGLUT itself. A fair amount of recent studies proved VGLUTs (but not CICs) may represent the major Cl^- permeation pathway in glutamatergic synaptic vesicles [49, 50]. Phosphate transport inside the synaptic vesicle occurs in a Na^+ - coupled manner by using $\Delta\mu H^+$ as a driving force, but with a lower affinity than to glutamate. In the plasma membrane it is coupled to the co-transport of 2 Na^+ ions [51]. In contrast, phosphate and glutamate transport have significant differences: 1. VGLUTs demonstrate activity in phosphate transport in the absence of Cl^- [52]; 2. the transport of phosphate is not stimulated in the plasma membrane by the presence of H^+ [53]. VGLUTs also display a K^+/H^+ antiport mode. Exchange of luminal H^+ with cytosolic K^+ decrease ΔpH allowing more H^+ ions enter inside the vesicle, therefore increasing $\Delta\psi$ component and stimulating glutamate uptake [54] (Figure 1.4, left).

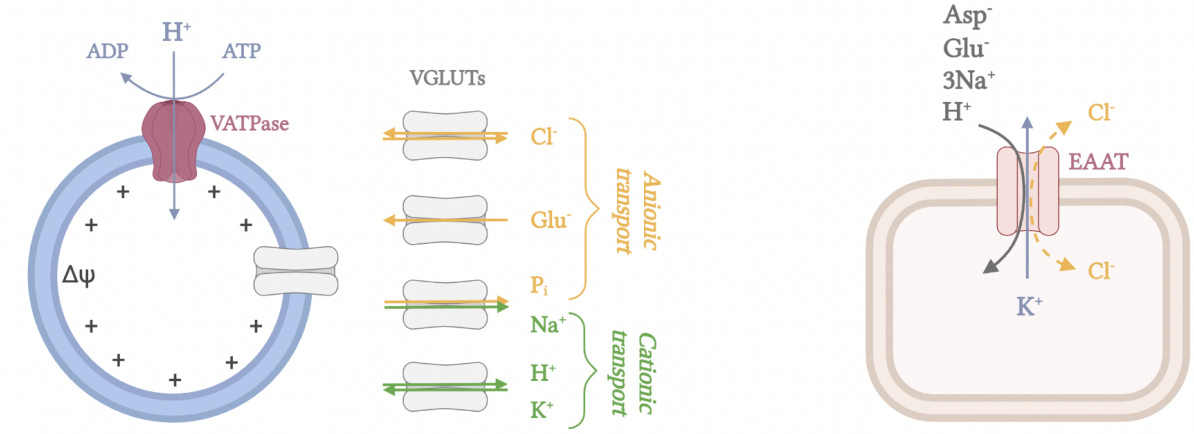

Figure 1.4. VGLUTs as ions transporter and EAATs stoichiometry of ion-flux coupling. (left) In addition to glutamate, VGLUTs also transport Cl^-, P_i and K^+ ions in different modes. (righ) EAATs glutamate transport is associated with the cotransport of 3 Na^+ and 1 H^+ accompanied by the countertransport of 1 K^+. Scheme is created with BioRender.com from [21, 48].

1.4 Glutamate clearance

Overstimulation of postsynaptic glutamate receptors leads to neurotoxicity and neurodegeneration. Therefore, glutamate has to be quickly and efficiently removed from the synaptic cleft. Such transport processes reduce resting glutamate concentrations in the extracellular space naturally to very low values (~ 3 µM [55]).

1.4.1 Excitatory Amino Acid Transporters

Glutamate clearance from the synaptic cleft is the main task of excitatory amino acid transporters (EAATs). EAATs bind glutamate and maintain extracellular glutamate concentrations below excitotoxic levels by transporting the neurotransmitter into neighboring glial cells and neurons [12, 56]. They belong to the SLC1 family of transporters and have five subtypes (EAAT1-5) [57]. Rodent versions of EAAT1 and EAAT2 are, respectively, GLAST1 and GLT1 [58, 59]. Glutamate transport by EAAT1-3 is coupled to the cotransport of 3 Na^+ and 1 H^+ ions followed by the countertransport of 1 K^+ ion (Figure 1.4, right), while the mechanism of coupling for EAAT4,5 has not been determined and just supposed to have the same ratio [40]. Additionally, EAATs have an uncoupled Cl^- flux through the transporter [60]. In glial cells glutamate is metabolized to glutamine by the glutamine synthetase and then transported again into excitatory neurons. Here the phosphate-activated glutaminase (PAG) converts it back into glutamate, which is then transported into the synaptic vesicle by VGLUTs [61].

EAAT1 is highly abundant in brain cerebellum, EAAT2 is the major glutamate transporter in all other brain regions, while EAAT3 has nearly 100-fold less expression than EAAT1,2 and is mostly concentrated in the hippocampus, cerebellum and basal ganglia. In turn, EAAT4 expression is highly localized in Purkinje cells of the cerebellum and EAAT5 is expressed in the retina. These glutamate transporters were detected also in a number of other organs, for example heart, kidney and placenta [62–67].

1.4.2 Glutamate-cysteine exchanger

Another type of transporter is glutamine-cysteine exchanger (xCT, SLC7A11) [68]. This transporter acts as a cysteine transporter using the transmembrane gradient of glutamate as driving force. xCT exchanges glutamate and cysteine in a 1:1 relationship [69]. Thus, extracellular glutamate inhibits cysteine uptake, while cysteine uptake causes glutamate release.

It is supposed that xCT could be a major source of extracellular glutamate [70, 71]. Therefore, this topic has been actively studied during the last years, demonstrating that xCT expression correlates with aggressiveness, chemoresistance and stem cells features in glioblastoma (GBM), where it provokes glutamate-associated neuronal cell death and tumor-associated epilepsy [72–74]. Its upregulation was also demonstrated in lymphomas, gliomas and pancreatic cancers [75, 76].

1.4.3 Glutamate receptors

As soon as glutamate has been released into the synaptic cleft, it binds to receptors that are located on neuronal and glial cells. Glutamate receptors are the most abundant in the brain and could be divided into two categories: ionotropic (iGluRs: AMPA-, NMDA- and Kainate) and metabotropic (mGluR1-8). The distribution of these receptors differs. iGluRs are located in the core of the synapse opposing the release site, while mGluRs are located at the border of the synapse [77, 78].

NMDA- and AMPA- types of ionotropic glutamate receptors are ligand-gated ion channels that depend on cation flux (K^+, Ca^{2+} and Na^+). They act on millisecond timescales to mediate the fast synaptic transmission. NMDA receptors have higher glutamate affinity than AMPA, while the last have faster kinetics. Glutamate acting on NMDA- and AMPA receptors highly contributes to cell death, epilepsy, traumatic brain injury and perinatal asphyxia [79].

In contrast, metabotropic receptors activate or inhibit second messenger systems via interactions with trimeric G-protein. mGluRs respond much slower with much longer-lasting physiological effects and modulate synaptic activity and plasticity [5, 40].

1.5 Glutamate in health and neurodegeneration

Glutamate plays a crucial role for normal brain functions such as neuronal differentiation, migration and survival in the developing brain and is involved in synaptic plasticity, motor activity, cognitive, emotional and endocrine functions [1]. At the same time, glutamate raises great interest among neurologists because of its contributions to the pathophysiology of various acute or chronic neurodegenerative processes.

Synaptic plasticity and strength have long been considered important mechanisms involved in learning, memory and development in neural circuits [80, 81]. Synaptic plasticity is defined by the changes that occur at synapses during the exocytotic release upon stimulation, so it controls how effectively neurons communicate between each other. Synaptic strength is the "volume" of such communication. Its extent depends on the amount of neurotransmitter released upon stimulation or on postsynaptic changes such as AMPA receptors expression [82, 83]. Consequently, the strength of glutamatergic synapses critically depends on glutamate concentrations in synaptic vesicles.

High glutamate concentrations in brain tissue can cause neuronal cell death. This effect was firstly observed by Lucas and Newhouse [84] and later was named "excitotoxicity" by Olney [85, 86]. Since the end of the 19-th century [87] glutamate excitotoxicity has been inseparably linked to acute neurological disorders, such as cerebral ischemia [88], traumatic brain injury [89] and other CNS pathologies. Chronic overexcitation of neurons by glutamate is associated with neurodegenerative processes in amyotrophic lateral sclerosis (ALS) [90, 91], Huntington's and Parkinson's diseases [92–96], as well as Alzheimer's dementia [97]–[100].

Dysregulation in glutamate signaling in the CNS is a key factor in the invasion and growth of glioblastoma, whose cells release high level of glutamate into the extracellular matrix and trigger neuronal cell death. Therefore, glutamate is a crucial mediator of glioma-associated epileptic seizures [101, 102].

The modulation of glutamate packaging into synaptic vesicles, caused by the loss in VGLUTs expression, stress or psychotropic drugs, results in destructive neuropsychiatric effects such as psychosis, schizophrenia and anxiety disorders [103–106].

Altogether, glutamate is involved in various neurodegenerative processes in the CNS either due to the alteration of receptor functions, excessive release or reduced uptake. Although many clinical studies were held to overcome the state of excitotoxicity, results have been poor and did not bring a lot of success [91, 97]. Scientists are still limited in diagnostic tools for a complete understanding of glutamate roles in pathophysiology and for providing novel treatment strategies.

1.6 Glutamate concentration measurements by fluorescent biosensors

Glutamate is not only of crucial importance for normal chemical communication in the nervous system of vertebrates, but the dysregulations in glutamate homeostasis also contribute to the pathophysiology of various neurodegenerative processes. However, despite its prominent role, there are still insufficient methods to visualize its dynamics and to measure its amount in living tissues.

Extracellular glutamate concentrations firstly were measured *in situ* by the microdialysis technique [107, 108], which appears not suitable for detecting rapid local glutamate concentration changes and shows poor signal-to-noise ratio. To study glutamate concentrations with higher spatial and temporal resolution, non-invasive glutamate optical sensors (EOSs) were developed. They could be spread into two groups: chemically labeled sensors and genetically encoded glutamate indicators (GEGIs). Both types are based on a glutamate-binding protein and are either labeled with a synthetic fluorophore or fused to a fluorescent protein [109].

The first generation of EOSs was represented by hybrid sensors, which were composed of a glutamate-binding core of an AMPA receptor coupled to a small molecule dye. They suffered from low refolding yield and stability. After extensive engineering, the enhanced glutamate optical sensor (eEOS) was reported. It demonstrates a wide dynamic range (> 2400 %), good photostability, pH insensitivity and high glutamate selectivity, but is not ratiometric [110]. Therefore, genetically encoded indicators based on fluorescent proteins (such as GFP), which may be easily targeted to specific cellular populations and may be delivered by relatively non-invasive techniques (viral infection or transgenesis) arise great interest [111, 112].

The generation of fluorescent glutamate biosensors, based on the bacterial periplasmic glutamate/aspartate binding protein (GluBP), which shares structural homology with AMPAR S1S2 [113] appears very perspective (Figure 1.5). First glutamate binding kinetic measurements of GluBP were based on tryptophan fluorescence changes, that is suitable as an indicator of the

conformational changes, but not of the binding action [114]. However, this type of glutamate indicator has become the basis for the set of GEGIs based on Förster resonance energy transfer (FRET) between two fluorescent proteins fused to the two protein termini: FLIPE [115], GluSnFR and SuperGluSnFR [116]. This group had small conformational change in GluBP during glutamate binding, therefore low FRET efficiency [117]. The substantial improvements were detected in a single - wavelength glutamate sensor iGluSnFR, whose separated fragments of GluBP were fused at each terminus of the circularly permuted green fluorescent protein (cpEGFP). iGluSnFR demonstrates a high fluorescence dynamic range with a K_d to glutamate of ~ 4 μM that allows the measurement of glutamate in a variety of tissues [109]. Variants of iGluSnFR ($iGlu_f$, $iGlu_u$, $iGlu_h$, $iGlu_m$, $iGlu_l$) [112], [114], [116] display diverse kinetic mechanisms and cover a broad range of affinities to glutamate (within 137 μM – 50 mM range).

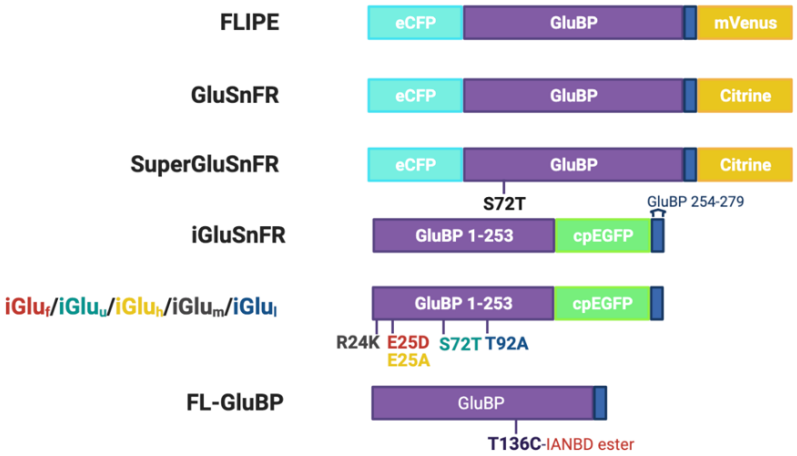

Figure 1.5. Structures of genetically encoded and chemically labeled glutamate indicators. Modified from [116].

Fl-GluBP was generated by targeted Cys substitution of GluBP (T136C) and following labeling with a synthetic fluorophore IANBD ester. Such a sensor exhibits a ~ 20-fold higher K_d to glutamate than GluBP with a 2.9-fold larger fluorescence enhancement upon glutamate binding [114]. It has a two-step fluorescent kinetic mechanism in which rapid glutamate binding is followed by isomerization. The rate of isomerization, which is saturated at 2220 s^{-1}, makes such sensor potentially suitable for real-time glutamate tracking at single synapses under high frequency stimulation. Moreover, Fl-GluBP demonstrates high selectivity for glutamate (K_d = 10.6 μM) over aspartate (K_d = 184 μM) and glutamine (K_d = 896 μM).

1.7 The aim of this study

This work aims at optimizing fluorescence glutamate sensor Fl-GluBP [114] to follow glutamate accumulation inside the synaptic vesicle. Since synaptic vesicles exhibit an acidic lumen [27] and since glutamate accumulation is associated with changes of cation and anion concentrations inside the synaptic vesicle [48], such a sensor needs to be unaffected by luminal pH and ions concentration. To report on high mM glutamate concentration inside the synaptic vesicle [19], low affinity is required.

In order to engineer such a sensor according to the listed requirements, the combination of atomistic molecular dynamics simulations together with the alchemical transformation method is used to study glutamate binding to the sensory domain, to shed light on its interaction with Na^+/K^+ ions and to predict mutants that could decrease the affinity to glutamate. Theoretically predicted fluorescently labeled derivatives can be experimentally tested with steady state and time-resolved fluorescence spectroscopy and fluorescent lifetime measurements.

1.8 Glutamate binding protein (GluBP)

The ATP-binding cassette (ABC) transporter system is one of the largest and one of the oldest known protein superfamilies in both prokaryotic and eukaryotic organisms. This system uses the ATP binding and hydrolysis to drive substrate transport across cell membranes. There are 48 ABC transporters in humans, and 80 in the gram-negative bacteria *Escherichia coli*. The ABC transporter of gram-negative bacteria consists of three components: a periplasmic binding protein (PBP), which traps and transports ligands through the membrane into the periplasmic space; an integral membrane protein complex for providing the transmembrane pathway; and two cytoplasmic nucleotide-binding domains that use ATP hydrolysis to drive the transport reaction (Figure 1.6, A). PBPs are the best studied component and are responsible for ligand specificities in the ABC system [118–120].

The first protein that was able to bind both glutamate and aspartate (DEBP) was purified from *E. coli* K12 and has a molecular weight near 31 kDa. It has only one ligand binding site for L-glutamate and L-aspartate, but not for L-glutamine or L-asparagine [121]. The sensory domains of all modern fluorescence sensors for *in vitro/in vivo* glutamate binding kinetics measurements are based on this protein sequence (ybeJ or gltI) [114–116].

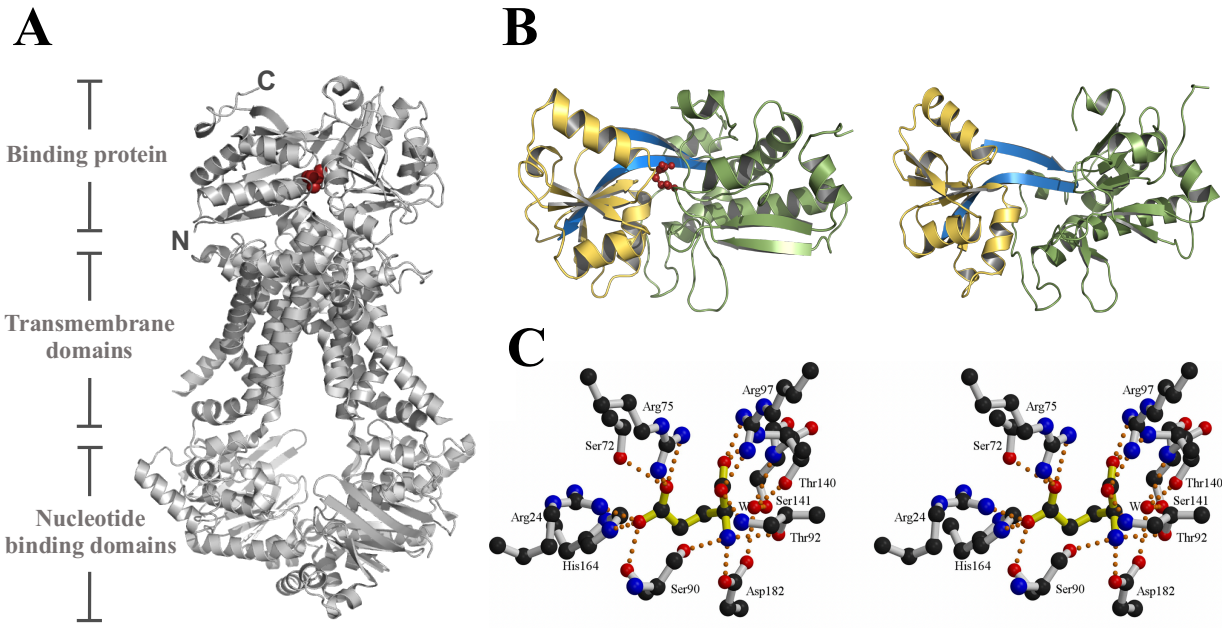

Figure 1.6. Structure of the periplasmic aspartate/ glutamate binding protein (GluBP). The overall structure of the ABC transporter of the $ModB_2C_2A$ complex, downloaded from the Protein Data Bank with an ID: 2ONK. Glutamate binding protein is coupled with one Glu molecule represented by red balls. (B) GluBP structure (PDB ID: 2VHA) in two conformational states: ligand-bound closed (left) and open ligand-free (right), with the domain I and II colored green and yellow, respectively. (C) The stereo view of the glutamate binding site. The bound glutamate is colored yellow. The residues in the proximity to glutamate and supposed to be involved in the glutamate binding process. The water molecule closest to the ligand is labeled W. Taken from [122].

The crystal structure of the L-glutamate/ L-aspartate binding protein from *Shigella flexneri* (*sf*DEBP) complexed with one glutamate molecule was refined at an atomic resolution of 1 Å and reported in 2008 [122] (Figure 1.6, B). It only differs in Ala5 from *E.coli* DEBP, where this residue is replaced with a valine. The final model contains an asymmetric unit with two DEBPs, 730 water and 2 Tris molecules. The single peptide chain of one DEBP molecule consists of two domains and is formed by 279 amino acids. A glutamate molecule, which was identified inside the cleft between the two domains, binds to both of them forming 13 hydrogen bonds with the protein. In the ligand-DEBP interaction residues from various protein groups are involved: positively charged (Arg24, Arg75, and Arg97) and negatively charged (Asp182) side chains, neutral polar side chains (Ser90, Thr92 and His164), and main-chain carbonyl (Ser90) and amide (Thr92 and Thr140) groups (Figure 1.6, C). Each domain contains central five-stranded β-sheet surrounded by several α-helices. Domain I is the largest and represented by residues 3-105 and 215-279 providing the majority (10 out of 13) of the protein-ligand interactions, while domain II is formed by residues 118-208.

Upon the ligand binding process, the protein could adopt two conformational states: open ligand-free form or ligand-bound closed state. These ligand-mediated conformational changes are in essence of fluorescence protein sensors and are used to couple ligand binding processes to fluorescence intensity changes. Structure is available in the Protein Data Bank (PDB ID: 2VHA) for *in silico* studies of protein dynamics.

1.9 The environmentally sensitive fluorophore IANBD ester

IANBD ester or NBD iodoacetate ester (N-((2-(iodoacetoxy)ethyl)-N-methyl)amino-7-nitrobenz-2-oxa-1,3-diazole) is an environment-sensitive fluorophore (Figure 1.7). After reaction with thiol groups, which in proteins are present in cysteine residues, this compound exhibits significant fluorescence, which is highly sensitive to protein conformational changes. Moreover, because of the relatively low abundance of cysteine residues in mammalian proteins, thiol-reactive labeling appears the most preferred approach for the detection of protein conformational changes [123] and ligand-binding processes [124].

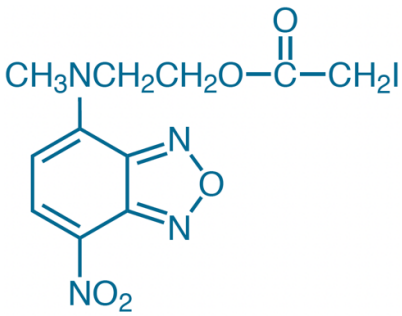

Figure 1.7. Chemical structure of IANBD ester fluorophore. From [124].

Compounds with an NBD (7-nitrobenz-2-oxa-1,3-diazol-4yl) skeleton belongs to the solvatochromic fluorescent dyes class. They generate a single emission band, which changes its position and sometimes intensity in response to the environment polarity and hydration changes [125]. However, NBD derivatives are characterized by a very weak fluorescence solvatochromism, weak fluorescence in water (lifetime is ~1 ns), but strong fluorescence in organic solvents, membranes (lifetime is ~ 7 ns) or hydrophobic environment [126, 127]. NBDs small size and absorption around 480 nm make this fluorophore convenient for biological applications. They have been widely studied [128] and used for various applications in biochemistry and chemical biology, e. g. in constructing FRET-based glucose sensors [129], in quantifying the hydrophobic thickness of a membrane protein [130] or in the measurement of temperature in living cell using NBD as an “optical thermometer” [131].

Chapter 2. Materials and Methods

2.1 Computational methods

Proteins are complex objects which have the greatest diversity of functions in all living organisms and are performed by a large range of length and time scales motions [132]. They are actively used for engineering diagnostic tools, such as biosensors for different compounds [110, 133–135]. Discussed in this work, glutamate biosensor Fl-GluBP is based on GluBP protein, which in turns undergoes conformational changes upon glutamate binding that is essential for its function (see chapter 1.6 and 1.8). Therefore, a clear understanding of protein structure and dynamics is highly important for understanding its function. Unfortunately, there are no experimental techniques available to provide connection between structure and dynamics at atomic resolution and physiologically relevant time scales, leaving computational methods, in particular Molecular Dynamics (MD) the only tool to study this regime [136].

2.1.1 MD simulations

Classical MD simulations are the most common computational technique for biomolecular systems research over nanoseconds to microseconds time scales. For protein and nucleic acid dynamics studies, this method was firstly applied in the 1970s [137] and since then is widely used for the investigation of conformational dynamics of biological macromolecules [138].

The molecular dynamics simulation is a trajectory-based approach, which involves the computation of the coordinates and velocities of the atoms as a function of time [139]. Considering that the system contains N particles (atoms or specific chemical groups) of mass m_i (i = 1…N), velocity $\vec{v}_i$ and position $\vec{r}_i$, the evolution of the microscopic configuration of the system at a certain time t can be determined. For this we have to integrate Newton's second law of motion for all atoms [140]:

$$\vec{F}_i = m_i \frac{d^2\vec{r}_i(t)}{dt^2} \tag{2.1}$$

where $\vec{F}_i$ is the total force acting on particle i and can be defined as:

$$\vec{F}_i = -\frac{\partial U_N\left(\vec{r}_i(t), \ldots, \vec{r}_N(t)\right)}{\partial \vec{r}_i(t)} \tag{2.2}$$

$U_N\left(\vec{r}_i(t), \ldots, \vec{r}_N(t)\right)$ is the potential energy.

The aim of this numerical integration is to find an expression that defines positions $\vec{r}_i(\mathrm{t} + \delta\mathrm{t})$ at time t + δt in terms of the already known positions at time t. The time increment δt corresponds to the "time-step" between two states of MD simulations. For this purpose, the velocity-Verlet algorithm is commonly used [141]. Then, the basic equation for the new position and velocity at time t + δt one can get:

$$\vec{r}_i(\mathrm{t} + \delta\mathrm{t}) \approx \vec{r}_i(\mathrm{t}) + \vec{v}_i(\mathrm{t})\delta\mathrm{t} + \frac{\vec{F}_i(\mathrm{t})}{2m_i}\delta t^2 \tag{2.3}$$

and

$$\vec{v}_i(\mathrm{t} + \delta\mathrm{t}) \approx \vec{v}_i(\mathrm{t}) + \frac{\vec{F}_i(\mathrm{t})}{2m_i}\delta\mathrm{t} + \frac{\vec{F}_i(\mathrm{t} + \delta\mathrm{t})}{2m_i}\delta t^2 \tag{2.4}$$

where $\vec{F}_i(\mathrm{t} + \delta\mathrm{t})$ is calculated for $\vec{r}_i = \vec{r}_i(\mathrm{t} + \delta\mathrm{t})$, *i*=1…N, defined in eq. 2.3.

For time-reversible motion, when t → -t, similarly we will write:

$$\vec{r}_i(\mathrm{t} - \delta\mathrm{t}) \approx \vec{r}_i(\mathrm{t}) - \vec{v}_i(\mathrm{t})\delta\mathrm{t} + \frac{\vec{F}_i(\mathrm{t})}{2m_i}\delta t^2 \tag{2.5}$$

Then by adding equations (2.3) and (2.5) we obtain:

$$\vec{r}_i(\mathrm{t} + \delta\mathrm{t}) \approx 2\vec{r}_i(\mathrm{t}) + \vec{r}_i(\mathrm{t} - \delta\mathrm{t}) + \frac{\vec{F}_i(\mathrm{t})}{m_i}\delta t^2 \tag{2.6}$$

Consequently, velocities could be generated by using:

$$\vec{v}_i(\mathrm{t}) \approx \frac{\vec{r}_i(\mathrm{t} + \delta\mathrm{t}) - \vec{r}_i(\mathrm{t} - \delta\mathrm{t})}{2\delta\mathrm{t}} \tag{2.7}$$

Alternatively, the less-trivial but the most popular leap-frog algorithm for describing the evolution of coordinates and velocities could be used too. It is the modification of Verlet algorithm and is given by [142]:

$$\vec{v}_i\left(\mathrm{t}+\frac{\delta \mathrm{t}}{2}\right) \approx \vec{v}_i\left(\mathrm{t}-\frac{\delta \mathrm{t}}{2}\right)+\frac{\vec{F}_i(\mathrm{t})}{2m_i}\delta \mathrm{t} \tag{2.8}$$

$$\vec{r}_i(\mathrm{t}+\delta \mathrm{t}) \approx \vec{r}_i(\mathrm{t})+\vec{v}_i\left(\mathrm{t}+\frac{\delta \mathrm{t}}{2}\right)\delta \mathrm{t} \tag{2.9}$$

The advantage of this integration scheme is that the velocity appears explicitly. Instead, the Verlet algorithm gives the velocity at the same time step as the position without additional calculations. Thus, it is just a question of preferences.

The most time-consuming step in classical MD simulations is calculations of the forces, which describe the interaction (potential) energies between atoms. There are multiple force fields available and each one is optimized for specific conditions and classes of molecules. But all of them use the same way to determine the potential energy of a system from which forces are calculated. Generally, force field function is a sum of all contributions from bonded (bond lengths, bond angles and sometimes improper dihedrals and torsional dihedral angles) and non-bonded (Van der Waals and electrostatic Coulomb) interactions. The energy function is given here [143]:

$$U(\vec{r}) = \sum U_{bonded}(\vec{r}) + \sum U_{non-bonded}(\vec{r}) =$$

$$= U_{bonds} + U_{angles} + U_{dihedrals} + U_{imp.torsion} + U_{LJ} + U_{Coulomb} =$$

$$= \sum_{i,j}^{bonds} k_b\,(r_{ij} - r_o)^2 +$$

$$+ \sum_{i,j,k}^{angles} k_\varphi\,(\varphi_{ijk} - \varphi_o)^2 +$$

$$+ \sum_{i}^{dihedrals} k_\phi\,(1 + \cos(n\phi_i - \delta)) +$$

$$+ \sum_{i,j,k,l}^{imp.torsion} k_\psi\,(\psi_{ijkl} - \psi_o)^2 +$$

$$+\sum_{i}^{N}\sum_{j=i+1}^{N}\left\{4\varepsilon_{ij}\left[\left(\frac{\sigma_{ij}}{r_{ij}}\right)^{12}+\left(\frac{\sigma_{ij}}{r_{ij}}\right)^{6}\right]+\frac{q_i q_j}{4\pi\varepsilon_0\varepsilon_r r_{ij}}\right\} \quad (2.10)$$

In eq. (2.10), the first term models the interaction of covalently bonded atoms in a molecule as a simple harmonic function describing oscillation about an equilibrium bond length r_0 with bond constant k_b. The second term, which describes the bond bending energy, is defined for every triplet of bonded atoms and is describing oscillation about an equilibrium angle φ_0 with force constant k_φ. In turn, the dihedrals energy is defined for every 4 sequentially bonded atoms, where ϕ_i is the angle of rotation about the covalent bond between the middle two atoms and the potential; n is the non-negative integer constant, which defines periodicity and δ is the phase shift. The improper torsion potentials are defined for a group of 4 atoms, where the central one is connected to the 3 peripheral atoms forming a pyramid. The dihedral angle ψ_0 is the angle between planes. This potential is used to keep structure planar. The last contribution is a double summation over neighbor atoms, which could belong to the same or different molecule, but always separated by at least 3 bonds. The Van der Waals interactions are modeled as a Lennard-Jones potential, where the first term describes the repulsive component and the second is represented by attractive forces. In the equation, σ_{ij} is the Van der Waals radius, the distance at which the intermolecular potential between two particles is zero; ε_{ij} is the well depth, the measure of interaction strength. The second term in summation is the electrostatic term, which is represented by the Coulomb energy, where r_{ij} is the distance between two atoms with charges q_i and q_j, ε is the dielectric constant. Usually, for biomolecular simulations, AMBER, CHARMM, GROMOS and OPLS force fields are widely used [140].

When molecular dynamic simulations of biological macromolecules are performed in explicit solvent, particles move without limits, causing some surface effects [144]. In order to minimize edge and size effects, it is common and important to apply periodic boundary conditions (PBC). When they are applied, the simulation box is replicated in all spatial directions forming an infinite lattice. During the simulations, when a molecule moves inside the central box, the same movements are reproduced in the neighboring boxes. In case this molecule leaves the central box, then one of its images will enter through the opposite side. The advantage of this technique is that there are no physical walls and surface molecules, and it requires to save coordinates and velocities of molecules belonging to only one of the boxes.

2.1.1.1 Simulation system

Molecular dynamics simulations for this study were performed in the GROMACS 2019.6 software package [145] using the AMBER99SB-ILDN force field [146] together with the improved Joung ion parameters [147]. For soluble free glutamate amino acid, the Horn parametrization adapted to the AMBER force field form was used [148].

The bacterial periplasmic aspartate/glutamate binding protein (DEBP) structure in a complex with L-glutamate molecule described in [122] was downloaded from the protein data bank (PDB ID: 2VHA) [10]. The initial asymmetric unit of the cell contains 2 DEBP molecules, as well as 730 water and 2 Tris molecules derived from the buffer of crystallization. The final model used in this work consists of only one DEBP (a single peptide chain of 279 amino acid residues) with a glutamate molecule for the bound or without for apo (unbound) state studies.

The working system was centered in a cubic box at least 1.2 nm from the box edge to satisfy the minimum image convention, since we used periodic boundary conditions. The box was filled with water by using the SPC/E three-point water model [149] together with two/three Cl^- ions for bound/unbound conformational states to maintain electroneutrality.

To study the interaction between the protein structure and Na^+/K^+ ions, the simulation box was filled with NaCl/ KCl salts at 0.25 M concentration (Figure 2.1). To obtain and compare the time-averaged density maps of Na^+ and K^+ ions around the protein structure, derived from MD simulations, an open-source GROMACS-based toolset GROma*ρ*s [150] was applied.

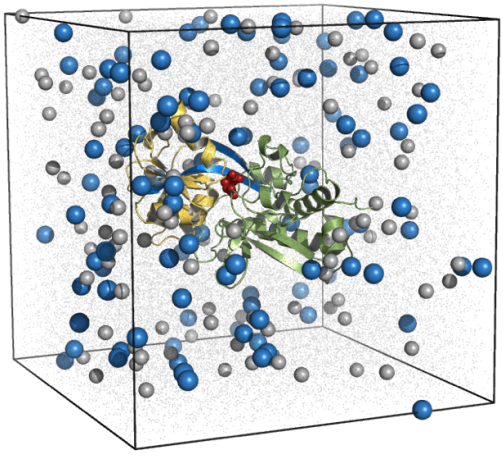

Figure 2.1. The example of a typical MD box used during simulations. The simulation box consists of one centered DEBP molecule complexed with one Glu molecule (red spheres), soaked in water (tiny grey dots) and NaCl/ KCl at 0.25 M concentration (Na^+/K^+ and Cl^- ions are blue and grey balls, respectively).

2.1.1.2 Energy minimization

The addition of hydrogens and solvent molecules will lead to big interference in the structure that might result in large forces acting on the particles. If the dynamics simulations were started at this point, the system would blow up. To cope with this problem, I performed an energy minimization (EM) using the Steepest Descent algorithm [151]. As a result, the system was relaxed to the closest local energy minimum which is reasonable enough in terms of geometry and solvent orientation for the starting MD structure. The maximum force (F_{max}) not greater than 1000 kJ × mol^{-1} × nm^{-1} after 0.01 ps step EM run indicates system stability.

2.1.1.3 System equilibration

After the energy minimization step, before starting real dynamics, the simulation system was additionally subjected to several stages of equilibration to stabilize the temperature and the pressure of the system by equilibrating the solvent and ions around the protein. In the first stage the positional restraints were applied to all atoms belonging to the *ybeJ* protein structure. This step ran for 2500 ns. In the following and final equilibration step only the backbone atoms of the protein were restrained, while the side-chains were allowed to move freely. From this additional 1000 ns we got the final positions and velocities for the MD runs. During these steps the temperature was set to 310.15 K by using the velocity-rescale thermostat [152] and the pressure was set to 1 bar with the Berendsen barostat and isotropic pressure coupling [153]. The temperature, pressure and density plots were stable over time which is a sign of a well equilibrated system.

2.1.1.4 Production phase

After the system was equilibrated at the desired temperature and pressure, free MD simulations in an isothermal-isobaric (NPT) ensemble [154] were started without any positional restrain. The NPT ensemble allows to study the system of interest under conditions of constant temperature T and pressure P that corresponds better to the experimental conditions. The velocities from the last equilibration step were retained in order to use the Parrinello-Rahman barostat [155]. In all simulations I used a leap-frog stochastic dynamics integrator with the step of 4 fs. Long range electrostatic interactions were treated with the particle mesh Ewald (PME) method [156].

To check the structural stability of the protein after 2500 ns MD simulation, the Root Mean Square Deviation (RMSD) was analyzed. MD runs were repeated several more times to get reasonable statistics.

2.1.2 Alchemical free-energy calculations

The influence of single site mutagenesis on binding affinity between the protein structure and Glu molecule was studied using alchemical free energy calculations [157]. During energy calculations an amino acid can be transformed into another one via a non-natural way, hence the name of the method. Figure 2.2 illustrates the thermodynamic cycle used in the current work. The open, ligand-free form is called apo, while the glutamate-bound closed conformation is named bound. Naturally, for the estimation of the binding free energy between the wild type (WT) and mutant (Mut), one should calculate the free energy changes for apo → bound transaction of WT and Mut separately (ΔG1 and ΔG2, respectively) and to calculate the difference of these energies (ΔΔG). In the simulations, this way would be too consumptive (time and power). Therefore, in order to circumvent this limitation, an energetically equivalent way was proposed, in which ΔΔG could be calculated from the equation:

$$\Delta\Delta G = \Delta G_2 - \Delta G_1 = \Delta G_4 - \Delta G_3 \tag{2.11}$$

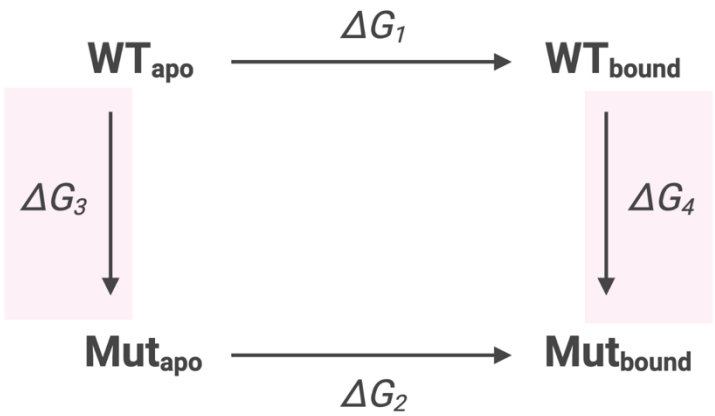

Figure 2.2. The thermodynamic cycle used in the alchemical transformation method. The energies calculated during the simulations are highlighted by red rectangles.

Before the free energy calculation was set up, the mutated protein structures and topologies were generated with the pmx package [158], which is compatible with all commonly used

force fields of the GROMACS simulation package. Following a standard procedure, the hybrid protein was placed in a simulation box with solvent and ions.

In general, the change in free energy along the reaction between WT and Mut is calculated from the work distribution (W) obtained from fast-switching simulations (Figure 2.3). But first, the simulations were performed in two independent equilibrium states A (WT) and B (Mut) following the standard unbiased molecular dynamics simulation setup to sufficiently sample the end state ensembles (λ=0 for A and λ=1 for B in eq. 2.12). We start with an energy minimization performed on both states separately. After that, the equilibration runs were used to sample the relevant phase space volumes. This step is very important, because the generated ensembles will define how accurately the free energy difference will be estimated. From the generated trajectories snapshots the system was driven (typically 10-200 ns) in the forward (A to B) and reverse (B to A) directions in a non-equilibrium manner resulting in $W_{forward}$ and $W_{reverse}$, respectively [157].

The mechanical work values for each trajectory could be obtained from [159]:

$$W = \int_0^1 \frac{\partial H}{\partial \lambda}\, d\lambda \tag{2.12}$$

where λ is coupling parameter, which switches the system during a simulation from state A (λ=0) to state B (λ=1), defined by Hamiltonians H_A and H_B, respectively.

For very long switching times the system stays close enough to equilibrium, so that one can write:

$$W = \Delta G_{AB} \tag{2.13}$$

Resulting work distributions were collected and analyzed with the Crooks Gaussian intersection method [160], which relies on Crooks' Fluctuation theorem [161] and is implemented in pmx. According to this theorem, the work distribution of forward- (P_f) and backward-switching (P_r) of the free-energy change between two states is:

$$\frac{P_f(W)}{P_r(-W)} = e^{\beta(W-\Delta G_{AB})} \tag{2.14}$$

Consequently, the free-energy change between the states A and B is the work value at which both distributions intersect:

$$\mathrm{W} = \Delta G_{AB} \leftrightarrow e^{\beta(W-\Delta G_{AB})} = 1 \leftrightarrow P_f(\mathrm{W}) = P_r(-\mathrm{W}) \tag{2.15}$$

The Crooks Gaussian Intersection point is given by [160]:

$$\Delta G_{CGI} = \frac{\frac{W_f}{\sigma_f^2} - \frac{-W_r}{\sigma_r^2} \pm \sqrt{\frac{1}{\sigma_f^2\sigma_r^2}(W_f + W_r)^2 + 2\left(\frac{1}{\sigma_f^2} - \frac{1}{\sigma_r^2}\right) ln\frac{\sigma_r}{\sigma_f}}}{\frac{1}{\sigma_f^2} - \frac{1}{\sigma_r^2}} \tag{2.16}$$

where σ_f and σ_r are the standard deviations of the respective Gaussian function.

The resulting ΔΔG values for the mutations were extracted from the analyses performed with pmx. Through the last equation the corresponding relative changes of the binding constant (K_d) values could be calculated:

$$K_d = e^{\frac{\Delta G_{bound} - \Delta G_{unbound}}{RT}} = e^{\frac{\Delta\Delta G}{RT}} \tag{2.17}$$

where T = 310.15 K is the temperature and R = 8.32 J × mol^{-1} × K^{-1} is the universal gas constant.

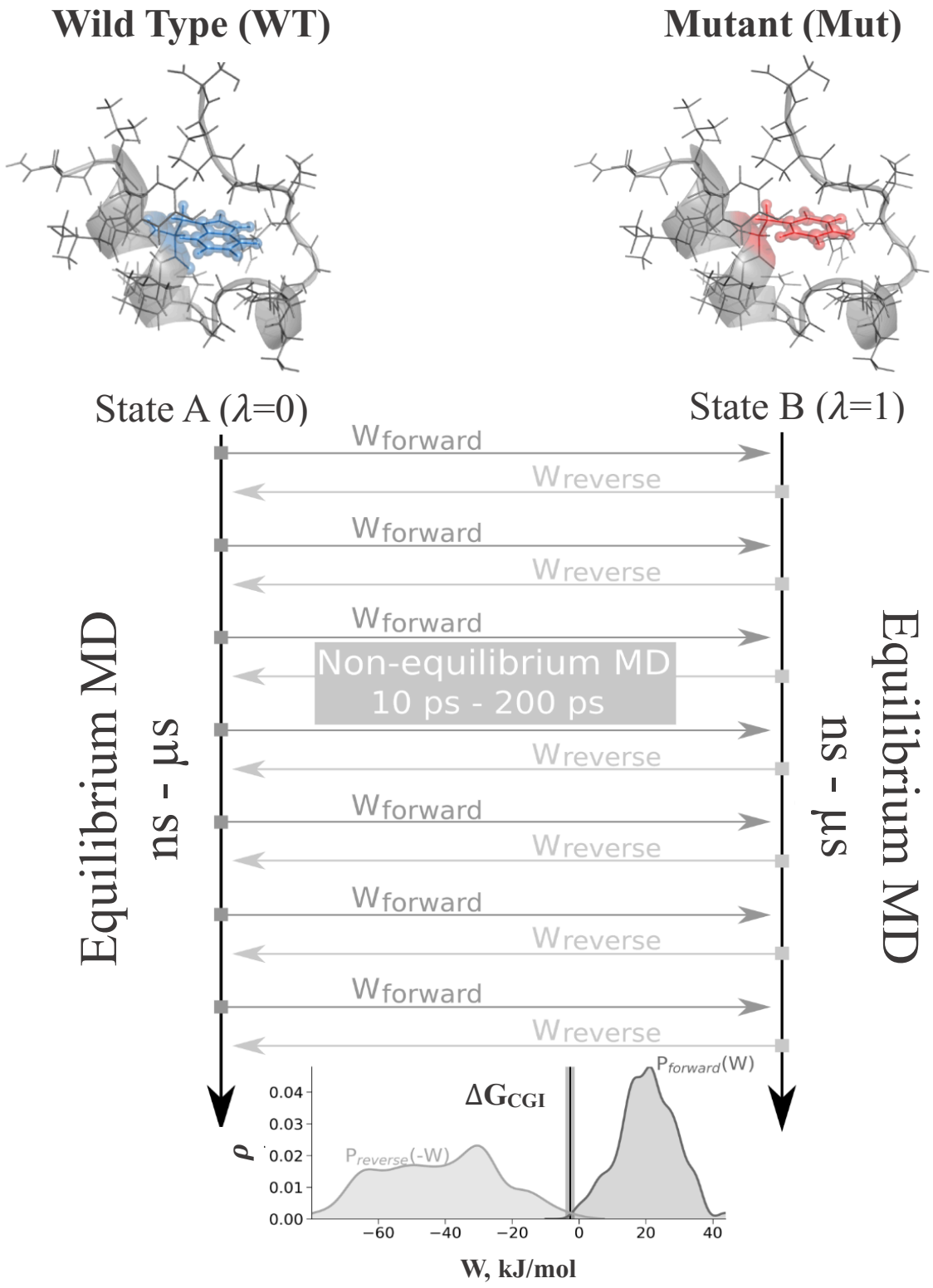

Figure 2.3. The non-equilibrium alchemical free energy calculations procedure. At the beginning, two independent equilibrium simulations were performed to sufficiently sample the end state ensembles (λ=0 for WT and λ=1 for Mut). From the generated trajectories, snapshots were selected and fast switching simulations started, driving the system in the forward (WT to Mut) and reverse (Mut to WT) directions. Required work values were collected and used for free energy difference calculations using the Crooks Fluctuation Theorem. From [157].

2.2 Experimental methods

2.2.1 Molecular biology

In order to test the theoretically predicted mutants by fluorescence experiments, site-directed PCR-based mutagenesis weas held to implement point mutations. Verified by sequencing, the constructs were expressed in *E. coli* and purified by the Immobilized Metal Affinity (IMAC) and Size-Exclusion Chromatography followed by IANBD-ester fluorophore labeling.

All buffers, chemical and materials together with the brand and manufacturers used in this work are summarized in chapter 2.2.3 and 2.3.

2.2.1.1 Site-directed mutagenesis

The original plasmid pET30b-GluBP600n was obtained from Addgene (catalog number 119835). The initial site-directed mutagenesis of pET30b-GluBP600n was performed to introduce a Thr to Cys mutation (T136C) [114] for the future labeling with a cysteine-reactive fluorophore (chapter 2.2.1.3) that will allow us to measure fluorescence changes under glutamate binding reaction (chapter 2.2.2). A new plasmid pET30bGluBP600n_T136C (hereinafter GluBP T136C) was used as a template for the generation of the plasmids encoding all GluBP protein variants studied in this work. All cloning strategies were performed by using Vector NTI software package (InforMax Inc, North Bethesda, MD, USA). Site directed mutagenesis was carried out using the PCR-based mutagenesis method using the KOD Hot DNA Polymerase Kit following the kit protocol without modifications.

Firstly, two PCR reactions (see Table 2.1 for PCR mixture composition) for each single mutation were carried out with the sense and antisense primers (Table 2.2). The standard PCR reaction usually goes through a set of temperature cycles, specified in the Table 2.3. The annealing temperature was optimized according to the used primers. The two PCR fragments were combined in the third PCR reaction using the same mixture and temperature protocols. After each PCR termination, products were analyzed by gel electrophoresis and purified using the NucleoSpin Gel and PCR Clean-up Kit according to the manufacturer's instructions.

In this work, during each electrophoresis step, 1-1.5 % - agarose gels were used for the separation during 25 min at 120 V in the TAE-running buffer. To visualize DNA bands, molten agarose was mixed with SYBR Safe DNA Gel Stain, which can be detected at 530 nm after 280 nm excitation using the BioRad Gel DocTM XR+ System (BioRad, Munich, Germany). The

size of the DNA fragments was estimated by comparison with the GeneRuler DNA ladder 1 kb molecular mass marker.

After the third PCR, the final product was subjected to a restriction protocol. The restriction enzymes digest the DNA at the corresponding restriction sites resulting in complementary ends of the target vector and the insert. The restriction reactions were done in a total volume of 30 µl (Table 2.4, preparative) and the digestion was carried out for 60 min at 37 °C.

Table 2.1. The PCR reaction components and concentrations.

Component	**Volume**	**Final concentration**
10X Buffer for KOD Hot Start DNA Polymerase	5 µl	1X
25 mM $MgSO_4$	3 µl	1.5 mM
dNTPs (2 mM each)	5 µl	0.2 mM each
PCR Grade Water	Up to 50 µl	
Sense (5') Primer (10 µM)	1.5 µl	0.3 µM
Anti-Sense (3') Primer (10 µM)	1.5 µl	0.3 µM
Template DNA (10 ng)	1 µl	
KOD Hot Start DNA Polymerase (1 U/µl)	1 µl	0.02 U/µl
Total reaction volume	**50 µl**	

Table 2.2. List of primers.

	Primer sequence
GluBP T136C [K.4224]	
Sense 1	GCGGATAACAATTCCCCTCTAGAAATAATTTTGTTTAACTTTAA-GAAGG
Antisense 1	AGAGGTAGTGCCGGAACAGACGACTACGGCTTTG
Sense 2	CAAAGCCGTAGTCGTCTGTTCCGGCACTACCTCT
Antisense 2	GCTTCCTTTCGGGCTTTGTTAGC

GluBP **A184W** T136C [K.4347]	
Sense 1	GCGGATAACAATTCCCCTCTAGAAATAATTTTGTTTAACTTTAA-GAAGG
Antisense 1	ACGTTCACCGGCCAGCAGCCAGTCATCCATCATAAAGGC
Sense 2	GCCTTTATGATGGATGACTGGCTGCTGGCCGGTGAACGT
Antisense 2	GTTATTGCTCAGCGGTGGCAG

GluBP **T191V** T136C [K.4414]	
Sense 1	GCGGATAACAATTCCCCTCTAGAAATAATTTTGTTTAACTTTAA-GAAGG
Antisense 1	GCGTTCGACGTTGTTGGTGACAGAACCACATTCAAAATCG
Sense 2	CGATTTTGAATGTGGTTCTGTCACCAACAACGTCGAACGC
Antisense 2	GTTATTGCTCAGCGGTGGCAG

GluBP **T92A** T136C [K.4415]	
Sense 1	GCGGATAACAATTCCCCTCTAGAAATAATTTTGTTTAACTTTAA-GAAGG
Antisense 1	GCGTTCGACGTTGTTGGCGGTAGAACCACATTCAA
Sense 2	TTGAATGTGGTTCTACCGCCAACAACGTCGAACGC
Antisense 2	GTTATTGCTCAGCGGTGGCAG

GluBP **T92V** T136C [K.4416]	
Sense 1	GCGGATAACAATTCCCCTCTAGAAATAATTTTGTTTAACTTTAA-GAAGG
Antisense 1	TTTTGGCGTTCGACGTTGTTGACGGTAGAACCACATTCAAAATC
Sense 2	GATTTTGAATGTGGTTCTACCGTCAACAACGTCGAACGCCAAAA
Antisense 2	GTTATTGCTCAGCGGTGGCAG

Table 2.3. PCR temperature cycling conditions.

Number of cycles	Step	Temperature	Time
	Polymerase activation	95 °C	2 min
	Denaturation	95 °C	20 s
40	Annealing	53-55	20 s
	Extension	70 °C	50 s
	Hold	8 °C	

Table 2.4. Composition of the restriction digestion mixture.

Component	Preparative Volume	Control Volume
FastDigest Enzyme I	1 µl	0.2 µl
FastDigest Enzyme II	1 µl	0.2 µl
FastDigest Green Buffer (10X)	3 µl	1 µl
Plasmid DNA	1 µg	1 µl
H_2O biodest	up to 30 µl	up to 10 µl
Total volume	**30 µl**	**10 µl**

All restriction digestion mixtures were separated by gel electrophoresis. The required DNA fragments were isolated by cutting the respective DNA-bands out from the gel using a scalpel under UV light in a BioRad Gel DocTM XR+ System (BioRad, Munich, Germany). The DNA extraction from the gel pieces was performed by using the NucleoSpin Gel and PCR Clean-up according to the manufacturer's protocol.

Finally, the T4 DNA ligase adds together the target vector and an insert, forming a single DNA molecule. The protocol of ligation was carried out using the Rapid Ligation Kit for ligation mixture (Table 2.5) according to user's manual. The ligation mixture was incubated at 22 °C for 10 min. For correct determination of the insert DNA amount needed for the reaction, the ligation calculator was used [162].

Table 2.5. Composition of the DNA ligation mixture.

Component	Volume/ Amount
Linearized vector DNA	50 ng
Insert DNA (at 3:1 molar excess over vector)	variable
5X Rapid Ligation Buffer	4 µl
T4 DNA Ligase, 5 U/µl	1 µl
Nuclease-free water	up to 20µl
Total volume	**20 ml**

After the ligation reaction, 5 µl of reaction mixture was transformed into 50 µl of Top10F competent cells using the heat shock method: after 20 minutes of incubation on ice, the reactions were heat shocked for 1 minute at 42 °C and immediately afterwards incubated on ice for another 20 minutes. A 200 µl aliquot of LB medium was added to the reaction mixture and incubated while shaking at 37 °C for 45 minutes allowing the cells to recover. Finally, the reaction was spread on a pre-warmed LB plate containing Kanamycin (Kan, 30 µg/ml) and incubated overnight at 37 °C.

Next day, from each incubated plate, five colonies were randomly selected and grown overnight in 5 ml LB+Kan (0.3 mg/ml) medium at 37 °C. The plasmids were isolated using NucleoSpin Plasmid kit. Newly synthesised DNAs were verified by a control restriction, carried out for ~ 30 min at 37 °C (Table 2.4, control), and the DNA sequence analysis, performed by Eurofins Genomics (Edersberg, Germany). Protein sequence was analyzed by using Vector NTI in combination with the GENtle (Magnus Manske, Cologne University, Germany) software package.

2.2.1.2 Protein Expression and Purification

Expression of the GluBP variants were performed in *E.coli* BL21 (DE3) bacteria cells. After re-transformation on a LB + Kanamycin agar plate, single colonies were picked and infused in 5 ml precultures (LB medium with 0.3 mg/ml Kan) and grown over day at 37 °C. The following 50 ml preculture was grown overnight under the same conditions. The next day a 450 ml culture was grown at 37 °C and 120 rpm until the OD_{600} reached a value of 0.6-0.9. At that moment some 25 % glycerol stocks were prepared and stored at -80 °C while the expression was induced

overnight at 20 °C and 120 rpm in the presence of 1 mM isopropyl-D-thiogalactopyranoside (IPTG). Next day, bacteria were harvested by centrifugation at 4 °C and 6.000 × g for 20 minutes in the Avanti JXN-26 centrifuge (Beckman Coulter, California, USA), freezed fast in liquid Nitrogen and stored at -80°C.

The pellets were resuspended in Binding Buffer (chapter 2.2.3, Table 2.12) containing one tablet of EDTA-free Complete protease inhibitor cocktail and lysed on ice by sonication (Sonifier® W-450 D, G. Heinemann, Germany) using a 40 % amplitude and 3 min program with the following two cycles of 70 % amplitude and 1 min.

After sonication and another round of centrifugation (4 °C, 15.000 × g, 20 min), the clarified lysate was filtered with a 0.22 µm pore filter and loaded on a HisTrap™ HP Ni^{2+}-NTA column for affinity chromatography at 8 °C. The protein was eluted with a linear gradient until 0.5 M imidazole in Elution buffer (chapter 2.2.3, Table 2.13) using a 1 ml/min flow rate. The fractions of interest were collected and applied on the Superdex 200 16/60 column previously equilibrated in HEPES 7.5 buffer (chapter 2.2.3, Table 2.18) for a size exclusion chromatography. Aliquoted fractions were concentrated using Amicon centrifugal filters and stored at -80 °C. Later, the purified protein was subjected again to an analytical Superdex 200 10/30 column to check the protein stability after a freezing-thawing cycle. The expression and purification protocols are based on [109], [114].

The protein purity was assessed by denaturing SDS-PAGE (Table 2.6) using Laemmli Sample Buffer in Vertical Electrophoresis Cell (BioRad) with SDS-running buffer (chapter 2.2.3, Table 2.15) at 120V during 50 min. Staining was held during 1h in Coomassie Staining buffer (chapter 2.2.3, Table 2.16) with the following destaining overnight at the Coomassie Destaining buffer (chapter 2.2.3, Table 2.17). Protein bands were identified by comparing with the molecular weight standard PageRuler™ Plus.

Table 2.6. SDS-page composition.

12% Separating Gel			4% Stacking Gel		
	Component	**Volume**		**Component**	**Volume**
	H_2O	3.3 ml		H_2O	6.1 ml
	1.5 M Tris-HCl pH 8.8	2.5 ml		1.5 M Tris-HCl pH 6.8	2.5 ml
	10% SDS	100 µl		10% SDS	100 µl
	Protogel	4.0 ml		Protogel	1.3 ml
	10% APS	100 µl		10% APS	50 µl
	TEMED	10 µl		TEMED	10 µl
	Total volume	**10 ml**		**Total volume**	**10 ml**

2.2.1.3 Protein Labeling

The labeling procedure was based on the Thiol-Reactive Probe Labeling Protocol (Thermo Fischer Scientific) [163]. The purified variants of GluBP were labeled during 2 hours at room temperature using a 2-fold excess of thiol-reactive environmentally sensitive IANBD-ester fluorophore (see chapter 1.9).

The protein was dissolved in HEPES 7.5 buffer (chapter 2.2.3, Table 2.18) at room temperature to get a final 200 µM concentration. To reduce disulfide bonds, a 10-fold molar excess of dithiothretiol (DTT) was used during 25 min at room temperature (RT). Prior to the introduction of the dye, the DTT reducing agent was washed out by 2X wash on a gel filtration column Sephadex G-25 in HEPES 7.5 buffer. A 10 mM stock solution of the IANBD-ester dye was prepared in dimethylsulfoxide (DMSO) and protected from light by wrapping the container in aluminium foil. Sufficient amount of reagent from the stock solution was added to the protein solution to give 2 moles of reagent for each mole of protein. Prepared solutions were stirring, and the reaction was allowed to proceed for 2 hours at RT. Then the conjugate was separated on a gel filtration column Sephadex G-25 in working buffer. Afterwards, to check the labeling results, the protein samples were run in a 12 % SDS gel for 50 min at 190 V and scanned in a Typhoon™ FLA 9500 (GE Healthcare, Life Sciences, Illinois, USA) to detect the fluorescence signal given by the labeled proteins.

2.2.1.4 Protein concentration measurements

The protein concentration was determined spectroscopically with molar extinction coefficient ε at 280 nm using a NanoDrop 2000 Spectrophotometer (Thermo Scientific, Massachusets, USA). ε_{280} for GluBP was calculated from the amino acid composition in VectorNTI and it was 23 830 M^{-1} cm^{-1}. Molecular weight of protein Mw was ~ 34.8 kDa.

The concentration of fluorescently labeled by IANBD ester fluorophore proteins (Fl-GluBP and mutations) were estimated using ultraviolet spectroscopy with an extinction coefficient of 25 000 M^{-1} cm^{-1} at 495 nm (absorbance peak of IANBD ester) [114].

2.2.2 Fluorescence measurements

Luminescence is the emission of light from any substances, which occurs from electronically excited states and divided into two categories: fluorescence and phosphorescence.

Fluorescence is associated with the absorption and re-emission of light in the pico- to nanosecond time range [164]. The processes which occur between the absorption and emission of light are usually illustrated by a Jablonski diagram (Figure 2.4). The process is related to the absorption of energy in the form of light ($h\nu$) on a femtoseconds timescale, which causes a change in the electron distribution, whereby an electron is transferred from the ground (S_0) to an excited state (S_1; usually the lowest excited state).

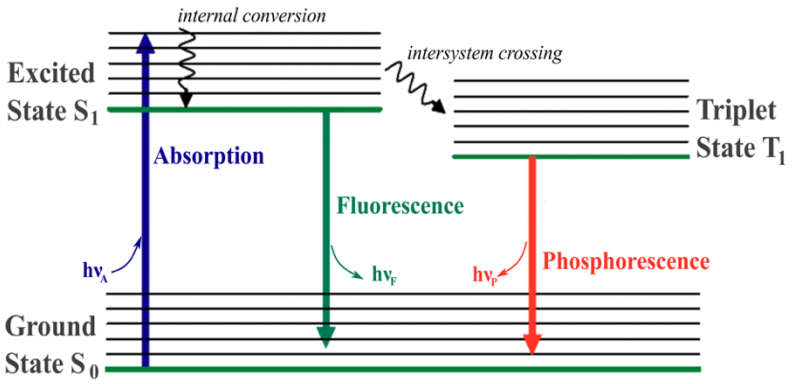

Figure 2.4. The simplified energy level diagram (Jablonski diagram). Picture was modified from [164, 165].

Fluorescence measurements can be classified into two types: steady-state and time-resolved. Steady-state measurements are performed with constant illumination using a continuous beam of light and emission spectra observation. In time-resolved measurements, the sample is exposed to a pulse of light (in most cases shorter, sometimes in the range to the excited state lifetime) and the intensity decay is recorded with a high-speed detection system [164].

2.2.2.1 Steady-state fluorescence spectroscopy

Steady-state fluorescence experiments were performed using a FS-5 Fluorolog spectrofluorimeter (Edinburgh Instruments, UK) coupled to a TC1 temperature controller (Quantum Northwest, USA) by using Fluoracle® Spectrometry software (Edinburgh Instruments, UK) in a stirred 3.5 ml cuvette (Figure 2.5).

During the emission spectra measurements, the sample solution containing 0.1-0.3 μM of protein (WT or variants) in assay buffer pH 7.5 was stabilized to 20 °C and excited with 495 nm wavelength. The emission spectra were recorded and represented as an average of 2-3 independent replicates in a 505-650 nm wavelength range. The peak value of measured spectra (~ 544 nm) was chosen as an emission wavelength for a kinetic scan of equilibrium binding titrations.

For glutamate affinity studies, the WT and variants at a 0.1-0.3 μM concentration in HEPES 7.5 buffer, were manually titrated with an appropriate stock solution of L-glutamate at 20 °C until saturation was reached. Measurement of each step was held for 15 seconds (s), recorded with a step of 0.5 s and averaged. Fluorescence intensity records of the full glutamate concentration range were corrected for dilutions, normalized and plotted against the glutamate concentration (in log scale). The titration curve was fitted to the Hill equation and the apparent glutamate dissociation constant (K_d) together with the cooperativity (n) were obtained. When n molecules of ligand (L) bind to a receptor (R), the ratio of bound to total receptors at equilibrium is given by [166]:

$$\frac{Bound}{Total} = \frac{[RL_n]}{[R] + [RL_n]} = \frac{\frac{[L]^n}{K_d}}{1 + \frac{[L]^n}{K_d}} \tag{2.18}$$

The same type of experiments under the analogous conditions were carried out to assess the ligand binding selectivity for the WT and two low-affinity mutants by titrating samples with L-aspartate. In order to check the influence of physiological temperature on the protein affinity to glutamate, the samples were titrated also at 37 °C.

To study the pH stability of proteins, a series of buffers with a pH 5.5 – 8.0 range (in ~ 0.5 pH unit intervals; chapter 2.2.3, Table 2.18) was prepared. The glutamate titrations were performed in each buffer at 20 °C using 0.1- 0.3 μM protein. Additional buffers with different

concentrations of NaCl and KCl were also prepared (chapter 2.2.3, Table 2.19) and used to study salt dependency of the glutamate binding process.

All titrations were performed at least in triplicates and expressed as mean ± SEM (Standard Error of the Mean).

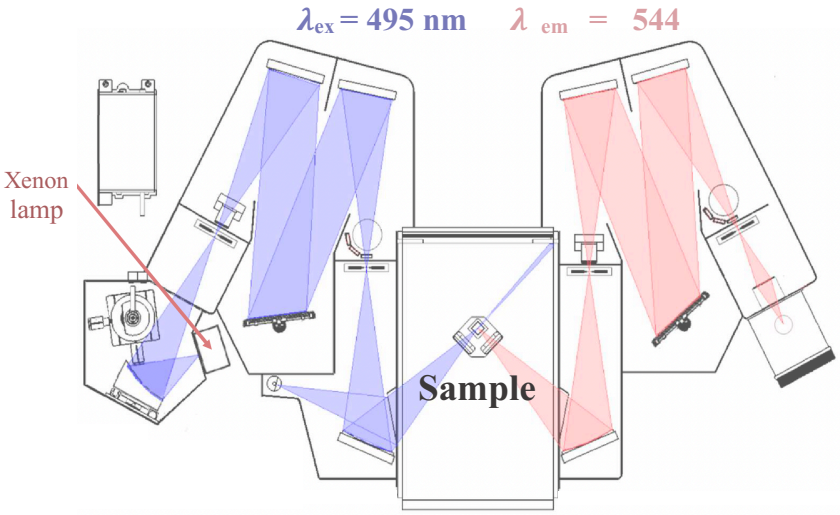

Figure 2.5. The principal optical design of the working set-up (Spectrofluorometer FS-5). Picture was modified from [167].

2.2.2.2 Stopped-flow fluorimetry

A stopped-flow instrument is the most frequently used rapid technique which allows to follow rapid chemical reactions on the milliseconds to second timescale. In the stopped-flow experiments, 2 sample solutions (Single Mixing mode) held in separate reservoirs, are injected, and rapidly driven into a mixer, initiating an extremely fast mixing reaction. The newly mixed solution travels into the observation cell making the instrument reach a stationary state. At this point a flow phase is stopped to record kinetics by a detector. The time between the mixing point and the first observation is defined as the dead time and can be changed by variation of the flow rate.

Glutamate association kinetic experiments for the low-affinity mutants were performed in a SFM400 or a µSFM (BioLogic Science Instruments, France) stopped-flow system using the Bio-Kine software (BioLogic). 3-12 µM protein (concentration in the mixing chamber) was rapidly mixed with glutamate at a series of concentrations (in concentration increasing way) in the assay buffer HEPES 7.5 (Table 2.18). The fluorescence excitation was set to ~ 490 nm with a 485DF22 filter, while the fluorescence emission was filtered at 545 nm through the 545RDF35 filter. The theoretical dead time was 1.5 ms [168].

Because the WT protein demonstrated a very fast kinetic, the measurements for it were carried out on a Hi-Tech Scientific SHU-61SX2 stopped-flow system (TgK Scientific, UK) with Kinetic Studio software (TgK Scientific). For these measurements ~ 25 μM concentration of protein was used. The excitation was performed at 492 nm, and emission was collected using the long pass OG530 filter (≥ 530 nm). The dead time in this system is ~ 0.5 ms.

Both systems were equipped with the Circular Water Bath (Haake, Karlsrue, Germany) which allowed to keep the temperature during the experiment constant, at 5 °C. Figure 2.6 demonstrates the main principle of work and difference between these two stopped-flow machines.

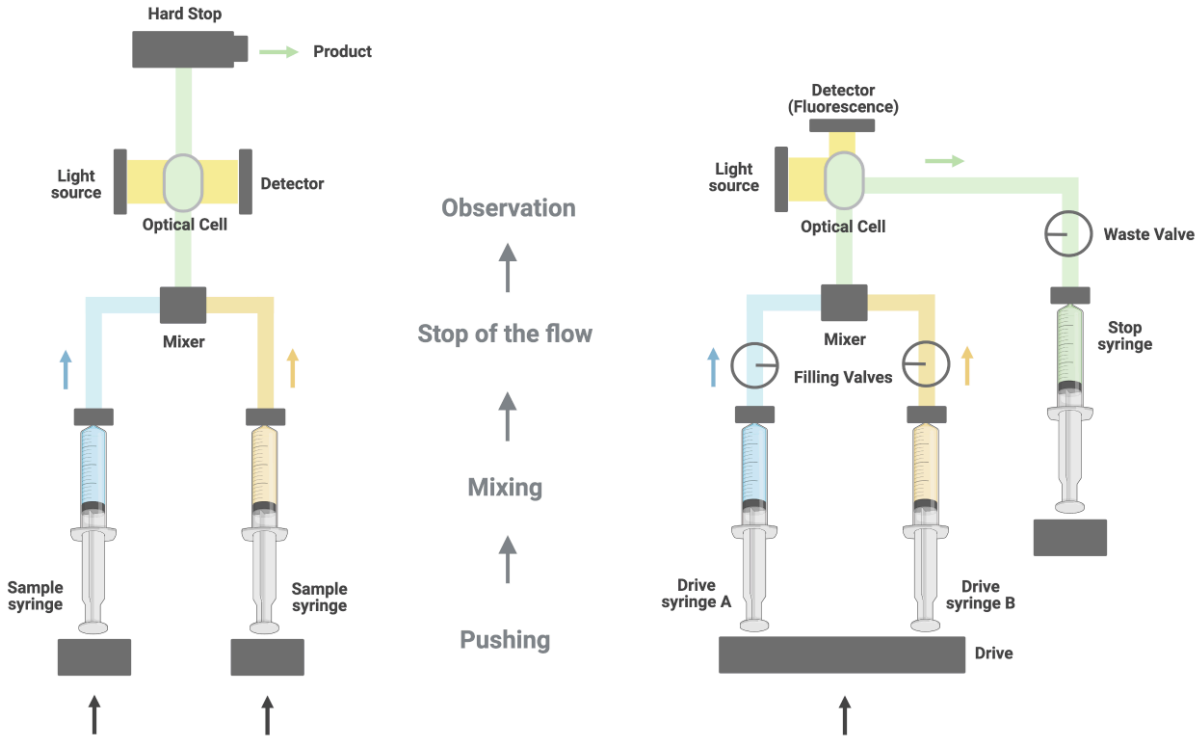

Figure 2.6 Schematic representation of stopped-flow machines. Both have the same principle of operation: two syringes are pushed simultaneously, causing their content to travel into the mixer and then to the measuring cell (optical cell), where the sample gets excited, and the fluorescence is collected by the detector. The only principal difference is in the flow stoppage mechanism. μSFM (left) is driven by step motors, which are synchronized with a stop valve called the hard-stop. In the SHU-61SX2 stopped-flow system (right), injected volume is limited by the stop syringe. Schemes are prepared by BioRender.com.

Data were collected, represented as the average of at least 3-5 traces from 3 independent repetitions and fitted using a single exponential to ascertain the fluorescence rise rate. Complex

ligand binding mechanisms have biphasic kinetics and are divided in two categories: conformational selection and induced-fit [169, 170]. The induced fit model (Figure 2.7, right) assumes that a conformational change, which increases the protein affinity to the ligand, follows the ligand binding action. Under the rapid equilibrium approximation, when the conformational changes are much slower than binding and dissociation, the dependence of rate constant k_{obs} on [L] defines the involved mechanism. In the case of induced fit mechanism, k_{obs} increase hyperbolically with [L] according to the following equation:

$$k_{obs} = k_2 + k_1 \frac{[L]}{K_d + [L]} \tag{2.19}$$

where k_1 and k_2 are forward and backward rate constants of the conformational change, respectively. K_d is the equilibrium dissociation constant that is defined as the ratio of the second-order rate constant for ligand binding to the first-order rate of dissociation (k_{off}/k_{on}). [L] is ligand concentration.

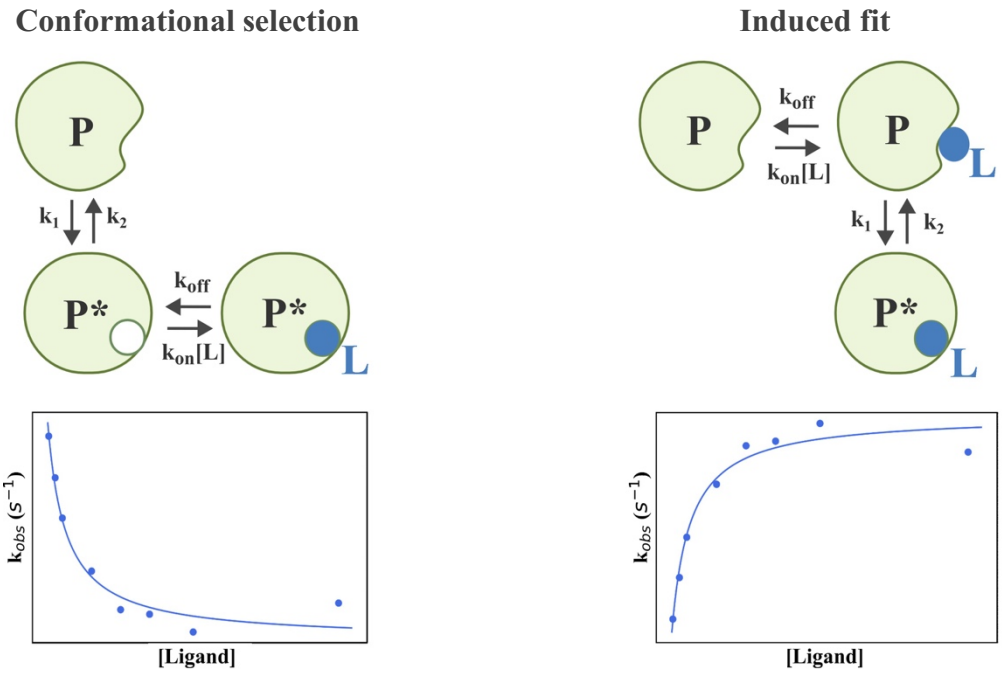

Figure 2.7. The illustration of two-step protein-ligand interaction models. An example of data is plotted and fitted with a hyperbolic function describing the respective model: conformational selection (left) or induced-fit (right). Conformational selection postulates a pre-existing equilibrium between the P and P^* forms, on which only P binds the ligand. The induced-fit model postulates a conformational transition between PL and P^*L that optimizes binding. Figure is prepared according to [169].

In the conformational selection mechanism (Figure 2.7, left), the protein exists in equilibrium between two forms, with the ligand binding to a pre-existing conformation and stabilizing it. Here the rate constant decreases hyperbolically with [L] and is calculated by using the next equation:

$$k_{obs} = k_1 + k_2 \frac{K_d}{K_d + [L]} \tag{2.20}$$

2.2.2.3 Fluorescence lifetime measurements

The fluorescence lifetime of the IANBD-ester fluorophore bound to the different GluBP proteins was measured by the Time-Correlated Single-Photon Counting (TCSPC, PicoHarp 300, PicoQuant, Berlin, Germany) technique. This method is useful in elucidating how changes in the local environment or molecular interactions influence on a molecule's fluorescence properties [171].

During measurements, the fluorophore of the sample is excited with laser (LDH-C 440, PicoQuant) pulses of photons (length is 50 ps) with defined wavelength (440nm) at a high repetition frequency (20 MHz). The photon detector, working in single photon counting mode, registers each photon with very accurate timing at 544 nm (chosen by monochromator). The time interval between the excitation pulse and the registration of the first detected photon is measured, collected and plotted in the histogram of number of events (counts) versus time (Figure 2.8). This histogram can be analyzed by iterative reconvolution of the instrument response function, IRF(t), with a sum of exponential model functions, using the FluoFit software (PicoQuant). The example of measurements and their fits are represented in Figure 2.9. Three-exponential fitting leads to a better description of the fluorescence decay than mono- and bi-exponential. However, because of the recognized temporal variation of the IRF, which could be connected to the slight cuvette position shift during the experiments, it was necessary to introduce ultrafast component (~ 0.02 - 0.03 ns) into the three-exponential fit for some samples. Nonetheless, for the results consistency, this ultrafast component was used in analysis for all measurements. From the next equation the average fluorescence lifetime (τ_{ave}) was calculated [172]:

$$\tau_{ave} = \frac{\sum_i A_i \tau_i}{\sum_i A_i} \tag{2.21}$$

where A_i is the respective amplitude and τ_i is the lifetime of the exponential component, $i = 3$.

For the ligand concentration-dependent changes in the fluorescence lifetime determination, titrations of aspartate and glutamate were carried out. The ligand was manually added to the 3.5-ml cuvette containing 0.1-0.2 µM of protein (WT or variants) in the assay buffer HEPES 7.5 (Table 2.19). The same experiments were done for pH 5.8 (MES 5.8 buffer, Table 2.18). A minimum of 3 repetitions from 3 replicates were carried out and averaged for the analysis.

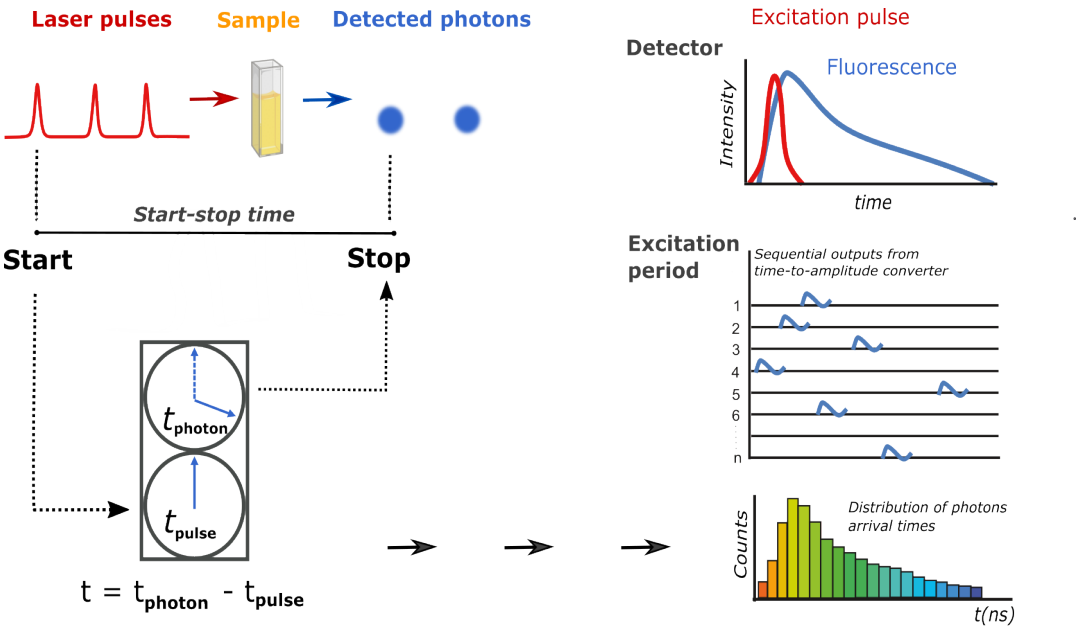

Figure 2.8. The Time-Correlated Single Photon Counting mechanism. The detection of the fluorescence lifetime starts (START t_{pulse}) when a pulsed laser excites the sample with a fluorophore. It stops (STOP t_{photon}) by the detection of the emitted photon. All detected photons are collected in a histogram to calculate τ_{ave}. The scheme was prepared according to [172, 173].

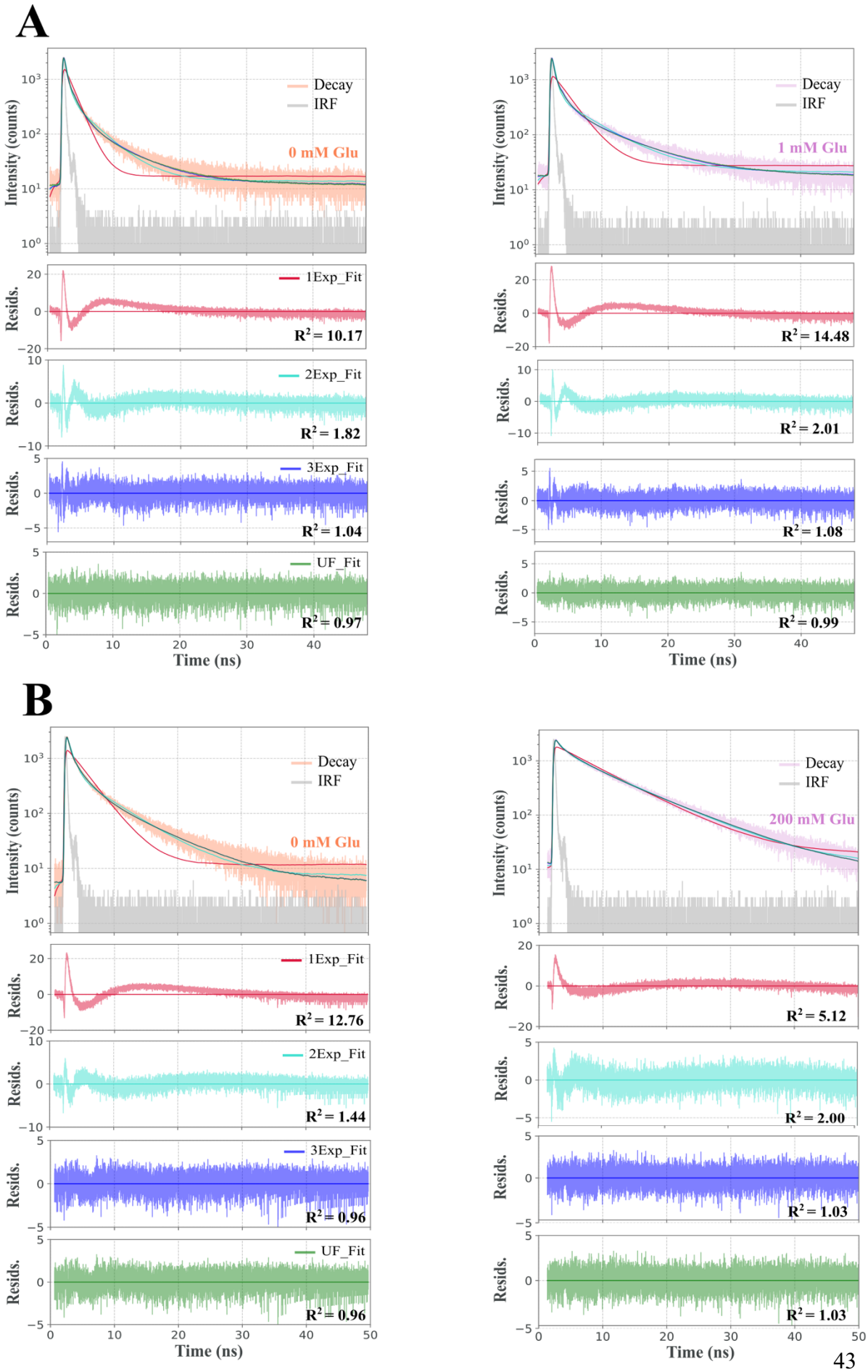
A
Intensity (counts)
Decay
IRF
0 mM Glu
1 mM Glu
Resids.
1Exp_Fit
R^2 = 10.17
R^2 = 14.48
2Exp_Fit
R^2 = 1.82
R^2 = 2.01
3Exp_Fit
R^2 = 1.04
R^2 = 1.08
UF_Fit
R^2 = 0.97
R^2 = 0.99
Time (ns)
B
0 mM Glu
200 mM Glu
R^2 = 12.76
R^2 = 5.12
R^2 = 1.44
R^2 = 2.00
R^2 = 0.96
R^2 = 1.03
R^2 = 0.96
R^2 = 1.03

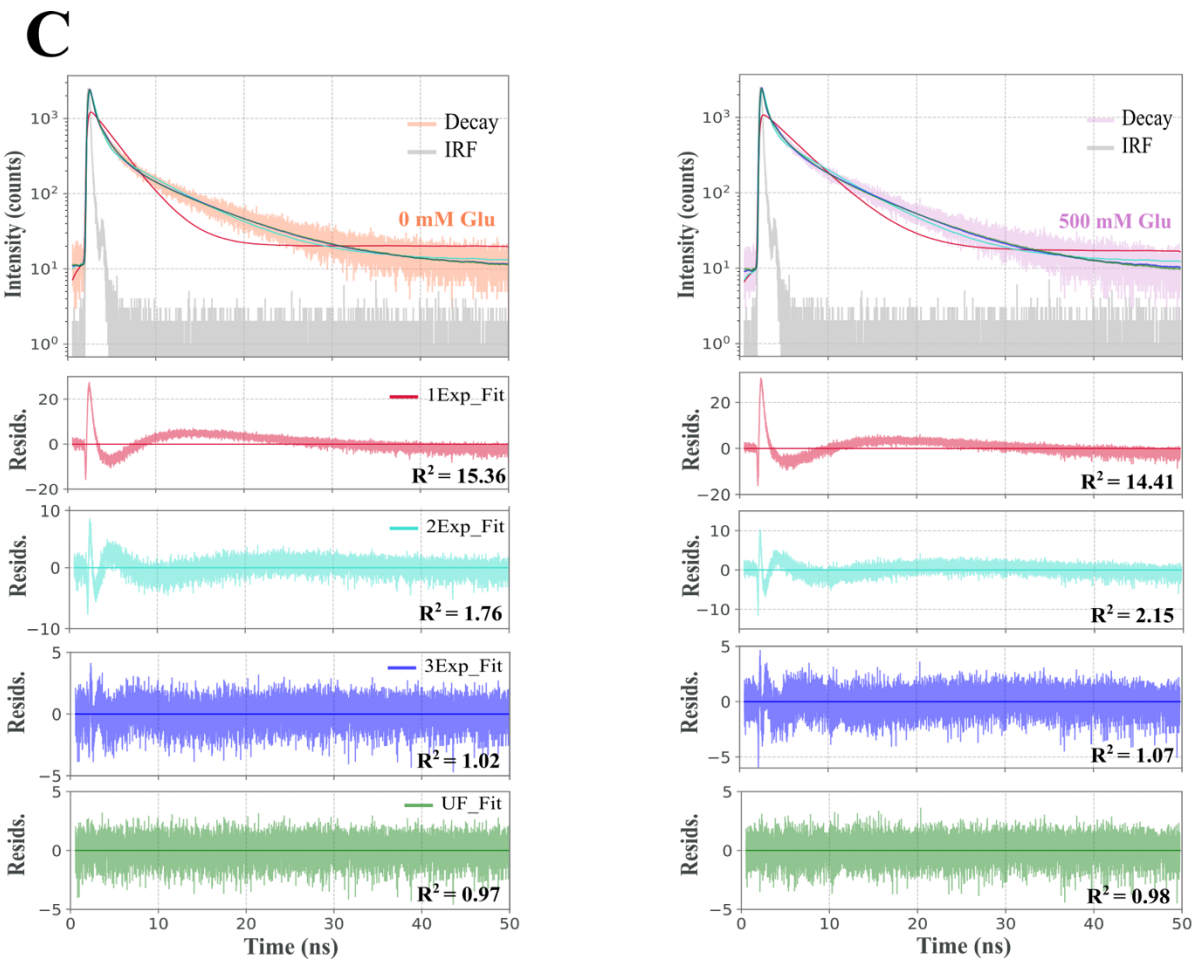

Figure 2.9. Comparison of fits of the Fl-GluBP-WT, Fl-GluBP-T91V and Fl-GluBP-T92V fluorescence decay measurement at pH 5.8. The fluorescence decays of (A) Fl-GluBP-WT at 0 mM (left) and 1 mM (right), (B) Fl-GluBP-T91V at 0 mM (left) and 200 mM (right) and (C) Fl-GluBP-T92V were fitted with mono-, bi-, three- and UF-three-exponential (with the ultrafast component) functions. The fitting curves are represented by solid line overlaying the measured data.

2.2.3 Chemicals, materials and buffers

Aqueous solutions and buffers were prepared with bi-distilled water and filtered with either 0.22 or 0.45 µm pore size filters (Millipore, Merck), according to the purity grade required for experiments. All chemicals were obtained from different companies listed in the tables below.

Table 2.7. List of the reagents and kits used in PCR-based site-directed mutagenesis method.

Reagents and Kits	**Catalog N°**
pET30b-GluBP600n plasmid, Addgene	119835
KOD Hot Start DNA Polymerase Kit, Sigma Aldrich	71086
Primers, Eurofins Genomics	
NucleoSpin Gel and PCR Clean-up, Macherey-Nagel	740609
Rapid DNA Ligation Kit, Thermo Scientific™	K1422
FastDigest BglII, Thermo Scientific™	ER0081
FastDigest EcoRI, Thermo Scientific™	FD0275
FastDigest NdeI, Thermo Scientific™	FD0584
FastDigest Green Buffer (10X), Thermo Scientific™	B72
NucleoSpin Plasmid (DNA Purifikation Kit), Macherey-Nagel	740588
Agarose NEEO ultra-quality, Carl Roth	2267
SYBR™ Safe DNA Gel Stain, Invitrogen, ThermoFischer	S33102
GeneRuler 1 kb DNA Ladder, Thermo Scientific	SM0313
LB-Medium/-Agar (Miller), PanReac AppliChem	A0954/A0927
Kanamycin, Sigma, Merck	K1377
TOP10F competent *E.coli* cells, Invitrogen	C303006

Table 2.8. Reagents and materials used in protein expression and purification.

Reagents and Materials	**Catalog N°**
BL21 (DE3) competent *E.coli* cells, BioLabs	C25271
IPTG BioChemica, PanReac AppliChem	A1008
Glycerol, PanReac AppliChem	A2926
cOmplete™ EDTA-free Protease Inhibitor Cocktail, Roche, Merck	05056489001
Syringe filter 0.22µm, Fisher Scientific	15181499
DURAPORE®0.22µm Membrane filters, Merck	GVWP04700
HisTrap™ HP column, Cytiva	17524701
Superdex™ 200 pg HiLoad™ 16/60 column, Cytiva	28989335
Superdex™ 200 Increase 10/300 GL column, Cytiva	28990944
Amicon® Ultra-15 Centrifugal Filters (10K), Merck Millipore Ltd.	UFC9010
Nickel Sulfate Hexahydrate ($NiSO_4$), Sigma Aldrich, Merck	N4882
Sodium di-Hydrogen Phosphate 1-hydrate (NaH_2PO_4), PanReac AppliChem	131965
EDTA, Carl Roth	1PHC

Table 2.9. Reagents and materials used in labeling.

Reagents and Materials	**Catalog N°**
IANBD Ester, Setareh Biotech	7635
DTT, PanReac AppliChem	A1101
PD Mini/midi Trap G-25, Sephadex™, Cytiva	28918 007/008
DMSO (Dimethylsulfoxide) anhydrous, Invitrogen	D12345

Table 2.10. List of compounds for SDS-PAGE.

Compounds	**Catalog N°**
Acetic-acid 96%, Merck	1.00062
Ammonium persulfate (APS), PanReac AppliChem	A1142
Bromphenol blue, Sigma Chemical	B-6896
Coomassie Brilliant Blue, SERVA	17525
Ethanol 99.8% Denatured, PanReac AppliChem	147194
Glycine for analysis, PanReac AppliChem	131340
Hydrochloric acid 32% for analysis (HCl), Merck	1.00319
PageRuler^{TM} Plus, Prestained Protein Ladder, Thermo Scientific	26619
Acrylamide/Bis Solution, 37.5:1, SERVA	10688
SDS, SERVA	20765
TEMED, Sigma Aldrich, Merck	T9281
Tris for molecular biology, PanReac AppliChem	A2264

Table 2.11. Fluorescence measurements chemicals and materials.

Chemicals and materials	**Catalog N°**
HEPES, SERVA	25245
Sodium Chloride for analysis (NaCl), PanReac AppliChem	131659
Potassium Chloride for analysis (KCl), PanReac AppliChem	131494
Magnesium Chloride 6-hydrate ($MgCl_2$), PanReac AppliChem	131396
Imidazole hydrochloride, Sigma Aldrich, Merck	I3386
MES, SERVA	29830
L-Glutamic acid monosodium salt hydrate, Sigma Aldrich, Merck	G1626
L-Aspartic acid sodium salt monohydrate, Sigma Aldrich, Merck	A6683

Table 2.12. Binding buffer. pH was adjusted to 7.4 with NaOH.

Substance	Concentration
NaH_2PO_4	50 mM
NaCl	300 mM
Imidazole	30 mM

Table 2.13. Elution buffer. pH was adjusted to 7.4 with NaOH.

Substance	Concentration
NaH_2PO_4	50 mM
NaCl	300 mM
Imidazole	500 mM

Table 2.14. 5X Laemmli Sample Buffer.

Substance	Concentration
Tris pH 6.8	300 mM
SDS	10%
Glycerol	50%
DTT	50 mM
Bromophenol blue	0.05%

Table 2.15. 10X SDS-Running Buffer, pH 8.3.

Substance	Concentration
Tris	250 mM
Glycine	1920 mM
SDS	1%

Table 2.16. Coomassie Staining Solution.

Substance	Volume/ Amount
Coomassie Brilliant Blue	1.5 g
Ethanol Denatured	450 ml
Acetic Acid	92 ml
H_2O	up to 1000 ml

Table 2.17. Coomassie Destaining Solution.

Substance	Volume/ Amount
Ethanol Denatured	300 ml
Acetic Acid	30 ml
H_2O	up to 1000 ml

Table 2.18. Buffers for pH sensitivity measurements. Depending on their respective pH buffering range, MES based buffers were prepared for a pH 5.5-6.5 range and called MES 5.5, MES 5.8 and MES 6.5, and HEPES for pH 7-8 (HEPES 7.0, HEPES 7.5 and HEPES 8.0). The pH was adjusted using NaOH at 20 °C.

Substance	Concentration
MES/HEPES	50 mM
NaCl	100 mM
$MgCl_2$	2 mM

Table 2.19. Buffers for salt dependency measurements: 100KCl, 100NaCl, 200NaCl and 100NaCl + 100KCl buffers, pH was adjusted to 5.8 with NaOH at 20 °C.

Substance	Concentration
MES	50 mM
KCl/ NaCl/ NaCl/ KCl+NaCl	100/ 100/ 200/ 100+100 mM
$MgCl_2$	2 mM

Table 2.20. 50X TAE-Running buffer.

Substance	Concentration
TrisBase	2 M
EDTA	0.5 M
Acetic acid	1 M

2.3 Manufacturers

Table 2.21. List of manufacturers.

Addgene	Watertown, MA, USA
Beckman Coulter	Brea, CA, USA
BioLabs	Ipswich, MA, USA
BioLogic Science Instruments	Seyssinet-Pariset, France
BioRad	Munich, Germany
Carl Roth	Karlsruhe, Germany
Cytiva	Marlboroug, MA, USA
Edinburgh Instruments	Livingston, UK
Eurofins Genomics	Edersberg, Germany
Fisher Scientific	Hampton, NH, USA
GE Healthcare	Chicago, IL, USA
GROMACS	University of Groningen, Netherlands
Hellma	Müllheim, Germany
InforMax Inc	North Bethesda, MD, USA
Invitrogen	Carlsbad, CA, USA
Linux	Linus Torvalds
Macherey-Nagel	Düren, Germany
Merck	Darmstadt, Germany
Microsoft Corporation	Redmond, WA, USA
PanReac AppliChem	Darmstadt, Germany
PicoQuant	Berlin, Germany
SERVA	Heidelberg, Germany
Setareh Biotech	Eugene, OR, USA
Sigma-Aldrich	Göttingen, Germany
TgK Scientific	Bradford-on-Avon, UK
Thermo Scientific	Massachusets, USA
ThermoFischer Scientific	Waltham, MA, USA

2.4 Data analysis

The visual inspection of the MD simulations was done with visualization programs such as VMD [174] and PyMOL [175]. All atomistic simulation data were analyzed with a combination of GROMACS tools [145] and self-prepared python scripts using the NumPy [176] and SciPy [177] libraries. Alchemical free energy calculations were analyzed and visualized by the pmx package [158]. The time-averaged density maps of K^+ and Na^+ ions were computed by GROmaps [150] toolset.

Protein sequence analyses were carried out by Vector NTI (InforMax Inc, North Bethesda) and GENtle (Magnus Manske, Cologne University) software packages.

Experimental data from fluorescence measurements were analyzed mostly by self-prepared python scripts. All titrations in the steady-state experiments were performed at least in triplicates, corrected for dilutions, normalized, plotted against the glutamate concentration (in log scale) and fitted to the Hill model [166]. Stopped-flow traces were collected, represented as the average of at least 3-5 traces from 3 independent experiments and fitted using a single exponential function. Received rate constants were plotted against glutamate concentration and fitted by one of the biphasic interaction models [169, 170]. Data from lifetime measurements were analyzed in PicoHarp software (PicoQuant) and received time decays were plotted against glutamate concentration for a fitting by Hill equation.

All plots were prepared in python with the aid of the Seaborn [178] and Matplotlib [179] libraries. The statistical evaluation of the goodness of the fits were based on the coefficient of determination (R^2), which value was always close to 1. The final calculated values from the experiments are expressed as mean ± standard error of the mean (SEM).

Chapter 3. Results

3.1 Computational studies of GluBP

3.1.1 Glutamate binding pocket rearrangement is crucial for glutamate affinity

In absence of glutamate, the *ybeJ* is in an open ligand-free (apo) state, while after glutamate binding the protein adopts a closed (bound) conformation [122]. This transition from the apo to the bound state is characterized by a series of rearrangements of the residues forming the glutamate binding pocket. Therefore, it is assumed that they are responsible for glutamate binding and that their mutations could lead to a change of the protein affinity to glutamate.

In order to choose mutation sites for affinity variants, we analyzed residues around the glutamate binding site and among those, residues with the shortest distance (~ 2 Å) from the glutamate molecule were selected.

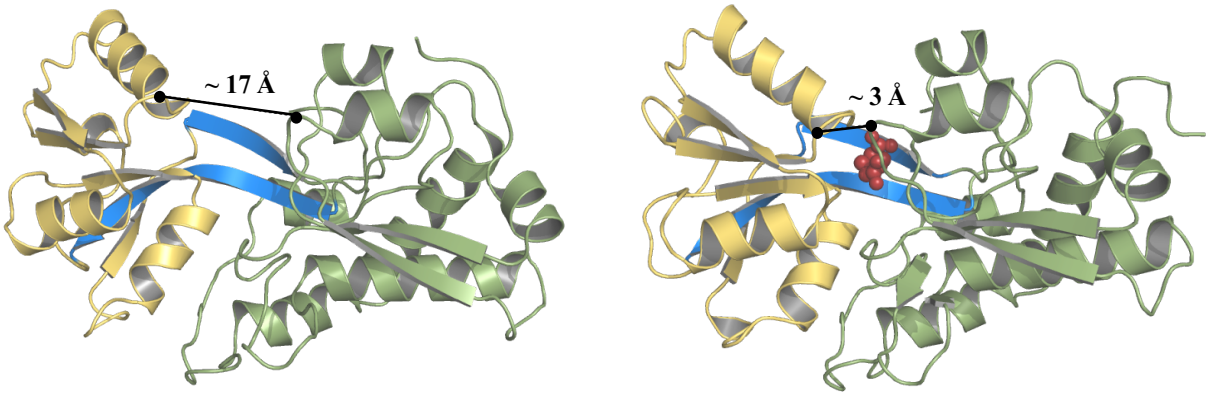

Figure 3.1. Protein structure (*ybeJ*) in the closed and open conformations. Domain A has yellow color, domain B is green. Amino acids Q73 and S137 were used to measure the distance between the two domains in apo (left) and bound (right) conformations and are indicated as small black spheres. The glutamate molecule in the bound structure is represented as red spheres.

To avoid dramatic changes in affinity, we investigated pairs of residues that participate in the apo to bound closure movement of the protein in the vicinity of glutamate. For this, we measured inter-residue distances between each residue from domain A and B (Figure 3.1). Residue pairs with probabilities to closely interact (within the distance of 3 Å) higher than 50 %

were excluded from the list of residues targeted for mutagenesis. This step was done in order to decrease the affinity, but to not disrupt the interaction. Figure 3.2 shows residues that were chosen for single-site mutagenesis.

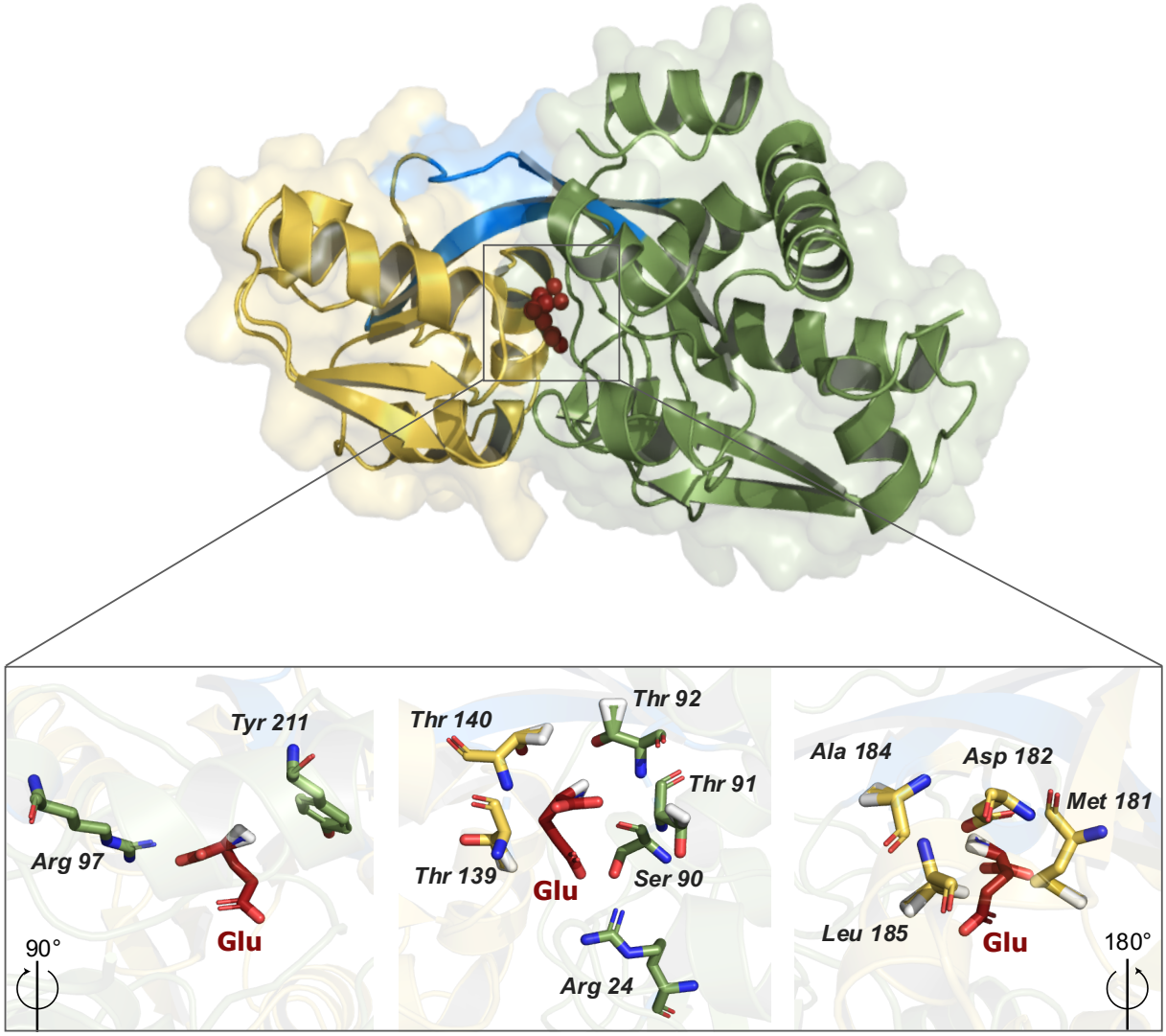

Figure 3.2. The glutamate binding pocket. The residues, represented as sticks, are located around the glutamate molecule (red stick) in a distance lower than 2 Å. Therefore, they are supposed to be involved in the glutamate binding action.

3.1.2 Effects of *in silico* mutagenesis on the binding free energy

To determine changes in glutamate binding affinities, we performed fast switching alchemical transformations (chapter 2.1.2) that enable us to mutate every targeted residue from the binding pocket. To save the electroneutrality of the system and to avoid dramatic changes in affinity,

residues were mutated to structures with the same charge. Tested combinations are given in Table 3.1.

For a quantitative evaluation of the effect of inserted mutations, we started a series of ~ 150 fast (5-10 ns) switching simulations in which the residue of interest was mutated following an alchemical path (chapter 2.1.2, Figure 2.2). After each run, the work performed on the system was estimated and from the distribution of the forward- and backward switching, the change in free energy as the intersection point of both distributions was calculated (Figure 3.3). The corresponding ΔΔG for all tested mutations, using data extracted from the analyses performed with pmx, were calculated, and summarized in Figure 3.4 and Table 3.1.

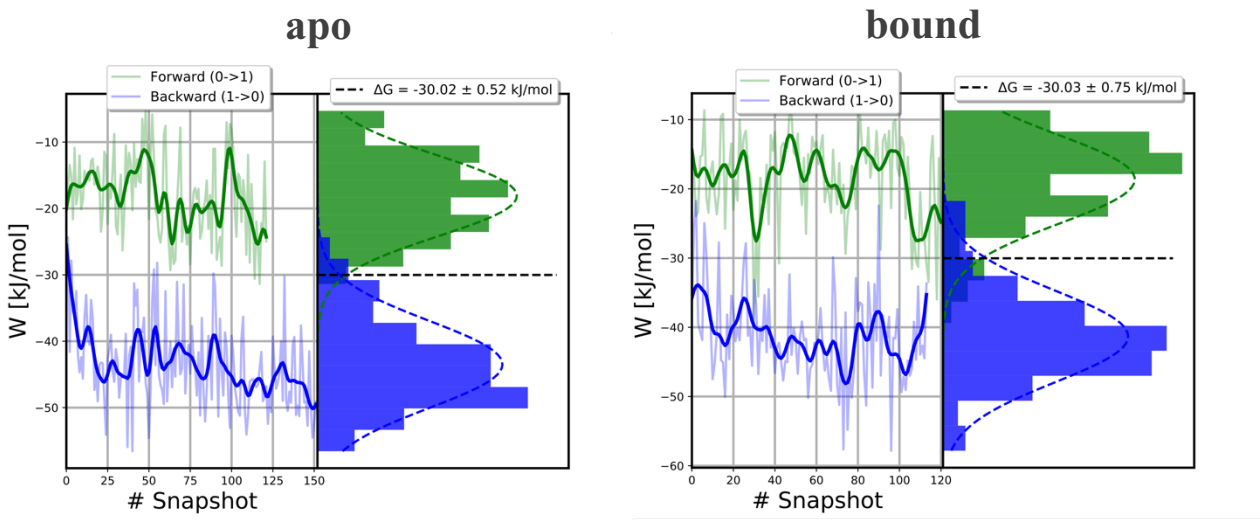

Figure 3.3. Example of the results from non-equilibrium transitions during alchemical transformation. The left section of each plot shows the work values for the rapid switching between amino acid sidechains as a function of the transition number (snapshots). The right region combines the work values into the work distribution histogram. The represented results belong to the mutant S90V.

The results demonstrate that among all variants, the biggest increase of glutamate binding free energy was caused by mutants A184W and T91V, suggesting the most pronounced effect on the protein affinity to glutamate. Consequently, these mutations were chosen for further investigations of their effect in experiments. Additionally, to test the correlation between simulation data and experiments, T92A and T92V variants were selected as well.

Table 3.1. List of mutations together with the calculated free energies after the *in silico* site-directed mutagenesis.

Residue	Mutation	ΔG_{apo} (kJ/mol)	ΔG_{bound} (kJ/mol)	$\Delta\Delta G$ (kJ/mol)
Arg 24	R24K	679.0 ± 0.7	678.1 ± 1.5	-0.9 ± 1.67
Ser 90	S90T	-81.6 ± 0.4	-90. ± 0.1	-9.4 ± 0.4
	S90V	-30.0 ± 0.5	-30.0 ± 0.78	-0.01 ± 0.9
	S90A	40.4 ± 0.2	42.9 ± 0.3	2.4 ± 0.3
	S90C	53.3 ± 0.3	47.5 ± 0.12	-5.8 ± 0.4
Thr 91	T91A	129.1 ± 0.6	158.3 ± 0.8	29.2 ± 1.0
	T91C	138.0 ± 0.7	155.8 ± 2.2	17.8 ± 2.3
	T91V	57.6 ± 0.8	106.9 ± 0.2	49.4 ± 0.9
	T91S	85.2 ± 0.2	88.4 ± 0.1	3.2 ± 0.2
Thr 92	T92A	119.7 ± 0.4	126.8 ± 0.1	7.1 ± 0.4
	T92C	133.7 ± 0.4	136.6 ± 0.4	2.8 ± 0.5
	T92V	50.3 ± 0.3	60.5 ± 0.5	10.2 ± 0.6
	T92S	79.0 ± 0.3	77.9 ± 0.3	-1.1 ± 0.4
Arg 97	R97K	665.3 ± 0.3	690.3 ± 0.6	25.0 ± 0.7
Thr 139	T139A	130.7 ± 0.5	136.2 ± 0.5	5.5 ± 0.7
	T139C	132.5 ± 0.2	148.6 ± 0.4	16.1 ± 0.4
	T139V	60.4 ± 0.4	69.5 ± 0.3	9.1 ± 0.5
	T139S	82.0 ± 0.2	80.6 ± 0.4	-1.5 ± 0.5
Thr 140	T140A	123.2 ± 0.2	136.7 ± 0.4	13.5 ± 0.4
	T140C	135.0 ± 0.3	138.9 ± 0.6	3.9 ± 0.6
	T140V	50.3 ± 0.2	56.7 ± 0.3	6.4 ± 0.4
	T140S	81.1 ± 0.1	90.1 ± 0.3	9.0 ± 0.3
Met 181	M181C	1.9 ± 0.5	12.2 ± 0.4	10.3 ± 0.6
Asp 182	D182E	31.3 ± 0.4	66.5 ± 3.4	35.3 ± 3.4
Ala 184	A184W	60.5 ± 1.7	162.2 ± 2.8	101.8 ± 3.2
Leu 185	L185I	77.8 ± 0.3	79.4 ± 0.6	1.6 ± 0.7
Tyr 211	Y211F	82.6 ± 0.3	98.5 ± 1.2	15.8 ± 1.3

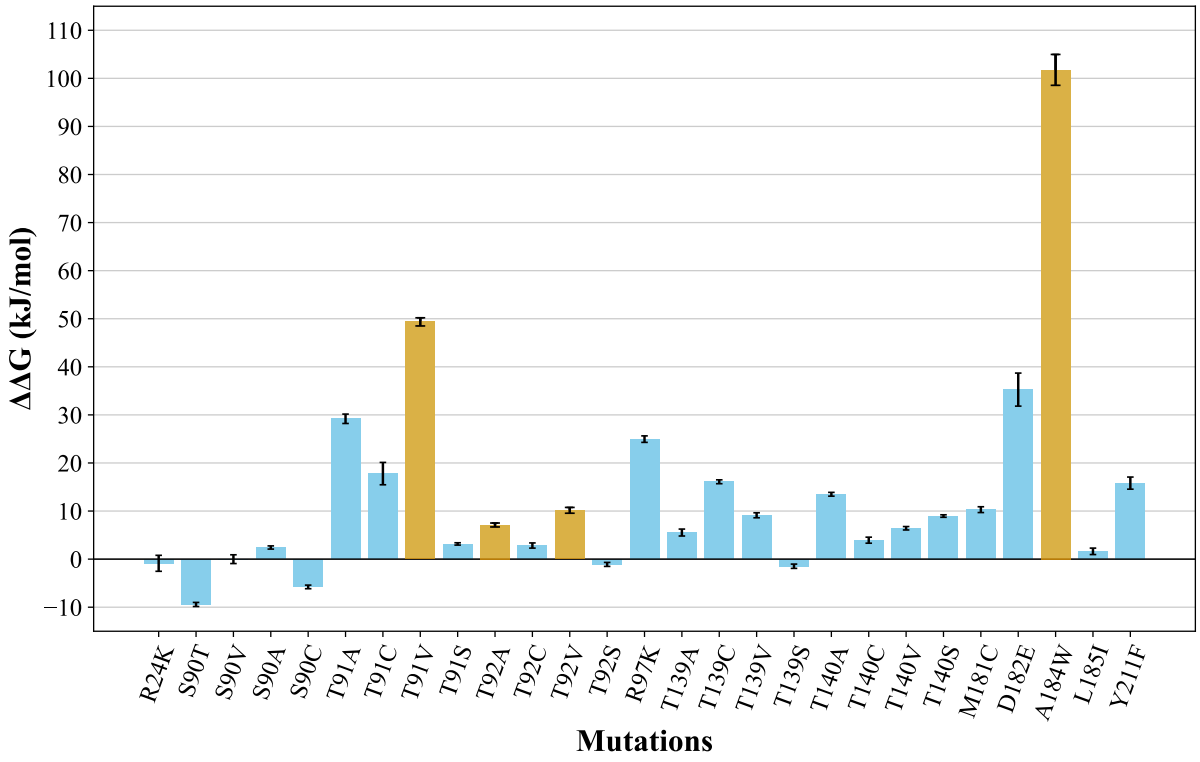

Figure 3.4. ΔΔG values of glutamate binding for alchemically induced mutants. The mutations highlighted in orange were selected for the experimental characterization.

3.1.3 Protein interaction with K^+ and Na^+ ions

We next addressed the potential role of K^+ and Na^+ ions in the glutamate binding process. For this purpose, the ions time-averaged density maps, derived from the MD simulations, were produced in proximity of the protein structure (≤ 3 Å) for apo and bound systems.

Density maps visualized in PyMol allowed me to spatially inspect the average location of atoms during a simulation and revealed regions with increased density of K^+ and Na^+ ions in apo and bound conformations, forming clusters around the protein structure (Figure 3.5, A). These increments in the density are an indication of a strong interaction between ions and the protein in the region of their localization. At first sight, the distribution of Na^+ ions clusters in the apo and bound states are similar. Perfect overlap for both conformational states was discovered for K^+ ions as well. More surprisingly, comparing the K^+ and Na^+ density maps, no significant differences in distribution around the protein structure was noticed (Figure 3.5, B, left). This observation suggest that the type of ion does not influence on the protein-salt interaction process and might not be involved in the glutamate binding process.

To confirm my assumption, I chose protein residues from ions clusters regions (Figure 3.5, B, right) and analyzed the amount of Na^+ and K^+ ions in the minimum distance from each

residue (≤ 3Å). The results, depicted in Figure 3.6, showed that the distribution of K^+ around every residue for the apo and bound states has very similar character, as that of Na^+. Moreover, the similarity in the distributions was also observed between K^+ and Na^+ plots for each residue.

Clearly, our observations lead us to the conclusion that the type of ions must not influence significantly on the protein-salt interaction and therefore on the protein affinity to glutamate, which should be further verified experimentally.

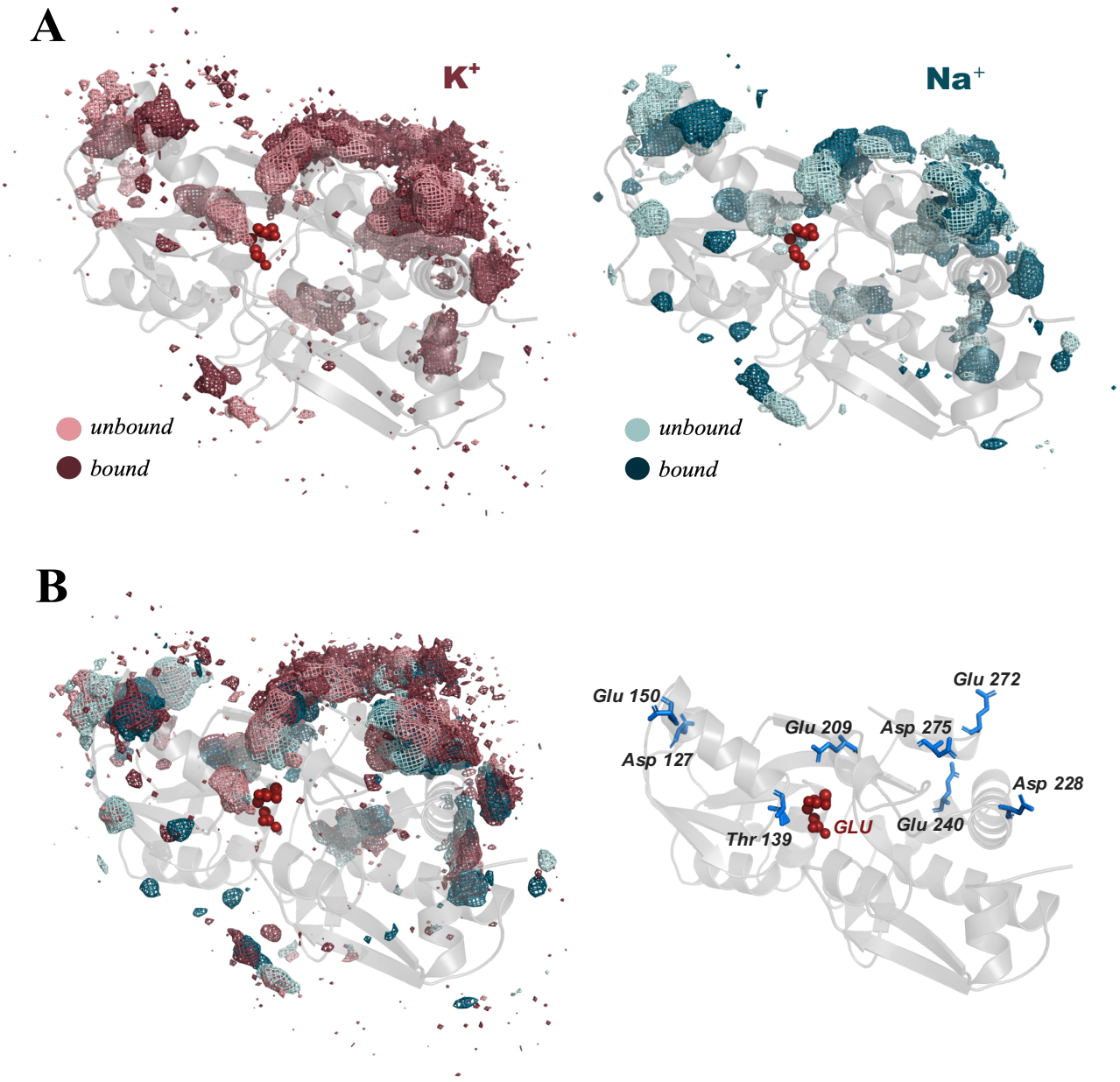

Figure 3.5. K^+ and Na^+ ions density maps. (A) K^+ (left) and Na^+ (right) ions density maps for the apo and bound states within 3 Å from the *ybeJ* structure (grey). The glutamate molecule is shown as red-sphere model. (B) Residues from the regions of ions clusters are represented as blue sticks.

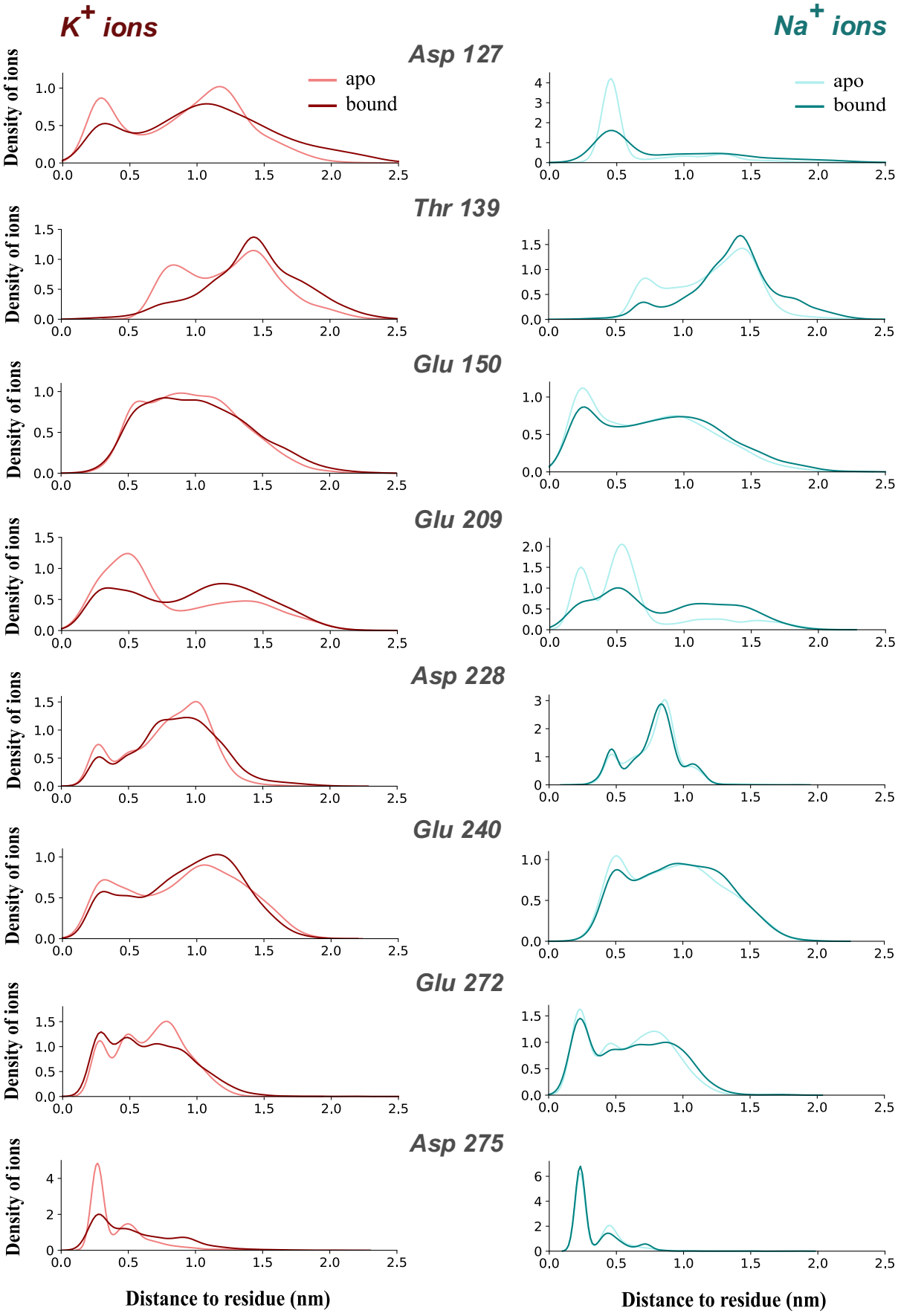

Figure 3.6. The minimum distance analysis of K^+/Na^+ ions from residues of interest.

3.2 Experimental characterization of Fl-GluBP and variants

All results predicted by MD simulations were corroborated by fluorescence measurements described in chapter 2.2.2.

3.2.1 Analysis of expression and labeling of the GluBP and variants

GluBP and its variants (A184W, T91V, T92A and T92V) were expressed in bacteria and purified by metal affinity followed by size-exclusion chromatography as described in chapter 2.2.1.2. All proteins were eluted as a monodispersed peak from the size exclusion chromatography without any sign of protein aggregation after freezing-defreezing process (Figure 3.7, A).

Chemically labelled GluBP and variants were scanned (Figure 3.7, B) to detect the fluorescence signal (chapter 2.2.1.3) and termed as Fl-GluBP-WT, Fl-GluBP-A184W, Fl-GluBP-T91V, Fl-GluBP-T92A and Fl-GluBP-T92V according to the mutated residue.

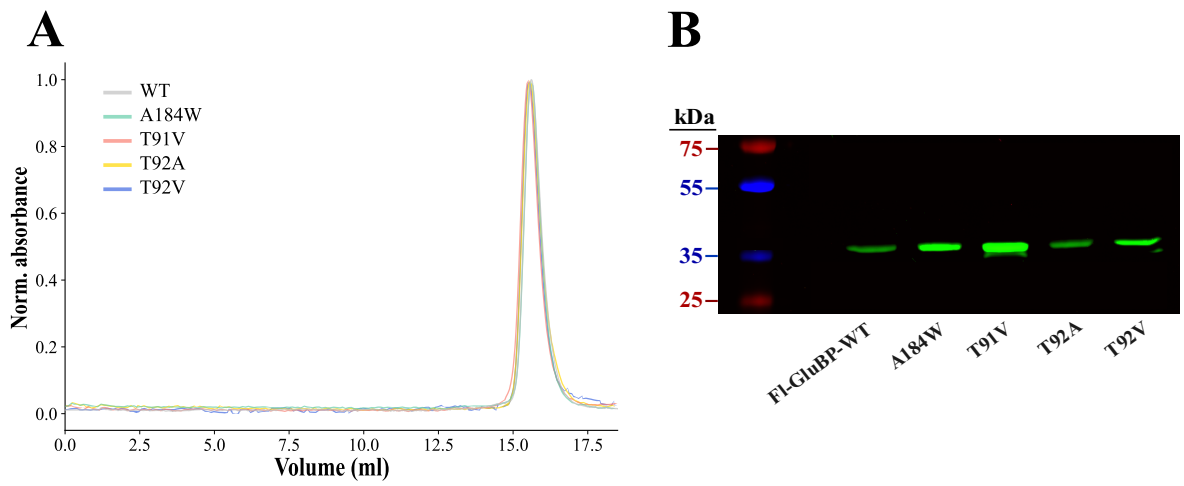

Figure 3.7. Purification and labeling analysis. (A) Size-exclusion chromatography profile of GluBP (WT) and variants (A184W, T91V, T92A and T92V) in HEPES 7.5 buffer. (B) SDS-PAGE scan of the IANBD-ester fluorophore labeled GluBP (Fl-GluBP-WT) and variants (A184W, T91V, T92A and T92V); lane 1 is molecular weight standards (kDa).

3.2.2 Glutamate affinity of Fl-GluBP and variants

I started the characterization of Fl-GluBP-WT and predicted in MD simulations four variants (Fl-GluBP-A184W, -T91V, -T92A and -T92V) from steady-state fluorescence spectroscopy

measurements (chapter 2.2.2.1), in order to study their affinity to glutamate. Experiments were performed at 20 °C and pH 7.5.

Addition of glutamate to Fl-GluBP-WT resulted in an increase in IANBD-ester emission (Figure 3.8, A), suggesting that the binding of glutamate to the protein results in a conformational change. The difference in the relative emission change between zero glutamate and the saturation point was estimated to be around 22 %. Determined from the equilibrium glutamate titration, WT's affinity to glutamate (K_d of 15.2 ± 2 µM with the Hill coefficient n ~ 1) (Figure 3.8, B; Table 3.2) was consistent with the previously determined value (9.7 ± 0.3 µM) [114].

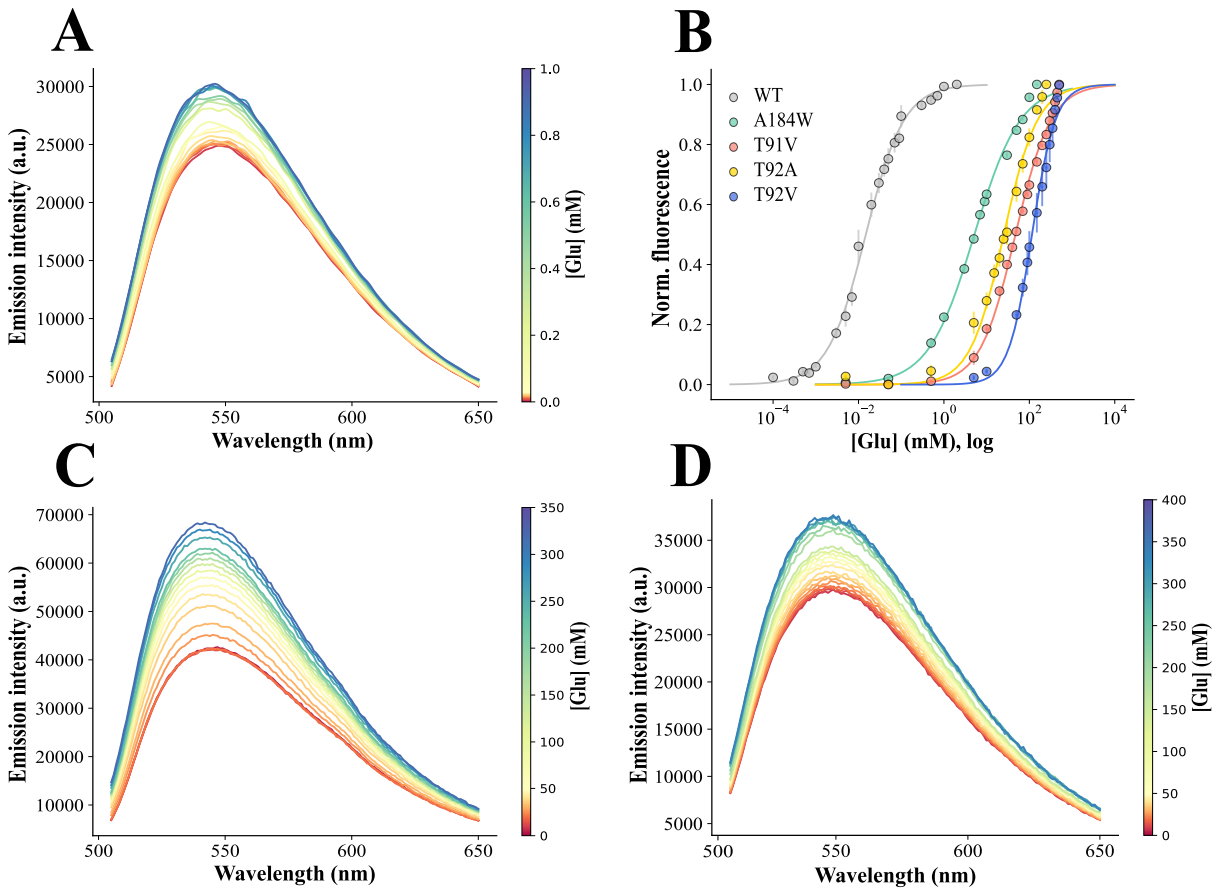

Figure 3.8. Characterization of the Fl-GluBP-WT and affinity mutants. (A, C, D) Emission spectra of Fl-GluBP-WT, -T91V and -T92V, respectively, with increasing glutamate concentrations. (B) Equilibrium glutamate binding titrations for Fl-GluBP-WT and -A184W, -T91V, -T92A, -T92V variants. Experiments were done at 20 °C, pH 7.5 in HEPES 7.5 buffer. Fluorescence changes are normalized to values between 0 and 1 and fitted to the Hill equation. Fitted curves are represented by solid lines overlaying the data points. Error bars represent SEM.

Mutants proposed by MD simulations decrease the protein´s affinity to glutamate, that could be observed as a shift of the titration curves on the semilogarithmic plot (Figure 3.8, B). Their respective dissociation constant values together with the Hill coefficients were calculated and summarized in the Table 3.2. Variants K_d increased in order of A184W < T92A < T91V < T92V. Compared to the Fl-GluBP-WT, the variants demonstrated a drastically decreased affinity to glutamate, that is associated with the K_ds increase from the μM to mM range. Moreover, the difference in the relative emission change for the Fl-GluBP-T91V was increased up to 70 %, while Fl-GluBP-T92V left this value close to Fl-GluBP-WT (23 %) (Figure 3.8, C and D, respectively). Cooperativity for glutamate remained independent, which is characterized by Hill coefficient values of ~ 1.

The equilibrium glutamate titration results revealed that the Fl-GluBP-T91V and -T92V, according to their K_d values (48.9 ± 2.0 mM and 119.4 ± 17.7 mM, respectively), have the lowest affinity to glutamate and therefore could be the best candidates for vesicular glutamate concentration measurements (Table 3.2). Consequently, these mutants were selected for a more detailed biophysical characterization.

Table 3.2. Affinity parameters of Fl-GluBP-WT, -A184W, -T91V, -T92A, -T92V for glutamate at 20 °C, pH 7.5. Fluorescence dynamic range is reported as fold enhancement by glutamate binding.

Protein	F_{+Glu}/F_{-Glu}	K_d	n
WT	1.19 ± 0.02	15.2 ± 2.0 μM	0.99 ± 0.05
A184W	1.55 ± 0.08	5.6 ± 0.5 mM	0.79 ± 0.03
T91V	1.71 ± 0.02	48.9 ± 2.0 mM	1.06 ± 0.05
T92A	1.92 ± 0.05	24.4 ± 2.2 mM	1.16 ± 0.05
T92V	1.16 ± 0.04	119.4 ± 17.7 mM	1.65 ± 0.09

3.2.3 Biophysical characterization of the law affinity mutants

Glutamate accumulation inside the acidified synaptic vesicle (pH ~ 5.8) is associated with changes of cations and anions concentrations (see chapter 1.3.4 and 1.3.5). Therefore, to investigate the effects of different environmental conditions, such as pH, temperature, salt type and its concentration, on affinity to glutamate of the low affinity mutants, I carried out the same steady-state fluorescence experiments but with some modified experimental conditions.

3.2.3.1 Temperature stability

To analyze the affinity of the Fl-GluBP-WT and the two low affinity variants (Fl-GluBP-T91V, Fl-GluBP-T92V) to glutamate under physiological conditions, glutamate titration measurements were performed at 37 °C, pH 7.5 (Figure 3.9). Comparison of affinities, summarized in the Table 3.3, at 20 and 37 °C revealed that the K_d significantly increased with increasing temperature only for the T91V mutant, from 48.9 ± 2.0 mM to 203.3 ± 7.6 mM. In contrast, K_d values for the Fl-GluBP-WT remained within 15 µM, demonstrating an absolutely temperature independent behavior. At the same time, Fl-GluBP-T92V had negligible increase in K_d values, from 119.4 ± 17.7 mM to 93.4 ± 8.9 mM, where the values and errors are correlated within the order of magnitude.

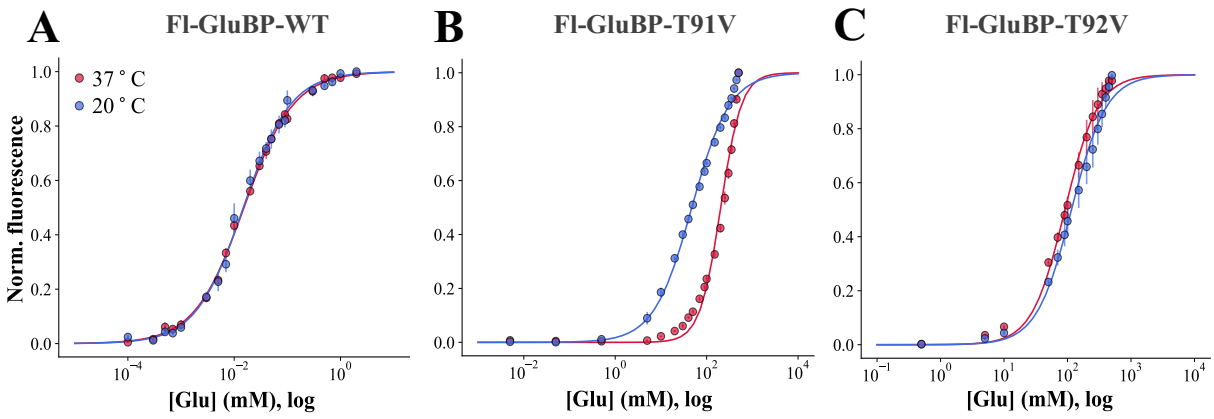

Figure 3.9. The temperature stability studies. Glutamate binding titrations for (A) Fl-GluBP-WT and (B, C) the low affinity mutants (Fl-GluBP-T91V, -T92V). Experiments were done at 20 and 37 °C, pH 7.5 in HEPES 7.5 buffer. Fluorescence changes are normalized to values between 0 and 1 and fitted to the Hill equation. Fitted curves are represented by solid lines overlaying the data points. Error bars represent SEM.

Table 3.3. Affinity parameters of Fl-GluBP-WT, Fl-GluBP-T91V, and Fl-GluBP-T92V for glutamate at 20 and 37 °C, pH 7.5. Fluorescence dynamic range is reported as fold enhancement by glutamate binding.

Protein	Temperature, °C	F_{+Glu}/F_{-Glu}	K_d	n
WT	20°C	1.19 ± 0.02	15.2 ± 2.1 µM	0.99 ± 0.05
	37°C	1.23 ± 0.003	15.4 ± 1.0 µM	0.93 ± 0.002
T91V	20°C	1.71 ± 0.02	48.9 ± 2.0 mM	1.06 ± 0.05
	37°C	1.70 ± 0.01	203.3 ± 7.6 mM	1.92 ± 0.06
T92V	20°C	1.17 ± 0.04	119.4 ± 17.7 mM	1.65 ± 0.09
	37°C	1.30 ± 0.11	93.4 ± 8.9 mM	1.74 ± 0.17

3.2.3.2 Salt dependency

The results from the equilibrium glutamate titration experiment of Fl-GluBP-WT and two low affinity mutants (Fl-GluBP-T91V and Fl-GluBP-T92V) in buffers with different NaCl and KCl salt contents at pH 5.8 are shown on Figure 3.10.

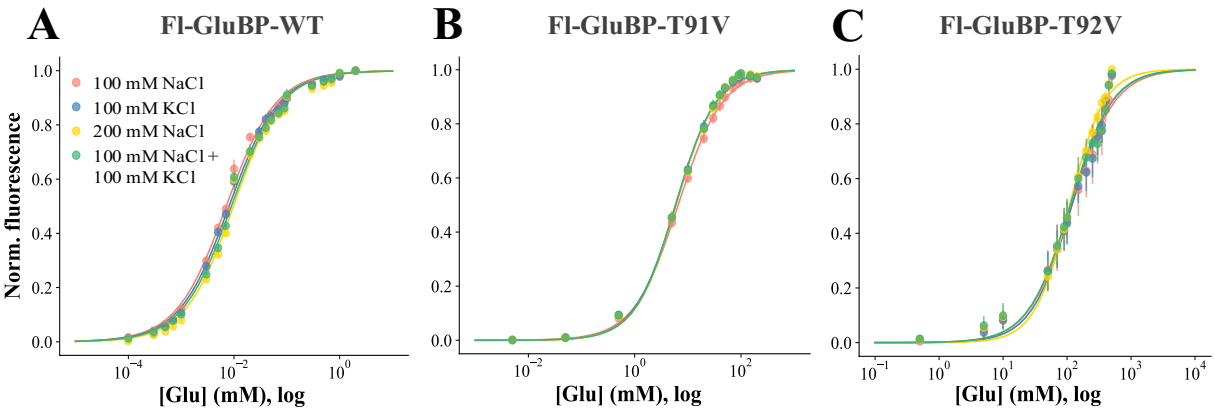

Figure 3.10. Salt dependency studies. Glutamate binding titrations for (A) Fl-GluBP-WT and (B, C) the low affinity mutants (Fl-GluBP-T91V, -T92V) in different concentrations of NaCl and KCl. Experimental conditions were 20°C and pH 5.8. Fluorescence changes are normalized to values between 0 and 1 and fitted to the Hill equation. Fitted curves are represented by solid lines overlaying the data points as the average of at least three experiments. Error bars represent SEM.

Inspection of the glutamate binding titration curves of the Fl-GluBP-WT (Figure 3.10, A) reveals no significant shift, which is a sign of the salt independent character of the glutamate binding process. Extracted after fitting K_d values (Table 3.4), are within 7-9 μM, confirming MD predictions about salt independent behavior of the WT.

More surprisingly, the inserted single mutations T91V and T92V, which affected the protein affinity to glutamate, preserved the salt independent character of WT with respect to glutamate binding. Once again, it can be observed from Figure 3.10 (B and C, respectively) as no shift in the titration curves and negligible differences in responsible K_ds values in the Table 3.4.

Table 3.4. Affinity parameters of Fl-GluBP-WT and low affinity variants Fl-GluBP-T91V and Fl-GluBP-T92V for glutamate in different concentrations of NaCl and KCl at 20 °C, pH 5.8. Fluorescence dynamic range is reported as fold enhancement by glutamate binding.

Protein	Salt	F_{+Glu}/F_{-Glu}	Kd	n
WT	100 mM NaCl	1.26 ± 0.02	7.1 ± 0.3 μM	0.92 ± 0.02
	100 mM KCl	1.25 ± 0.03	8.2 ± 0.8 μM	0.93 ± 0.03
	200 mM NaCl	1.27 ± 0.02	9.9 ± 0.7 μM	0.96 ± 0.05
	100 mM NaCl + 100 mM KCl	1.28 ± 0.02	9.1 ± 0.8 μM	0.93 ± 0.03
T91V	100 mM NaCl	2.50 ± 0.05	6.4 ± 0.6 mM	1.03 ± 0.03
	100 mM KCl	2.38 ± 0.09	5.9 ± 0.6 mM	1.11 ± 0.03
	200 mM NaCl	2.47 ± 0.11	5.6 ± 0.5 mM	1.10 ± 0.02
	100 mM NaCl + 100 mM KCl	2.47 ± 0.10	5.9 ± 0.4 mM	1.11 ± 0.04
T92V	100 mM NaCl	1.18 ± 0.05	92.0 ± 12.4 mM	1.54 ± 0.20
	100 mM KCl	1.17 ± 0.05	92.3 ± 14.9 mM	1.56 ± 0.24
	200 mM NaCl	1.15 ± 0.05	90.0 ± 18.5 mM	1.70 ± 0.28
	100 mM NaCl + 100 mM KCl	1.15 ± 0.04	88.7 ± 18.8 mM	1.49 ± 0.21

3.2.3.3 pH stability

We then proceed in investigating the effect of pH on the affinity of Fl-GluBP-WT and Fl-GluBP-T91V, Fl-GluBP-T92V affinity mutants to glutamate. The pH stability was studied through glutamate binding titrations in solutions at different pHs ranging from 5.5 to 8.0 at 20 °C. The observed equilibrium curves are shown in Figure 3.11.

Fl-GluBP-WT, according to a slight shift of the titration curves and determined K_d values (Table 3.5) within 8.2 µM - 23.3 µM, demonstrated a slightly pH dependent behavior.

In experiments with Fl-GluBP-T91V we observed that the pH had a drastic effect on protein (Figure 3.11, B), changing the K_d value ~ 3 times in the pH 5.5 - 8.0 range, from 3.1 to 65.2 mM. Such a result has questioned the applicability of this variant as a sensor for glutamate measurements inside synaptic vesicles. However, the K_d value at pH 7.5, determined to be 47.4 ± 2.1 mM, allows this sensor to be promising for glutamate measurements in the neuronal cytoplasm.

In contrast, Fl-GluBP-T92V was less pH sensitive than Fl-GluBP-WT and -T91V (Figure 3.11, C). Calculated K_ds together with Hill coefficients are listed in the Table 3.5 and are correlated within error.

Together obtained results let us to consider the Fl-GluBP-T92V as the best candidate sensor for glutamate measurements inside synaptic vesicles.

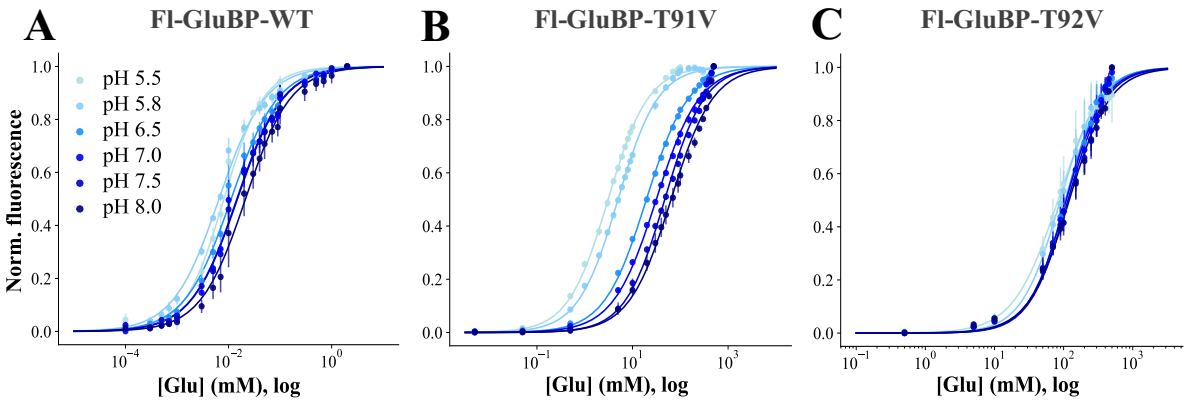

Figure 3.11. pH stability studies. Equilibrium glutamate binding titrations for the (A) Fl-GluBP-WT and (B, C) low affinity variants (Fl-GluBP-T91V and -T92V) at different pH values and 20 °C. Fluorescence changes are normalized to values between 0 and 1 and fitted to the Hill equation. Fitted curves are represented by solid lines overlaying the data points. Error bars represent SEM.

Table 3.5. Affinity parameters of Fl-GluBP-WT and low affinity variants Fl-GluBP-T91V and Fl-GluBP-T92V for glutamate at 20 °C. Fluorescence dynamic range is reported as fold enhancement by glutamate binding.

Protein	pH	F_{+Glu}/F_{-Glu}	Kd	n
WT	5.5	1.10 ± 0.04	8.2 ± 0.7 μM	1.16 ± 0.09
	5.8	1.26 ± 0.02	7.1 ± 0.3 μM	0.92 ± 0.02
	6.5	1.26 ± 0.05	11.7 ± 2.5 μM	0.98 ± 0.01
	7.0	1.22 ± 0.05	15.3 ± 3.4 μM	1.01 ± 0.06
	7.5	1.19 ± 0.02	15.2 ± 2.1 μM	0.99 ± 0.05
	8.0	1.21 ± 0.02	23.3 ± 7.7 μM	1.03 ± 0.01
T91V	5.5	2.64 ± 0.06	3.1 ± 0.1 mM	1.04 ± 0.02
	5.8	2.50 ± 0.05	6.4 ± 0.6 mM	1.03 ± 0.03
	6.5	2.18 ± 0.01	20.1 ± 0.3 mM	0.97 ± 0.02
	7.0	1.87 ± 0.02	31.5 ± 0.7 mM	0.97 ± 0.03
	7.5	1.71 ± 0.02	48.9 ± 2.0 mM	1.06 ± 0.05
	8.0	1.69 ± 0.04	65.2 ± 29.0 mM	1.01 ± 0.06
T92V	5.5	1.14 ± 0.06	89.7 ± 17.5 mM	1.53 ± 0.08
	5.8	1.18 ± 0.05	92.0 ± 12.4 mM	1.54 ± 0.20
	6.5	1.16 ± 0.05	108.1 ± 9.9 mM	1.72 ± 0.12
	7.0	1.17 ± 0.05	114.7 ± 18.4 mM	1.72 ± 0.15
	7.5	1.17 ± 0.04	119.4 ± 17.7 mM	1.65 ± 0.09
	8.0	1.16 ± 0.04	122.1 ± 16.0 mM	1.52 ± 0.14

3.2.3.4 Fl-GluBP-T91V ligand selectivity

From the aforementioned results, we suggested that Fl-GluBP-T91V sensor could be used for cytoplasmic glutamate measurements. Therefore, the sensitivity to aspartate, which has been identified as a co-neurotransmitter with glutamate in some neurons [180], must be considered and characterized.

To determine the specificity of this mutant and Fl-GluBP-WT, I titrated proteins against the aspartate at the same conditions as they were for the glutamate titration experiments (20 °C

and pH 7.5). The results showed that Fl-GluBP-WT has a K_d of 25.2 ± 5.82 mM for aspartate, demonstrating a highly selective behavior for glutamate (K_d is 15.2 ± 2.1 μM) over aspartate (Figure 3.12, A; Table 3.6), firstly described by Coates et al. [114].

The examination of Fl-GluBP-T91V indicated an affinity of 52.6 ± 6.0 mM for aspartate, which in comparison with the previously determined K_d for glutamate (48.9 ± 2.0 mM), revealed equal selectivity for both ligands (Figure 3.12, B; Table 3.6). However, due to the inability to reach a plateau because of experimental limitations we cannot be sure in this conclusion. Moreover, the resulted apparent K_d value appears higher than glutamate concentration in the neuronal cytoplasm that is reported to be within 10 - 15 mM [31]. Therefore, to explore the utility of this sensor in the cytoplasmic glutamate measurements I carried out fluorescence lifetime measurements, which are discussed in chapter 3.2.4.

Additionally, I studied salt dependency of the Fl-GluBP-T91V mutation at physiological neuronal pH ~ 7.5 in buffers with different NaCl and KCl salt contents (Figure 3.12, C). Extracted after fitting K_d values (Table 3.7), determined to be within 50 mM, once again suppose salt independent character of the Fl-GluBP-T91V variant.

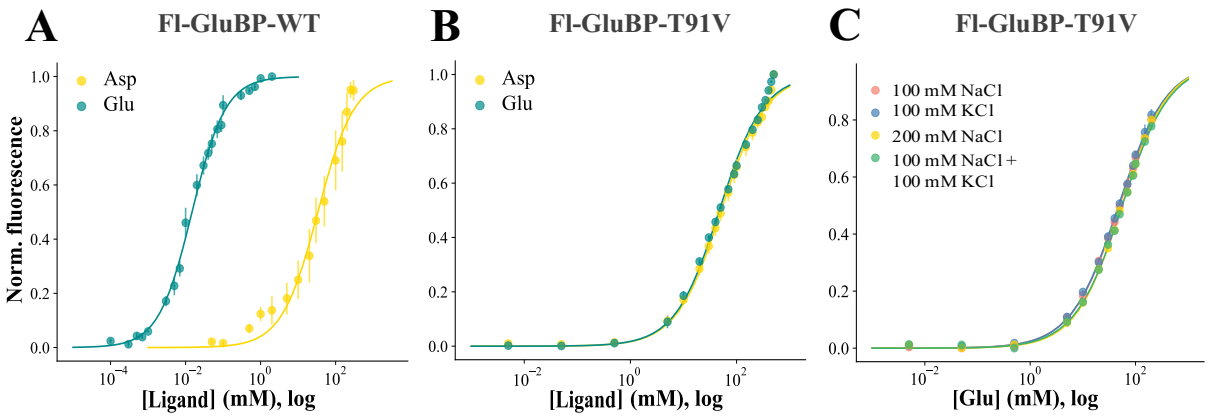

Figure 3.12. Ligand selectivity and salt dependency studies at pH 7.5. Equilibrium glutamate and aspartate binding titrations for (A) the Fl-GluBP-WT and (B) low affinity variant Fl-GluBP-T91V. (C) Glutamate binding titrations for low affinity mutant Fl-GluBP-T91V in different concentrations of NaCl and KCl. Experiments were done at 20 °C, pH 7.5 in HEPES 7.5 buffer. Fluorescence changes are normalized to values between 0 and 1 and fitted to the Hill equation. Fitted curves are represented by solid lines overlaying the data points. Error bars represent SEM.

Table 3.6. Affinity and selectivity of Fl-GluBP-WT and Fl-GluBP-T91V for glutamate and aspartate at 20 °C, pH 7.5. Fluorescence dynamic range is reported as fold enhancement by aspartate or glutamine ligand binding.

Protein	Ligand	F_{+Glu}/F_{-Glu}	K_d	n
WT	Glutamate	1.19 ± 0.02	15.2 ± 2.1 μM	0.99 ± 0.05
	Aspartate	1.03 ± 0.01	25.2 ± 5.8 mM	0.90 ± 0.10
T91V	Glutamate	1.71 ± 0.02	48.9 ± 2.0 mM	1.06 ± 0.05
	Aspartate	1.42 ± 0.03	52.6 ± 6.0 mM	1.05 ± 0.04

Table 3.7. Affinity parameters of low affinity variant Fl-GluBP-T91V for glutamate in different concentrations of NaCl and KCl at 20 °C, pH 7.5. Fluorescence dynamic range is reported as fold enhancement by glutamate binding.

Protein	Salt	F_{+Glu}/F_{-Glu}	K_d	n
T91V	100 mM NaCl	1.71 ± 0.02	48.9 ± 2.0 mM	1.06 ± 0.05
	100mM KCl	1.75 ± 0.03	46.7 ± 2.8 mM	1.11 ± 0.02
	200 mM NaCl	1.76 ± 0.03	53.3 ± 2.3 mM	1.10 ± 0.02
	100mM NaCl + 100 mM KCl	1.74 ± 0.001	54.3 ± 1.6 mM	1.09 ± 0.003

3.2.3.5 Kinetic studies

Glutamate binding in Fl-GluBP (-WT) sensor has a two-step mechanism [114]: initial rapid glutamate binding and subsequent conformational change. In order to investigate how low affinity mutations T91V and T92V affect these two processes I used fast-mixing fluorescence stopped-flow technique (chapter 2.2.2.2). Association kinetic experiments were held with a series of glutamate concentrations at pH 7.5 and 5 °C (the reaction was slowed down enough to be observable).

For all measured proteins (Fl-GluBP-WT, -T91V and -T92V) I observed a fluorescence increase in response to glutamate application (Figure 3.13, left). The highest relative change in fluorescence was demonstrated again by the Fl-GluBP-T91V. By fitting all signals with a single

exponential function, I extracted values for the association rate constants (k_{obs}) and plotted them as a function of glutamate concentration (Figure 3.13, right).

The association rate of the Fl-GluBP-WT increased until reaching a plateau at ~ 600 s^{-1} that gives a hyperbolic appearance to the plot (Figure 3.13, A, right). Such a pattern of the association rate plot was interpreted in terms of a two-step mechanism, in which the rapid glutamate binding is followed by conformation (induced-fit mechanism [169]). The best fit parameters to the hyperbole are represented in the Table 3.8, giving an apparent K_d of 21.0 ± 4.4 μM, comparable to values measured by steady-state fluorescence (15.2 ± 2.1 μM) and satisfactorily reproduce published results [114].

Fluorescence amplitudes of the Fl-GluBP-T91V and -T92V also increased with saturating [glutamate] dependence, in agreement with an induced-fit mechanism. As expected, both mutations reduce the glutamate affinity by more than 1000 times, which is confirmed by a K_d of 22.7 ± 3.4 mM for Fl-GluBP-T91V and 91.3 ± 29.7 mM for Fl-GluBP-T92V (Figure 3.13, D; Table 3.8). This is a sign of tighter initial glutamate binding in Fl-GluBP-WT than in these mutants [181]. There are additional changes in the subsequent conformational step. The association rate plots, plateauing at ~ 80 and ~ 50 s^{-1} for Fl-GluBP-T91V and -T92V mutation, respectively, lead to the assumption that the rate of subsequent conformational change in these mutants is slowed down in comparison to the Fl-GluBP-WT (Figure 3.13, B and C, right). The smaller forward rates (k_1) of the conformational change for Fl-GluBP-T91V and -T92V, comparing to the Fl-GluBP-WT, additionally contribute to the low affinities of the mutants to glutamate. The backward rate constant values (k_2) for Fl-GluBP-T91V and -T92V appeared smaller than for Fl-GluBP-WT as well, that allows us to conclude that glutamate in these mutants exhibits higher rates of establishing induced fit and the lower rates back to the loosely bound state. The best fit values to the data are summarized in Table 3.8.

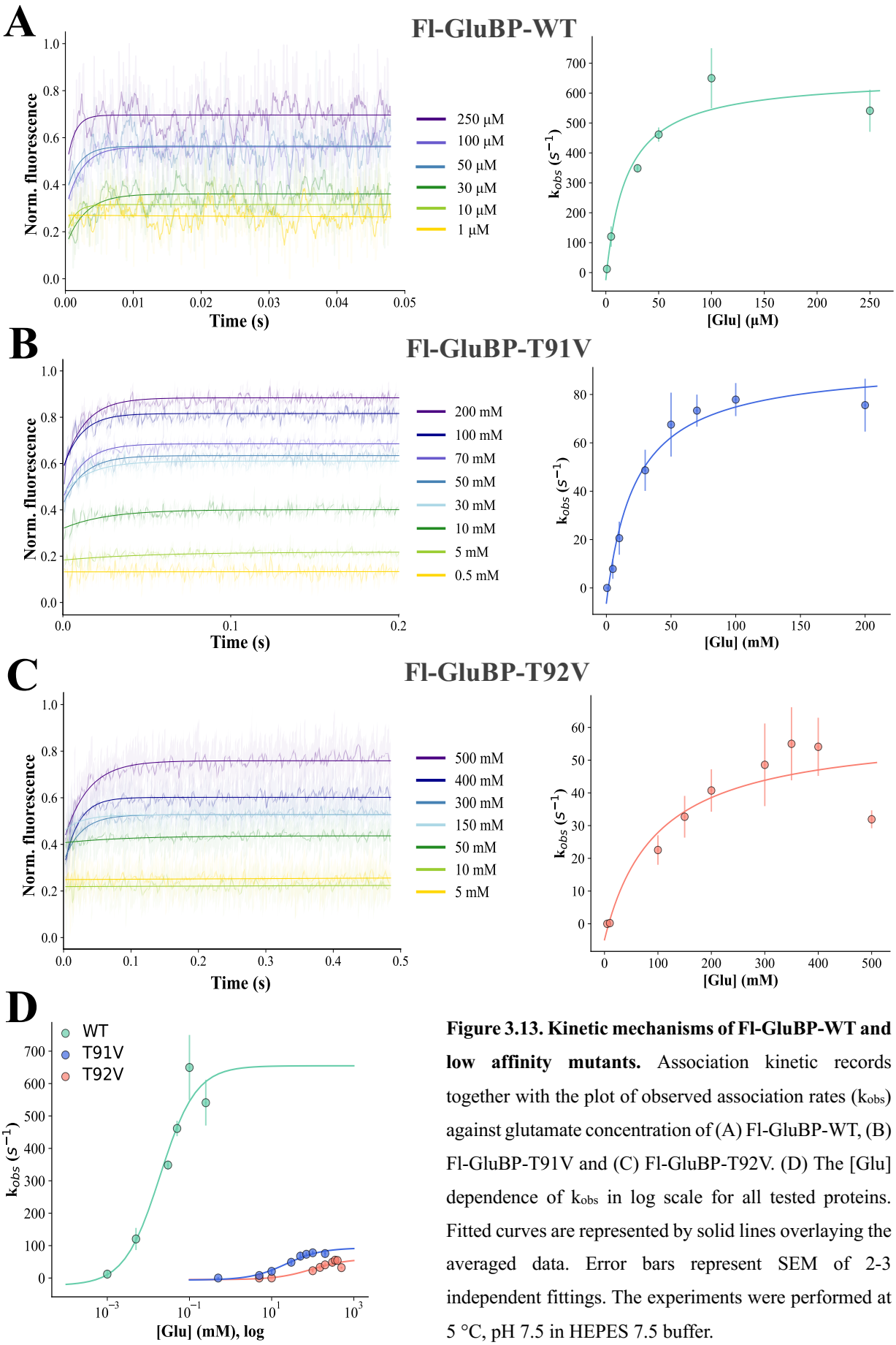

Figure 3.13. Kinetic mechanisms of Fl-GluBP-WT and low affinity mutants. Association kinetic records together with the plot of observed association rates (k_{obs}) against glutamate concentration of (A) Fl-GluBP-WT, (B) Fl-GluBP-T91V and (C) Fl-GluBP-T92V. (D) The [Glu] dependence of k_{obs} in log scale for all tested proteins. Fitted curves are represented by solid lines overlaying the averaged data. Error bars represent SEM of 2-3 independent fittings. The experiments were performed at 5 °C, pH 7.5 in HEPES 7.5 buffer.

Table 3.8. Kinetic parameters of Fl-GluBP-WT, -T91V and -T92V. Rate constants were calculated by fitting the measurements in Figure 3.13. The errors represent the SEM of 2-3 independent fittings. The experiments were performed at 5 °C and pH 7.5.

Protein	k_1 (s^{-1})	k_2 (s^{-1})	K_d
WT	682.4 ± 28.8	20.2 ± 37.4	21.0 ± 4.4 μM
T91V	99.8 ± 3.4	6.8 ± 0.9	22.7 ± 3.4 mM
T92V	64.9 ± 14.7	5.4 ± 0.3	91.3 ± 29.7 mM

3.2.4 Lifetime measurements

We tested whether it is possible to use fluorescence lifetime measurements (chapter 2.2.2.3) to obtain absolute glutamate concentrations with our sensors. Since changes in glutamate homeostasis appear to contribute to the pathophysiology of various human diseases (chapter 1.5), such tools are urgently needed.

To study the change in the lifetime of the IANBD-ester fluorophore upon the glutamate binding process, the fluorescence decays of the Fl-GluBP-WT and low affinity mutants (Fl-GluBP-T91V and -T92V) were measured in the absence and presence of saturating glutamate concentration (Figure 3.14) at pH 5.8 and 7.5. By fitting experimental traces, we extracted the values of fluorescence lifetimes and amplitudes, and used them to calculate the corresponding average fluorescence lifetime (τ_{ave}). All fit values are summarized in Table 3.9 and 3.10.

At pH 5.8, average fluorescence lifetimes of Fl-GluBP-T91V increased from 1.4 to 4.6 ns at the maximum glutamate concentration (Table 3.10), indicating that the fluorescence lifetime has glutamate concentration-dependent behavior and upon the glutamate binding could be increased to about 240 %. These results demonstrate that the Fl-GluBP-T91V sensor could be used to investigate absolute glutamate concentration changes in real time monitoring measurements. In contrast, Fl-GluBP-WT and -T92V fluorescence lifetimes increased only by 42 - 44 % at maximum glutamate level. Such a barely noticeable changes in fluorescence limits Fl-GluBP-T92V sensor suitability in experiments. Similar measurements were carried out at pH 7.5. The obtained results showed a pH-dependent behavior of the Fl-GluBP-WT and low affinity variant Fl-GluBP-T91V, which was confirmed by the fluorescence lifetime increase to

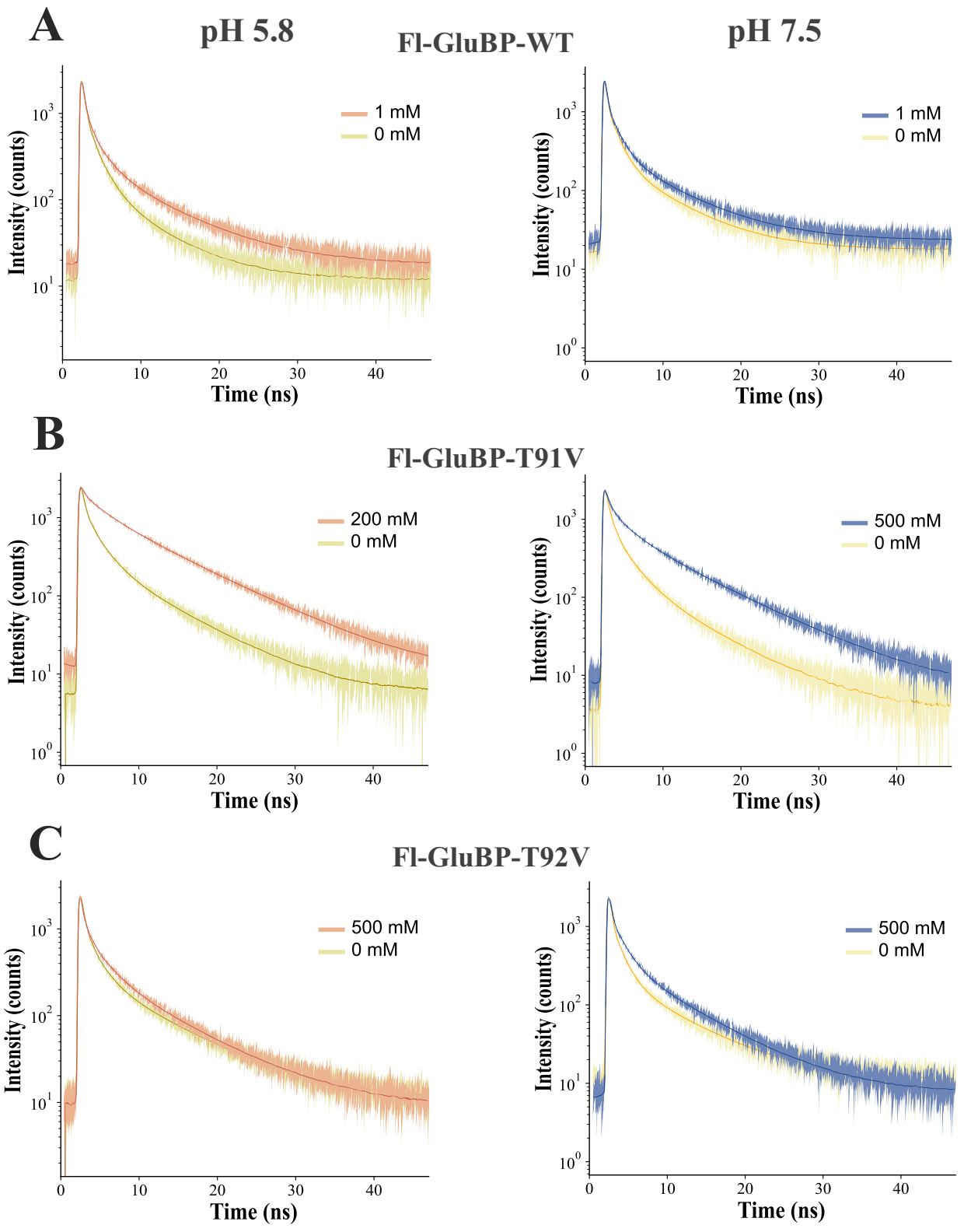

Figure 3.14. Fluorescence decays of Fl-GluBP-WT, -T91V and -T92V as a function of glutamate concentration. Represented measurements were held at pH 5.8 (left column) and pH 7.5 (right column) for (A) Fl-GluBP-WT, (B) Fl-GluBP-T91V and (C) Fl-GluBP-T92V in the absence and presence (saturation) of glutamate. Fitted curves are represented by solid lines overlaying measured data. Experiments were held at 27 °C.

about 125 % for Fl-GluBP-T91V, 53 % for Fl-GluBP-T92V and 17 % for Fl-GluBP-WT (Table 3.9).

These results make Fl-GluBP-T91V a candidate sensor to quantify resting glutamate concentrations in the neuronal and glial cytoplasm. However, the low selectivity between glutamate and aspartate (chapter 3.2.3.4) and the high apparent K_d value for glutamate at pH 7.5 (~ 49 mM, chapter 3.2.3.3) limit its suitability. We therefore performed additional measurements of fluorescence decays at different concentrations of glutamate and aspartate at pH 7.5 (Figure 3.15, A and B). The fluorescence lifetimes and their amplitudes together with the calculated τ_{ave}s are listed in Table 3.11 and 3.12. The averaged lifetime plotted against the ligand concentration shows a glutamate and aspartate concentration dependent behavior for the Fl-GluBP-T91V sensor (Figure 3.15, C). Fitted with a Hill function titration curves provided K_d values of 99.7 ± 8.6 mM for aspartate and 44.7 ± 1.2 mM for glutamate, consistent with the values measured in the previous chapter. Moreover, glutamate causes bigger change in fluorescence lifetime (over 100 %) than aspartate (~ 50 %). However, this selectivity of the sensor is nor sufficient to exclude contributions of aspartate in fluorescence during glutamate measurements in an environment where both ligands are present. In addition, the analysis of fluorescence lifetime under the glutamate binding in cytoplasmic glutamate concentration range [31] showed the increase up to ~ 30 % (Figure 3.15, D and E). This result showed that despite high K_d value, Fl-GluBP-T91V sensor can report on smaller glutamate concentrations. On the other hand, in neuronal or glial cytoplasm, where both glutamate and aspartate are present, Fl-GluBP-T91V could yield composite signal due to its fluorescence dynamic range for both ligands at physiological concentration range (Figure 3.15, F). Improved selectivity to glutamate over aspartate could make the Fl-GluBP-T91V an ideal candidate sensor for cytoplasmic absolute glutamate concentrations measurements. We hope that this goal can be achieved by additional mutations in our future work.

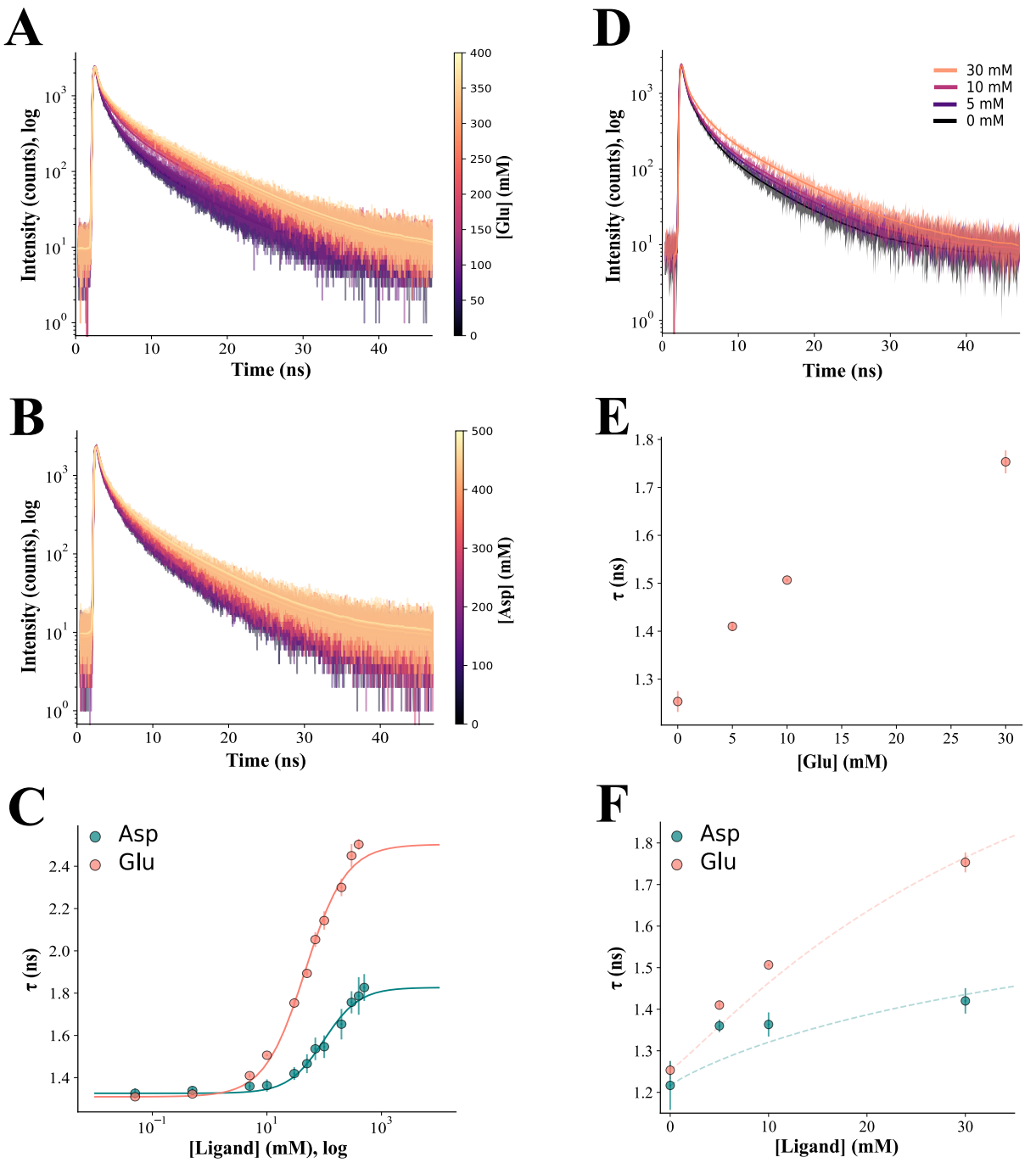

Figure 3.15. Fluorescence decays of Fl-GluBP-T91V as a function of glutamate and aspartate concentration. Measured fluorescence decays as a function of (A) glutamate and (B) aspartate concentration. (C) The averaged lifetime (τ_{ave}) against ligand concentrations plot. Fitted curves are represented by solid lines overlaying data points. (D) Fluorescence decays as a function of glutamate at cytoplasmic glutamate range. (E) τ_{ave} dependency of glutamate, (F) glutamate and aspartate concentrations at cytoplasmic ligands range. The dashed lines display τ_{ave} tendency upon ligand concentration increase. Error bars represent SEM of 3 independent fittings. Experiments were held at 27 °C and pH 7.5.

Table 3.9. Parameters from fluorescence lifetime measurements of Fl-GluBP-WT, -T91V and -T92V as a function of glutamate at pH 7.5. The values were calculated by fitting the measurements in Figure 3.14. The experiments were held at 27 °C in HEPES 7.5 buffer.

Glutamate (mM)	τ_1 (ns)	τ_2 (ns)	τ_3 (ns)	τ_4 (ns)	A_1 (cnts)	A_2 (cnts)	A_3 (cnts)	A_4 (cnts)	τ (ns)	R^2
WT										
0 mM	7.12	1.71	0.42	0.02	194.54	838.2	2336	20840	1.13	1.01
1 mM	7.71	1.85	0.43	0.02	258.43	782.4	2317	19970	1.32	0.99
T91V										
0 mM	7.25	2.07	0.51	0.02	241.32	848.1	2413	20680	1.35	0.96
500 mM	8.73	2.62	0.56	0.02	783.3	780.8	1663	18700	3.04	1.03
T92V										
0 mM	7.42	1.57	0.40	0.02	209.24	828.9	2622	22330	1.06	0.99
500 mM	7.82	2.15	0.48	0.02	318.01	790.7	2082	25480	1.62	0.98

Table 3.10. Parameters from fluorescence lifetime measurements of Fl-GluBP-WT, T91V and T92V as a function of glutamate at pH 5.8. The values were calculated by fitting the measurements in Figure 3.14. The experiments were held at 27 °C in MES 5.8 buffer.

Glutamate (mM)	τ_1 (ns)	τ_2 (ns)	τ_3 (ns)	τ_4 (ns)	A_1 (cnts)	A_2 (cnts)	A_3 (cnts)	A_4 (cnts)	τ (ns)	R^2
WT										
0 mM	6.37	1.62	0.39	0.02	163.86	817.5	2097	25090	1.04	0.97
1 mM	7.96	1.86	0.42	0.02	272.96	676.2	1877	30990	1.50	0.99
T91V										
0 mM	7.41	1.92	0.41	0.02	345.7	1090.3	2906	0	1.35	0.96
200 mM	9.08	3.36	0.60	0.02	1262.5	808.8	1157	7430	4.61	1.03
T92V										
0 mM	8.31	1.76	0.42	0.03	304.20	855.2	2289	15630	1.45	0.97
500 mM	8.25	2.27	0.48	0.03	373.30	716.6	1559	23920	2.06	0.98

Table 3.11. Parameters from fluorescence lifetime measurements of Fl-GluBP-T91V as a function of glutamate. The values were calculated by fitting the measurements in Figure 3.15. The experiments were held at 27 °C, pH 7.5 in HEPES 7.5 buffer.

Glutamate (mM)	τ_1 (ns)	τ_2 (ns)	τ_3 (ns)	τ_4 (ns)	A_1 (cnts)	A_2 (cnts)	A_3 (cnts)	A_4 (cnts)	τ (ns)	R^2
0	7.24 ± 0.10	2.09 ± 0.06	0.47 ± 0.01	0.03	238.42 ± 1.05	832.73 ± 4.68	2705.00 ± 9.24	6426.67 ± 410.74	1.25 ± 0.02	0.95 ± 0.01
0.005	7.08 ± 0.07	1.98 ± 0.05	0.46 ± 0.01	0.03	271.13 ± 11.02	888.43 ± 27.38	2637.67 ± 49.08	6540.00 ± 680.22	1.29 ± 0.02	0.96 ± 0.01
0.05	7.09 ± 0.09	1.97 ± 0.05	0.46 ± 0.01	0.03	278.87 ± 8.97	898.03 ± 16.92	2581.67 ± 15.72	6906.67 ± 337.75	1.31 ± 0.01	0.97 ± 0.01
0.5	7.05 ± 0.07	1.94 ± 0.03	0.45 ± 0	0.03	290.92 ± 7.56	905.43 ± 8.83	2548.67 ± 28.71	6886.67 ± 230.96	1.32 ± 0.01	0.98 ± 0.01
5	7.50 ± 0.13	2.03 ± 0.07	0.45 ± 0	0.03	310.03 ± 15.16	883.67 ± 29.31	2532.67 ± 31.86	7486.67 ± 674.05	1.41 ± 0.01	0.97 ± 0
10	7.60 ± 0.09	2.03 ± 0.05	0.46 ± 0.01	0.03	352.64 ± 9.04	882.30 ± 28.53	2473.00 ± 27.62	7233.33 ± 811.94	1.51 ± 0	0.98 ± 0.01
30	7.85 ± 0.13	2.06 ± 0.09	0.46 ± 0.01	0.03	356.13 ± 16.37	891.13 ± 38.94	2359.67 ± 28.98	6080.00 ± 625.06	1.75 ± 0.02	0.99 ± 0.01
50	8.07 ± 0.10	2.13 ± 0.07	0.46 ± 0.01	0.03	502.10 ± 12.57	881.70 ± 24.51	2304.67 ± 25.83	6286.67 ± 708.39	1.89 ± 0.02	0.99 ± 0.02
70	8.30 ± 0.10	2.25 ± 0.08	0.48 ± 0.01	0.03	530.70 ± 6.27	860.43 ± 14.89	2210.67 ± 42.03	6466.67 ± 717.64	2.05 ± 0.04	1.01 ± 0.02
100	8.36 ± 0.16	2.31 ± 0.16	0.48 ± 0.02	0.03	551.03 ± 25.44	810.40 ± 33.81	2146.00 ± 32.35	7206.67 ± 1032.83	2.14 ± 0.04	1.01 ± 0.03
200	8.43 ± 0.10	2.37 ± 0.14	0.48 ± 0.02	0.03	628.17 ± 21.87	821.03 ± 36.50	2136.33 ± 39.87	6623.33 ± 869.51	2.30 ± 0.04	1.00 ± 0.01
300	8.46 ± 0.07	2.36 ± 0.03	0.49 ± 0.01	0.03	668.57 ± 12.64	820.03 ± 15.79	2007.00 ± 58.53	7593.33 ± 1023.59	2.45 ± 0.06	1.02 ± 0.03
400	8.47 ± 0.02	2.44 ± 0.05	0.49 ± 0.01	0.03	662.73 ± 10.47	781.37 ± 11.96	1934.33 ± 13.33	8663.33 ± 295.77	2.50 ± 0.03	1.00 ± 0.04
500	8.46 ± 0.04	2.44 ± 0.07	0.48 ± 0.02	0.03	673.50 ± 18.40	785.85 ± 47.35	1915.50 ± 50.50	8250.00 ± 1690.00	2.53 ± 0.02	0.99 ± 0

Table 3.12. Parameters from fluorescence lifetime measurements of Fl-GluBP-T91V as a function of aspartate**.** The values were calculated by fitting the measurements in Figure 3.15. The experiments were held at 27 °C, pH 7.5 in HEPES 7.5 buffer.

Aspartate (mM)	τ_1 (ns)	τ_2 (ns)	τ_3 (ns)	τ_4 (ns)	A_1 (cnts)	A_2 (cnts)	A_3 (cnts)	A_4 (cnts)	τ (ns)	R^2
0	7.22 ± 0.17	2.03 ± 0.11	0.46 ± 0.03	0.03	237.38 ± 12.35	864.03 ± 52.22	2807.33 ± 168.48	5760.00 ± 435.58	1.22 ± 0.06	0.97 ± 0.02
0.005	7.16 ± 0.12	1.99 ± 0.07	0.44 ± 0.03	0.03	256.27 ± 10.12	877.10 ± 22.91	2803.67 ± 132.60	6033.33 ± 360.43	1.23 ± 0.06	0.97 ± 0.01
0.05	7.28 ± 0.10	2.08 ± 0.06	0.47 ± 0.02	0.03	266.38 ± 11.70	873.63 ± 28.27	2616.33 ± 50.84	7660.00 ± 661.44	1.33 ± 0.02	0.95 ± 0.01
0.5	7.25 ± 0.08	2.06 ± 0.05	0.47 ± 0.01	0.03	267.80 ± 6.89	864.90 ± 17.44	2535.33 ± 22.24	7880.00 ± 1037.99	1.34 ± 0.02	0.96 ± 0.01
5	7.24 ± 0.05	2.06 ± 0.05	0.47 ± 0.01	0.03	279.99 ± 3.82	864.57 ± 17.77	2532.33 ± 22.67	7773.33 ± 1308.41	1.36 ± 0.02	0.96 ± 0.01
10	7.26 ± 0.06	2.05 ± 0.03	0.46 ± 0.02	0.03	290.81 ± 9.27	881.63 ± 24.84	2556.67 ± 93.68	7726.67 ± 380.45	1.36 ± 0.03	0.96 ± 0.01
30	7.30 ± 0.06	2.05 ± 0.03	0.46 ± 0.01	0.03	304.31 ± 9.57	842.63 ± 28.62	2421.67 ± 36.15	9086.67 ± 767.47	1.42 ± 0.03	0.96 ± 0.01
50	7.34 ± 0.05	2.04 ± 0.03	0.45 ± 0.02	0.03	343.08 ± 5.80	908.30 ± 11.66	2549.00 ± 94.54	7066.67 ± 1436.55	1.47 ± 0.04	0.97 ± 0.01
70	7.39 ± 0.03	2.07 ± 0.04	0.47 ± 0.03	0.03	356.75 ± 5.15	894.80 ± 36.23	2415.00 ± 130.22	7510.00 ± 508.56	1.54 ± 0.05	0.97 ± 0
100	7.47 ± 0.04	2.10 ± 0.06	0.46 ± 0.03	0.03	363.89 ± 3.41	878.10 ± 31.13	2450.33 ± 109.45	7703.33 ± 667.19	1.55 ± 0.05	0.96 ± 0.01
200	7.56 ± 0.10	2.15 ± 0.07	0.48 ± 0.03	0.03	386.27 ± 12.48	841.07 ± 14.47	2303.00 ± 60.77	9520.00 ± 1859.63	1.65 ± 0.07	0.96 ± 0
300	7.56 ± 0.13	2.16 ± 0.12	0.48 ± 0.03	0.03	441.07 ± 16.91	881.77 ± 45.73	2285.33 ± 32.34	7463.33 ± 495.39	1.76 ± 0.05	0.97 ± 0
400	7.60 ± 0.10	2.17 ± 0.10	0.49 ± 0.04	0.03	451.70 ± 9.95	865.27 ± 48.64	2279.00 ± 140.44	7580.00 ± 425.48	1.79 ± 0.09	0.97 ± 0.01
500	7.67 ± 0.09	2.17 ± 0.09	0.48 ± 0.03	0.03	460.77 ± 6.82	877.73 ± 28.53	2231.00 ± 75.27	8460.00 ± 631.06	1.83 ± 0.06	0.99 ± 0.01

Chapter 4. Discussion

Glutamate is the predominant mediator of excitatory neurotransmission in the CNS and plays important roles in normal and pathologically altered physiology. Nevertheless, there exist only a limited selection of experimental approaches to quantify glutamate concentrations inside and outside living cells [112, 182]. In the past, genetically encoded, as well as chemically labeled, glutamate fluorescent biosensors have been developed to study glutamate dynamics in diverse systems by real-time monitoring of synaptic and cellular glutamate concentration changes (chapter 1.6). Although these glutamate biosensors were a breakthrough toward investigating neurotransmission in living organisms, their high affinity to glutamate brings limitations in glutamate measurements inside synaptic vesicles: the main storage of the neurotransmitter.

The aim of this work was to engineer a fluorescence glutamate biosensor, capable to detect high mM range of glutamate concentrations inside synaptic vesicles [29]. For this purpose, I have combined molecular dynamics simulations and fluorescence measurements to modify the chemically labeled fluorescent glutamate sensor Fl-GluBP by inserting point mutations and to characterize the biophysical properties of the produced low-affinity variants.

4.1 Novel variants, predicted by MD simulations, cover a broad mM range of affinities to glutamate

Firstly, the atomic MD simulations in a combination with the fast-switching alchemical transformation method was conducted. Using these approaches, I carried out *in silico* mutagenesis and predicted mutations which potentially decrease the affinity of the sensor protein (*ybeJ*) to glutamate. Molecular simulations were based on the recently determined crystal structure of a periplasmic L-aspartate/L-glutamate binding protein (DEBP or *ybeJ*) complexed with an L-glutamate molecule (bound state) [122]. For apo (ligand-free) state the glutamate molecule was manually deleted out from the structure.

Residues in the vicinity of the glutamate molecule (≤ 2 Å), which are supposed to contribute to the rearrangement associated with the glutamate binding, were targeted for the alchemical site-directed mutagenesis to decrease the *ybeJ* affinity to glutamate. Upon the glutamate binding the protein structure adopt closed conformation. Therefore, it was crucial to understand which residues from the glutamate binding pocket undergo a rearrangement that is

directly connected with the closure movement, as their mutation could lead to an interaction disruption in the system and unwanted dramatic changes in affinity. In order to pinpoint possible contributors to the protein closure, I monitored the movement of residues by measuring the inter-residue distances between protein domains (Figure 3.1) in both apo and bound states. Pairs of residues from the glutamate binding pocket, which had a probability to be close (inter-residue distance is ≤ 3 Å) in the bound state, were therefore excluded from the list of targeted residues for future mutagenesis (Figure 3.2).

The computed alchemical glutamate binding free energies (ΔΔG) (Figure 3.4, Table 3.1) revealed the most pronounced changes for the A184W mutation, with a ΔΔG value over 100 kJ/mol. The next promising binding free energy increase was caused by the mutant T91V with a ΔΔG of ~ 50 kJ/mol. Consequently, these two mutations were chosen for experimental testing. The T92A and T92V mutations resulted in a small increase in ΔΔG, within 7-10 kJ/mol, but were selected as well, to further correlate simulation data and experiments. Moreover, the last two mutants were used in the previous generations of glutamate fluorescent biosensors, such as FLIPE-1m [115], iGluSnFR T92A [116] and $iGlu_l$ [114], showing significant decrease in affinity to glutamate.

In order to test the predictions of these simulations experimentally, I expressed GluBP and mutants in *E. coli* and purified them by metal affinity and size-exclusion chromatography (chapter 2.2.1.2). GluBP variants were labeled with environmentally sensitive IANBD ester fluorophore at the engineered Cys136 residue (Fl-GluBP) (chapter 2.2.1.3). Fluorescently labeled derivatives were then tested by steady-state fluorescence measurements (chapter 2.2.2.1) to determine their affinity to glutamate. Glutamate titration experiments (Figure 3.8, B) provided an apparent K_d of 15.2 ± 2.1 μM for Fl-GluBP(-WT), similar to the previously reported value (9.7 ± 0.3 μM) by Coates et al. [114]. The novel Fl-GluBP affinity variants predicted by MD simulations, Fl-GluBP-A184W, Fl-GluBP-T91V, Fl-GluBP-T92A and Fl-GluBP-T92V cover a broad range of K_ds (5.6 ± 0.5 mM, 48.9 ± 2.0 mM, 24.4 ± 2.2 mM and 119.4 ± 17.7 mM, respectively), demonstrating significant decrease in glutamate affinity from ~10 μM to 100 mM, compared to the Fl-GluBP-WT (Table 3.2).

In experiments, theoretically predicted high change in the binding free energy of the A184W mutation, was confirmed by increase of the apparent K_d about 400 times. This observation is in agreement with recent results of the FLIPE sensor [115], whose sensory domain is also based on the *ybeJ* protein. This exchange A to W at position 207 (analogous to 184 in Fl-GluBP-A184W), termed FLIPE-1m, caused a 1700 times affinity decrease from 600

nM to 1 mM. The T92A substitution was previously tested in the iGluSnFR sensor [116] resulting in a K_d value increase from 33 μM to 12 mM (400 times) and later in $iGlu_l$ [114] with the K_d change from 33 μM to 50 mM (1500 - fold). Our measurements of the Fl-GluBP-T92A variant resulted in a 1500 – fold K_d increase. The T91V and T92V mutations, firstly reported in this work, caused the biggest changes in apparent K_d (~ 3300 and 7000 times, respectively) and therefore were proposed as the best candidates for vesicular glutamate detection measurements and subjected to detailed biophysical characterization.

4.2 Characterization of low-affinity variants Fl-GluBP-T91V and Fl-GluBP-T92V at physiological conditions in synaptic vesicles

Synaptic vesicle acidification represents a critical point during the SV cycle: neurotransmitters are loaded into SVs at a luminal acidification to a pH of ~ 5.5 - 5.8 [183]. The key components that execute the acidification and glutamate filling are V-ATPase and VGLUT, which shuttles glutamate molecules into SVs driven by the proton gradient generated by the V-ATPase (chapter 1.3.4). Moreover, the glutamate uptake mechanism underlying VGLUT is a complex process, associated with a rapid change of ionic conditions in the native synaptic vesicle (chapter 1.3.5), and it is thus necessary to study glutamate affinity of low-affinity variants in SVs physiological conditions.

4.2.1 A temperature increase causes a glutamate affinity decrease in low-affinity variants

Obtained apparent K_d values, summarized in Table 3.3, revealed that the temperature increase caused a ~ 4-fold decrease in glutamate affinity of the Fl-GluBP-T91V variant, while leaving the affinities of Fl-GluBP-WT and Fl-GluBP-T92V unaffected. This finding indicates that the T91V mutation affects the initial balance of entropy and enthalpy that might be evaluated in future thermodynamic studies [184].

On the other hand, considering the inability to reach the saturation point during the experiments for both Fl-GluBP-T91V and Fl-GluBP-T92V variants and the significant difference between their fluorescence dynamic ranges upon glutamate binding (Figure 3.9), one could expect a similar equal response to temperature changes.

Nevertheless, the decrease in affinity to glutamate of Fl-GluBP-T91V and Fl-GluBP-T92V variants at 37 °C do not impair the usefulness of these sensor candidates for glutamate measurements inside synaptic vesicles in living neurons.

4.2.2 Low affinity variants have salt unaffected affinity to glutamate

To understand K^+ and Na^+ dependences of the glutamate binding process, I studied the interaction of *ybeJ* with these ions. For this I generated time-averaged ions density maps [150], derived from MD simulations, within 3 Å from the protein structure (Figure 3.5). The K^+ and Na^+ ions density increments around the protein perfectly overlap and revealed regions of strong interaction between ions and the protein structure. Thus, the residues D127, T139, E150, E209, D228, E240, E272, D275 from the protein in the region of ion clusters localization were subjected for further analysis. The plots of minimum distance to K^+ ions from each residue (Figure 3.6) showed an identical distribution of K^+ ions in both apo and bound conformations. Interestingly, a similar pattern was observed for Na^+ ions. This demonstrates that protein interaction with K^+/Na^+ ions does not change under glutamate binding, indicating that ions must not affect the glutamate binding process.

To experimentally corroborate the MD simulations results, I used the same steady-state fluorescence method as in the previous chapter to estimate the K_d values of variants in buffers with different concentrations of NaCl and KCl (Figure 3.10) at pH 5.8. The estimated K_ds (Table 3.4) for Fl-GluBP-WT were determined to be within 7-9 μM and confirmed the assumption derived from simulations about the salt independent behavior of the WT. The measurements for the low affinity variants Fl-GluBP-T91V and -T92V resulted in similar salt independent behavior in presence of different concentrations of NaCl and KCl (Table 3.4), keeping their respective K_d values around 6 mM and 90 mM, respectively.

Taken together, my results confirm the applicability of low affinity variants Fl-GluBP-T91V and Fl-GluBP-T92V for vesicular glutamate measurements.

4.2.3 The Fl-GluBP-T92V variant is insensitive to changes in pH

I next examined the effect of pH on glutamate affinity for Fl-GluBP-WT and the two low affinity variants Fl-GluBP-T91V and Fl-GluBP-T92V in different glutamate concentrations (Figure 3.11). While Fl-GluBP-WT showed a slight pH dependence for glutamate binding, increasing the apparent K_d from 8.2 μM to 23.3 μM in the pH 5.5 – 8.0 range (Table 3.5), surprisingly, Fl-GluBP-T91V and Fl-GluBP-T92V variants demonstrated two completely

opposite results. Compared with the Fl-GluBP-WT, the T91V mutation increases the pH sensitivity and changes the K_d values from 3.1 to 65.2 mM. In contrast, the T92V mutation significantly decreased not only the protein affinity to glutamate but also the protein response to pH changes, keeping the K_d value around ~ 100 mM in each tested pH (Table 3.5).

These results restrict the applicability of the Fl-GluBP-T91V as a suitable sensor for measuring glutamate concentration inside synaptic vesicles. Thus, the Fl-GluBP-T92V variant, which has the lowest affinity to glutamate, is salt stable and pH insensitive, remains the only suitable candidate sensor for vesicular glutamate detections.

4.3 Kinetic analysis of low affinity Fl-GluBP variants

I studied the kinetics of the interaction of glutamate with Fl-GluBP-WT, Fl-GluBP-T91V and Fl-GluBP-T92V by the stopped-flow glutamate application at 5 °C. For all measured variants glutamate concentration steps resulted in fluorescence amplitude increase (Figure 3.13, left). The time course of fluorescence enhancement was fitted with a single exponential function to extract rate constants. The hyperbolic shape of the association rate plots (Figure 3.13, right) suggested a two-step mechanism [169], in which the glutamate binding is followed by conformational changes ("closure" movement in protein structure observed during MD simulations). This is consistent with the kinetic mechanism for Fl-GluBP-WT suggested in [114], in which rapid glutamate binding is followed by isomerization, based on a polarity change around the IANBD ester fluorophore.

The rates obtained from fitting with the induced-fit function (equation 2.19) are summarized in Table 3.8. Best fit parameters to the hyperbole for the Fl-GluBP-WT gave an apparent K_d of 21.0 ± 4.4 μM, which satisfactorily reproduces results firstly described by Coates et al. [114]. One can infer that despite the similar effects on glutamate binding, the two mutations have different effects on the kinetics of glutamate association. The T91V and T92V mutations affect the forward rate (k_1) component of the conformational change more than the backward (k_2) rate, slowing down the conformational change ("closure") induced by glutamate binding by ~ 2-fold, compared to the Fl-GluBP-WT. These results promote decrease of glutamate affinity of these mutants, giving apparent K_d values of 22.7 ± 3.4 mM for -T91V and 91.3 ± 29.7 mM for -T92V, comparable to those measured by steady-state fluorescence values (chapter 4.1). However, k_1 value of each of the variants remains higher than respective k_2 rate demonstrating the lower rates back to the loosely bound state.

Altogether, the obtained results demonstrate that Fl-GluBP-T91V and Fl-GluBP-T92V

impair initial glutamate binding to Fl-GluBP (-WT) and make the subsequent conformational change slower.

4.4 Fluorescence lifetime measurements

Fluorescence lifetime measurements of fluorescent indicators often provide absolute concentrations. We measured fluorescence intensity decays of Fl-GluBP-WT, Fl-GluBP-T91V and Fl-GluBP-T92V upon ps-pulsed excitation at 440 nm have been measured at different glutamate concentrations (0 mM and saturation) to study changes in microenvironment of the IANBD-ester fluorophore upon the glutamate binding process. The representative emission decays, shown on Figure 3.14, were fitted using a three-exponential decay function (sufficient and necessary) equally for every variant, that agrees with an earlier study of NBD fluorescence kinetics [185]. The fluorescence kinetic parameters, summarized in Table 3.9 (for pH 7.5) and Table 3.10 (for pH 5.8), were then used to calculate the average fluorescence lifetime, in order to obtain a qualitative picture. The fluorescence decay of NBD in most solvents is multiexponential, with average fluorescence lifetimes in the order of 5 to 10 ns [185]. Water is the single exception to that with an average fluorescence lifetime around 1 ns. In general, interactions with protons in the excited state open fast non-radiative decay channels and hence add sub-nanosecond components to NBD's fluorescence decay. This behaviour can be exploited to test the accessibility of amino acid residues in proteins to solvent water [130, 186]. Another source for a shortening of NBD's average fluorescence lifetime is the presence of electron-donating groups (like in tryptophane or tyrosine) [187–189]. An electron transfer onto NBD in the excited state and a subsequent faster non-radiative deactivation is proposed as mechanism. Therefore, NBD may also be used to indicate conformational changes in proteins that lead to decreased or increased interactions with neighbouring tyrosine and tryptophan residues.

At pH 7.5, from zero to maximum glutamate concentration (saturation point), average lifetimes increase by 17 % for Fl-GluBP-WT, 125 % for Fl-GluBP-T91V and 50 % for Fl-GluBP-T92V. The fluorescence increase for all the tested variants was also observed at pH 5.8, resulting in 42 % increase for Fl-GluBP-T92V but with a significantly higher range of change for Fl-GluBP-WT (44 %) and Fl-GluBP-T91V (240 %) than at pH 7.5. This observation demonstrates a pH dependence of the Fl-GluBP-WT and -T91V in agreement with our previous results obtained in steady-state experiments. It must be noted that the NBD group is very weakly fluorescent in water, that could be used for sensing accessibility of protons, and its fluorescence lifetime exhibits sensitivity to environmental polarity [127]. Therefore, our results suggest that

the glutamate binding apparently changes the NBD environment to more non-polar and/or reduces the accessibility of protons (meaning water) resulting in the observed lifetime prolongation. A decreased interaction with nearby tryptophans or tyrosines may also contribute to the observed fluorescence lifetime increase. The conformational changes in the Fl-GluBPs might affect several of the three proposed processes. Since the T91V mutation exhibits larger fluorescence changes that the other sensors, it suggests that certain processes are more pronounced in this mutant.

Steady-state experiments showed that Fl-GluBP-T92V has the lowest affinity among the previously reported glutamate sensors (~ 120 mM) [109, 114–116], pH insensitivity and salt stability. These properties make this sensor best suited for glutamate detection inside the synaptic vesicle. However, the small fluorescence dynamic range of the Fl-GluBP-T92V between 0- and 500 mM glutamate concentration (Figure 3.14, C) limits its applicability for precise absolute vesicular glutamate concentration measurements. However, a noticeable change in fluorescence of IANBD ester fluorophore provoked by vesicular glutamate concentration (over 100 mM) would allow to follow the time dependence of glutamate accumulation inside synaptic vesicle. Such tool would be helpful for vesicular refilling dynamic and cellular glutamate homeostasis studies for example using the calyx of Held preparation [190, 191]. The use of solvatochromic (or environmentally sensitive) fluorophores to study biomolecular systems could provide a unique information about the protein interaction and dynamics but is still limited by the challenges encountered when trying to deliver the labeled protein into cells [192]. In this context, the best way to overcome this limitation might be to fuse the biosensor to a fluorescent protein, for example, enhanced green fluorescence protein (EGFP), which was widely used during fluorescent biosensors engineering [112, 193, 194]. In our case, we could use the genetically encoded glutamate sensor iGluSnFR [112, 114], whose sensory domain is also based on the GluBP protein whose two separated fragments are fused at each terminus of circularly permuted eGFP. It is important to point out, that in this case, the insertion of the same point mutation as for Fl-GluBP-T92V will not guarantee that a new sensor will maintain the same glutamate affinity, pH and salt stability, ligand selectivity and the fluorescence dynamic range. Therefore, all these parameters should be tested in a genetically encoded prototype of the Fl-GluBP-T92V sensor.

Fluorescence lifetime experiments revealed that Fl-GluBP-T91V has a wide fluorescence dynamic range. This property together with its salt stability (figure 3.12, C; table

3.7) and low affinity to glutamate at pH 7.5 (K_d of 47 mM) make this variant a candidate sensor for the direct quantification of absolute glutamate levels in the neuronal and glial cytoplasm.

4.4.1 Fl-GluBP-T91V characterization at neuronal cytoplasm physiological conditions

Glutamate and aspartate are both present in large amount in the neuronal cytoplasm [180, 195]. Therefore, in order to test if Fl-GluBP-T91V could be applied for cytoplasmic glutamate detection, it was necessary to know the ligand selectivity of this variant. For this, I monitored fluorescence changes under aspartate and glutamate binding at physiological neuronal pH ~ 7.5 [180, 195, 196]. Both ligands cause a fluorescence increase (Figure 3.15). A more detailed analysis demonstrated that glutamate provokes a bigger change in fluorescence lifetime, that is nearly twice higher than that of aspartate (Table 3.11 and 3.12). Additionally, the fit of ligand titration curves resulted in a K_d of 99.7 ± 8.6 mM for aspartate and 44.7 ± 1.2 mM for glutamate, demonstrating once again the selective behavior for glutamate over aspartate of the Fl-GluBP-T91V variant. However, in an environment where both ligands are present, precise glutamate concentration measurements would be limited by the aspartate contribution. In this case Fl-GluBP-T91V could yield a fluorescence lifetime increase induced by glutamate and aspartate binding at the same time.

Since the K_d is significantly higher than glutamate concentration inside neuronal cytoplasm (~ 10 - 15 mM [31]), we studied fluorescence lifetimes in the cytoplasmic glutamate concentration range. The analysis of averaged lifetime values at glutamate concentrations from 0 to 10 - 30 mM revealed an increase in fluorescence up to ~ 20 - 40 % (Figure 3.15, D and E), demonstrating that Fl-GluBP-T91V sensor can report on smaller glutamate concentrations but with a contribution of aspartate (Figure 3.15, F). Altogether, fluorescent dynamic range of the Fl-GluBP-T91V together with its affinity to glutamate and salt stability allowed us to propose this sensor as a candidate for the direct quantification of absolute glutamate levels in neuronal cytoplasm. However, to make it feasible, we must drastically reduce aspartate binding, which could be accomplished by further mutations in the future. The measurements inside the neuronal cytoplasm could be investigated using the protein microinjection method [197].

The Fl-GluBP-T92A variant with its apparent K_d of 24 mM at pH 7.5 (chapter 3.2.2) might be more suitable for cytoplasmic glutamate measurements. However, further studies to establish the salt dependency of the Fl-GluBP-T92A glutamate affinity and increase the fluorescence dynamic range upon glutamate binding are required.

Conclusions

In this thesis, I engineered and characterized a glutamate fluorescent biosensor: Fl-GluBP-T92V (based on the Fl-GluBP [114]), capable of registering glutamate inside synaptic vesicles.

I used atomistic MD simulations of the *ybeJ* protein [122] together with the fast-switching alchemical transformation method to study glutamate binding to sensory domain and to predict mutants which decrease the protein affinity to glutamate (T91V and T92V). I investigated the *ybeJ* interaction with Na^+ and K^+ ions and established that the glutamate binding process is salt independent.

The computational predictions were confirmed by steady state fluorescence spectroscopy. I could demonstrate that fluorescently labeled by IANBD ester mutant T92V (Fl-GluBP-T92V) has the lowest affinity to glutamate (K_d of ~ 120 mM), is pH insensitive and salt independent. These features make Fl-GluBP-T92V well suited for intravesicular glutamate concentrations measurements. However, time-resolved fluorescence spectroscopy together with fluorescence lifetime measurements revealed only a small fluorescence dynamic range for this mutant that limits absolute glutamate concentration measurements inside SVs.

The Fl-GluBP-T91V variant has a wide fluorescence dynamic range, glutamate selectivity over aspartate and salt stability, but its affinity to glutamate changes with pH. Nevertheless, its K_d at pH 7.5 (~ 49 mM) supposes the applicability of Fl-GluBP-T91V for absolute glutamate measurements inside the neuronal cytoplasm. However, currently the use of this sensor is limited by its low selectivity between aspartate and glutamate that makes Fl-GluBP-T91V unable to report specifically on the glutamate concentration in the cytoplasm of neuronal and glial cells.

With these results, I proposed Fl-GluBP-T91V as a promising candidate sensor for the direct quantification of absolute glutamate levels in neuronal cytoplasm and Fl-GluBP-T92V for quantifying the time course of glutamate accumulation inside synaptic vesicles.

Bibliography

[1] Ezza HSA and Khadrawyb YA, “Glutamate Excitotoxicity and Neurodegeneration,” *Journal of Molecular and Genetic Medicine*, vol. 08, no. 04, 2014, doi: 10.4172/1747-0862.1000141.

[2] J. Shen, “Glutamate,” in *Magnetic Resonance Spectroscopy*, Elsevier, 2014, pp. 111–121. doi: 10.1016/B978-0-12-401688-0.00009-4.

[3] H. A. Krebs, “Metabolism of amino-acids: The synthesis of glutamine from glutamic acid and ammonia, and the enzymic hydrolysis of glutamine in animal tissues.,” *Biochem J*, vol. 29, no. 8, pp. 1951–69, Aug. 1935, doi: 10.1042/bj0291951.

[4] F. Fonnum, “Glutamate: a neurotransmitter in mammalian brain.,” *J Neurochem*, vol. 42, no. 1, pp. 1–11, Jan. 1984, doi: 10.1111/j.1471-4159.1984.tb09689.x.

[5] M. J. Niciu, B. Kelmendi, and G. Sanacora, “Overview of glutamatergic neurotransmission in the nervous system,” *Pharmacology Biochemistry and Behavior*, vol. 100, no. 4. pp. 656–664, Feb. 2012. doi: 10.1016/j.pbb.2011.08.008.

[6] O. A. C. Petroff, “GABA and glutamate in the human brain,” *Neuroscientist*, vol. 8, no. 6. pp. 562–573, Dec. 2002. doi: 10.1177/1073858402238515.

[7] M. Erecińska and I. A. Silver, “Metabolism and role of glutamate in mammalian brain.,” *Prog Neurobiol*, vol. 35, no. 4, pp. 245–96, 1990, doi: 10.1016/0301-0082(90)90013-7.

[8] H. Tapiero, G. Mathé, P. Couvreur, and K. D. Tew, “II. Glutamine and glutamate.,” *Biomed Pharmacother*, vol. 56, no. 9, pp. 446–57, Nov. 2002, doi: 10.1016/s0753-3322(02)00285-8.

[9] Jü, “L-Glutamate_Structural_Formulae,” Feb. 07, 2010. https://commons.wikimedia.org/wiki/File:L-Glutamate_Structural_Formulae.png (accessed Jan. 03, 2023).

[10] Y. Hu, C.-P. Fan, G. Fu, D. Zhu, Q. Jin, and D.-C. Wang, “2VHA,” Jul. 08, 2008. https://www.rcsb.org/structure/2vha (accessed Jan. 03, 2023).

[11] N. C. Danbolt, “Glutamate uptake.,” *Prog Neurobiol*, vol. 65, no. 1, pp. 1–105, Sep. 2001, doi: 10.1016/s0301-0082(00)00067-8.

[12] W. A. Fairman and S. G. Amara, “Functional diversity of excitatory amino acid transporters: ion channel and transport modes.,” *Am J Physiol*, vol. 277, no. 4, pp. F481-6, Oct. 1999, doi: 10.1152/ajprenal.1999.277.4.F481.

[13] J. Shen *et al.*, "Determination of the rate of the glutamate/glutamine cycle in the human brain by in vivo 13C NMR.," *Proc Natl Acad Sci U S A*, vol. 96, no. 14, pp. 8235–40, Jul. 1999, doi: 10.1073/pnas.96.14.8235.

[14] D. E. Featherstone, "Intercellular glutamate signaling in the nervous system and beyond.," *ACS Chem Neurosci*, vol. 1, no. 1, pp. 4–12, Jan. 2010, doi: 10.1021/cn900006n.

[15] V. M. Ho, J.-A. Lee, and K. C. Martin, "The cell biology of synaptic plasticity.," *Science*, vol. 334, no. 6056, pp. 623–8, Nov. 2011, doi: 10.1126/science.1209236.

[16] Z. P. Pang and T. C. Südhof, "Cell biology of Ca2+-triggered exocytosis," *Curr Opin Cell Biol*, vol. 22, no. 4, pp. 496–505, Aug. 2010, doi: 10.1016/j.ceb.2010.05.001.

[17] T. C. Südhof and J. E. Rothman, "Membrane fusion: grappling with SNARE and SM proteins.," *Science*, vol. 323, no. 5913, pp. 474–7, Jan. 2009, doi: 10.1126/science.1161748.

[18] "The principles of nerve cell communication.," *Alcohol Health Res World*, vol. 21, no. 2, pp. 107–8, 1997, [Online]. Available: http://www.ncbi.nlm.nih.gov/pubmed/15704344

[19] S. Takamori *et al.*, "Molecular anatomy of a trafficking organelle.," *Cell*, vol. 127, no. 4, pp. 831–46, Nov. 2006, doi: 10.1016/j.cell.2006.10.030.

[20] H. Omote, T. Miyaji, N. Juge, and Y. Moriyama, "Vesicular neurotransmitter transporter: bioenergetics and regulation of glutamate transport.," *Biochemistry*, vol. 50, no. 25, pp. 5558–65, Jun. 2011, doi: 10.1021/bi200567k.

[21] R. J. Vandenberg and R. M. Ryan, "Mechanisms of glutamate transport.," *Physiol Rev*, vol. 93, no. 4, pp. 1621–57, Oct. 2013, doi: 10.1152/physrev.00007.2013.

[22] Y. A. Chen and R. H. Scheller, "SNARE-mediated membrane fusion.," *Nat Rev Mol Cell Biol*, vol. 2, no. 2, pp. 98–106, Feb. 2001, doi: 10.1038/35052017.

[23] T. C. Südhof, "THE SYNAPTIC VESICLE CYCLE," *Annu Rev Neurosci*, vol. 27, no. 1, pp. 509–547, Jul. 2004, doi: 10.1146/annurev.neuro.26.041002.131412.

[24] T. C. Südhof and J. Rizo, "Synaptic vesicle exocytosis.," *Cold Spring Harb Perspect Biol*, vol. 3, no. 12, Dec. 2011, doi: 10.1101/cshperspect.a005637.

[25] R. Jahn and T. C. Südhof, "Synaptic vesicles and exocytosis.," *Annu Rev Neurosci*, vol. 17, pp. 219–46, 1994, doi: 10.1146/annurev.ne.17.030194.001251.

[26] Y. Egashira, M. Takase, and S. Takamori, "Monitoring of Vacuolar-Type H+ ATPase-Mediated Proton Influx into Synaptic Vesicles," *Journal of Neuroscience*, vol. 35, no. 8, pp. 3701–3710, Feb. 2015, doi: 10.1523/JNEUROSCI.4160-14.2015.

[27] M. Martineau, R. E. Guzman, C. Fahlke, and J. Klingauf, “VGLUT1 functions as a glutamate/proton exchanger with chloride channel activity in hippocampal glutamatergic synapses,” *Nat Commun*, vol. 8, no. 1, p. 2279, Dec. 2017, doi: 10.1038/s41467-017-02367-6.

[28] T. Hori and T. Takahashi, “Kinetics of synaptic vesicle refilling with neurotransmitter glutamate.,” *Neuron*, vol. 76, no. 3, pp. 511–7, Nov. 2012, doi: 10.1016/j.neuron.2012.08.013.

[29] S. el Mestikawy, A. Wallén-Mackenzie, G. M. Fortin, L. Descarries, and L.-E. Trudeau, “From glutamate co-release to vesicular synergy: vesicular glutamate transporters.,” *Nat Rev Neurosci*, vol. 12, no. 4, pp. 204–16, Apr. 2011, doi: 10.1038/nrn2969.

[30] P. M. Burger *et al.*, “Synaptic vesicles immunoisolated from rat cerebral cortex contain high levels of glutamate,” *Neuron*, vol. 3, no. 6, pp. 715–720, Dec. 1989, doi: 10.1016/0896-6273(89)90240-7.

[31] S. Mangia, F. Giove, and M. Dinuzzo, “Metabolic pathways and activity-dependent modulation of glutamate concentration in the human brain.,” *Neurochem Res*, vol. 37, no. 11, pp. 2554–61, Nov. 2012, doi: 10.1007/s11064-012-0848-4.

[32] P. M. Burger, J. Hell, E. Mehl, C. Krasel, F. Lottspeich, and R. Jahn, “GABA and glycine in synaptic vesicles: storage and transport characteristics,” *Neuron*, vol. 7, no. 2, pp. 287–293, Aug. 1991, doi: 10.1016/0896-6273(91)90267-4.

[33] R. J. Bridges, N. R. Natale, and S. A. Patel, “System x c- cystine/glutamate antiporter: An update on molecular pharmacology and roles within the CNS,” *British Journal of Pharmacology*, vol. 165, no. 1. pp. 20–34, Jan. 2012. doi: 10.1111/j.1476-5381.2011.01480.x.

[34] H. Omote, T. Miyaji, M. Hiasa, N. Juge, and Y. Moriyama, “Structure, Function, and Drug Interactions of Neurotransmitter Transporters in the Postgenomic Era.,” *Annu Rev Pharmacol Toxicol*, vol. 56, pp. 385–402, 2016, doi: 10.1146/annurev-pharmtox-010814-124816.

[35] H. Omote and Y. Moriyama, “Vesicular Neurotransmitter Transporters: An Approach for Studying Transporters With Purified Proteins,” *Physiology*, vol. 28, no. 1, pp. 39–50, Jan. 2013, doi: 10.1152/physiol.00033.2012.

[36] B. Ni, P. R. Rosteck, N. S. Nadi, and S. M. Paul, “Cloning and expression of a cDNA encoding a brain-specific Na(+)-dependent inorganic phosphate cotransporter.,” *Proc*

Natl Acad Sci U S A, vol. 91, no. 12, pp. 5607–11, Jun. 1994, doi: 10.1073/pnas.91.12.5607.

[37] S. Naito and T. Ueda, "Characterization of glutamate uptake into synaptic vesicles.," *J Neurochem*, vol. 44, no. 1, pp. 99–109, Jan. 1985, doi: 10.1111/j.1471-4159.1985.tb07118.x.

[38] Y. Aihara *et al.*, "Molecular cloning of a novel brain-type Na(+)-dependent inorganic phosphate cotransporter.," *J Neurochem*, vol. 74, no. 6, pp. 2622–5, Jun. 2000, doi: 10.1046/j.1471-4159.2000.0742622.x.

[39] R. T. Fremeau *et al.*, "The identification of vesicular glutamate transporter 3 suggests novel modes of signaling by glutamate.," *Proc Natl Acad Sci U S A*, vol. 99, no. 22, pp. 14488–93, Oct. 2002, doi: 10.1073/pnas.222546799.

[40] B. S. Meldrum, "Glutamate as a neurotransmitter in the brain: review of physiology and pathology.," *J Nutr*, vol. 130, no. 4S Suppl, pp. 1007S–15S, Apr. 2000, doi: 10.1093/jn/130.4.1007S.

[41] P. Bezzi *et al.*, "Astrocytes contain a vesicular compartment that is competent for regulated exocytosis of glutamate.," *Nat Neurosci*, vol. 7, no. 6, pp. 613–20, Jun. 2004, doi: 10.1038/nn1246.

[42] R. T. Fremeau, S. Voglmaier, R. P. Seal, and R. H. Edwards, "VGLUTs define subsets of excitatory neurons and suggest novel roles for glutamate.," *Trends Neurosci*, vol. 27, no. 2, pp. 98–103, Feb. 2004, doi: 10.1016/j.tins.2003.11.005.

[43] H. Wolosker, D. O. de Souza, and L. de Meis, "Regulation of Glutamate Transport into Synaptic Vesicles by Chloride and Proton Gradient," *Journal of Biological Chemistry*, vol. 271, no. 20, pp. 11726–11731, May 1996, doi: 10.1074/jbc.271.20.11726.

[44] S. Schenck, S. M. Wojcik, N. Brose, and S. Takamori, "A chloride conductance in VGLUT1 underlies maximal glutamate loading into synaptic vesicles," *Nat Neurosci*, vol. 12, no. 2, pp. 156–162, Feb. 2009, doi: 10.1038/nn.2248.

[45] P. R. Maycox, T. Deckwerth, J. W. Hell, and R. Jahn, "Glutamate uptake by brain synaptic vesicles. Energy dependence of transport and functional reconstitution in proteoliposomes.," *J Biol Chem*, vol. 263, no. 30, pp. 15423–8, Oct. 1988, [Online]. Available: http://www.ncbi.nlm.nih.gov/pubmed/2902091

[46] R. H. Edwards, "The neurotransmitter cycle and quantal size.," *Neuron*, vol. 55, no. 6, pp. 835–58, Sep. 2007, doi: 10.1016/j.neuron.2007.09.001.

[47] F. A. Chaudhry, J.-L. Boulland, M. Jenstad, M. K. L. Bredahl, and R. H. Edwards, "Pharmacology of Neurotransmitter Transport into Secretory Vesicles," in *Handbook of experimental pharmacology*, no. 184, 2008, pp. 77–106. doi: 10.1007/978-3-540-74805-2_4.

[48] N. Pietrancosta, M. Djibo, S. Daumas, S. el Mestikawy, and J. D. Erickson, "Molecular, Structural, Functional, and Pharmacological Sites for Vesicular Glutamate Transporter Regulation.," *Mol Neurobiol*, vol. 57, no. 7, pp. 3118–3142, Jul. 2020, doi: 10.1007/s12035-020-01912-7.

[49] S. M. Stobrawa *et al.*, "Disruption of ClC-3, a Chloride Channel Expressed on Synaptic Vesicles, Leads to a Loss of the Hippocampus," *Neuron*, vol. 29, no. 1, pp. 185–196, Jan. 2001, doi: 10.1016/S0896-6273(01)00189-1.

[50] J. Preobraschenski, J.-F. Zander, T. Suzuki, G. Ahnert-Hilger, and R. Jahn, "Vesicular glutamate transporters use flexible anion and cation binding sites for efficient accumulation of neurotransmitter.," *Neuron*, vol. 84, no. 6, pp. 1287–301, Dec. 2014, doi: 10.1016/j.neuron.2014.11.008.

[51] J. Preobraschenski *et al.*, "Dual and Direction-Selective Mechanisms of Phosphate Transport by the Vesicular Glutamate Transporter.," *Cell Rep*, vol. 23, no. 2, pp. 535–545, Apr. 2018, doi: 10.1016/j.celrep.2018.03.055.

[52] N. Juge, Y. Yoshida, S. Yatsushiro, H. Omote, and Y. Moriyama, "Vesicular glutamate transporter contains two independent transport machineries.," *J Biol Chem*, vol. 281, no. 51, pp. 39499–506, Dec. 2006, doi: 10.1074/jbc.M607670200.

[53] N. Juge *et al.*, "Metabolic Control of Vesicular Glutamate Transport and Release," *Neuron*, vol. 68, no. 1, pp. 99–112, Oct. 2010, doi: 10.1016/j.neuron.2010.09.002.

[54] G. Y. Goh *et al.*, "Presynaptic regulation of quantal size: K+/H+ exchange stimulates vesicular glutamate transport.," *Nat Neurosci*, vol. 14, no. 10, pp. 1285–92, Aug. 2011, doi: 10.1038/nn.2898.

[55] A. Lehmann, H. Isacsson, and A. Hamberger, "Effects of in vivo administration of kainic acid on the extracellular amino acid pool in the rabbit hippocampus.," *J Neurochem*, vol. 40, no. 5, pp. 1314–20, May 1983, doi: 10.1111/j.1471-4159.1983.tb13572.x.

[56] F. A. Chaudhry, K. P. Lehre, M. van Lookeren Campagne, O. P. Ottersen, N. C. Danbolt, and J. Storm-Mathisen, "Glutamate transporters in glial plasma membranes: highly differentiated localizations revealed by quantitative ultrastructural

immunocytochemistry.," *Neuron*, vol. 15, no. 3, pp. 711–20, Sep. 1995, doi: 10.1016/0896-6273(95)90158-2.

[57] W. A. Fairman, R. J. Vandenberg, J. L. Arriza, M. P. Kavanaugh, and S. G. Amara, "An excitatory amino-acid transporter with properties of a ligand-gated chloride channel.," *Nature*, vol. 375, no. 6532, pp. 599–603, Jun. 1995, doi: 10.1038/375599a0.

[58] G. Pines *et al.*, "Cloning and expression of a rat brain L-glutamate transporter.," *Nature*, vol. 360, no. 6403, pp. 464–7, Dec. 1992, doi: 10.1038/360464a0.

[59] T. Storck, S. Schulte, K. Hofmann, and W. Stoffel, "Structure, expression, and functional analysis of a Na(+)-dependent glutamate/aspartate transporter from rat brain.," *Proc Natl Acad Sci U S A*, vol. 89, no. 22, pp. 10955–9, Nov. 1992, doi: 10.1073/pnas.89.22.10955.

[60] J. I. Wadiche, S. G. Amara, and M. P. Kavanaugh, "Ion fluxes associated with excitatory amino acid transport," *Neuron*, vol. 15, no. 3, pp. 721–728, Sep. 1995, doi: 10.1016/0896-6273(95)90159-0.

[61] A. Martinez-Hernandez, K. P. Bell, and M. D. Norenberg, "Glutamine synthetase: glial localization in brain.," *Science*, vol. 195, no. 4284, pp. 1356–8, Mar. 1977, doi: 10.1126/science.14400.

[62] K. P. Lehre and N. C. Danbolt, "The number of glutamate transporter subtype molecules at glutamatergic synapses: chemical and stereological quantification in young adult rat brain.," *J Neurosci*, vol. 18, no. 21, pp. 8751–7, Nov. 1998, doi: 10.1523/JNEUROSCI.18-21-08751.1998.

[63] S. Holmseth *et al.*, "The density of EAAC1 (EAAT3) glutamate transporters expressed by neurons in the mammalian CNS.," *J Neurosci*, vol. 32, no. 17, pp. 6000–13, Apr. 2012, doi: 10.1523/JNEUROSCI.5347-11.2012.

[64] Y. Dehnes, F. A. Chaudhry, K. Ullensvang, K. P. Lehre, J. Storm-Mathisen, and N. C. Danbolt, "The glutamate transporter EAAT4 in rat cerebellar Purkinje cells: a glutamate-gated chloride channel concentrated near the synapse in parts of the dendritic membrane facing astroglia.," *J Neurosci*, vol. 18, no. 10, pp. 3606–19, May 1998, doi: 10.1523/JNEUROSCI.18-10-03606.1998.

[65] J. L. Arriza, S. Eliasof, M. P. Kavanaugh, and S. G. Amara, "Excitatory amino acid transporter 5, a retinal glutamate transporter coupled to a chloride conductance.," *Proc Natl Acad Sci U S A*, vol. 94, no. 8, pp. 4155–60, Apr. 1997, doi: 10.1073/pnas.94.8.4155.

[66] J. C. Matthews *et al.*, "Activity and protein localization of multiple glutamate transporters in gestation day 14 vs. day 20 rat placenta.," *Am J Physiol*, vol. 274, no. 3, pp. C603-14, Mar. 1998, doi: 10.1152/ajpcell.1998.274.3.C603.

[67] T. Nakayama, H. Kawakami, K. Tanaka, and S. Nakamura, "Expression of three glutamate transporter subtype mRNAs in human brain regions and peripheral tissues.," *Brain Res Mol Brain Res*, vol. 36, no. 1, pp. 189–92, Feb. 1996, doi: 10.1016/0169-328x(95)00297-6.

[68] Y. Zhou and N. C. Danbolt, "Glutamate as a neurotransmitter in the healthy brain," *Journal of Neural Transmission*, vol. 121, no. 8. pp. 799–817, 2014. doi: 10.1007/s00702-014-1180-8.

[69] S. Bannai, "Exchange of cystine and glutamate across plasma membrane of human fibroblasts.," *J Biol Chem*, vol. 261, no. 5, pp. 2256–63, Feb. 1986, [Online]. Available: http://www.ncbi.nlm.nih.gov/pubmed/2868011

[70] D. A. Baker, Z.-X. Xi, H. Shen, C. J. Swanson, and P. W. Kalivas, "The origin and neuronal function of in vivo nonsynaptic glutamate.," *J Neurosci*, vol. 22, no. 20, pp. 9134–41, Oct. 2002, doi: 10.1523/JNEUROSCI.22-20-09134.2002.

[71] D. de Bundel *et al.*, "Loss of System xFormula Does Not Induce Oxidative Stress But Decreases Extracellular Glutamate in Hippocampus and Influences Spatial Working Memory and Limbic Seizure Susceptibility," *Journal of Neuroscience*, vol. 31, no. 15, pp. 5792–5803, Apr. 2011, doi: 10.1523/JNEUROSCI.5465-10.2011.

[72] K. Koch *et al.*, "Overexpression of Cystine/Glutamate Antiporter xCT Correlates with Nutrient Flexibility and ZEB1 Expression in Highly Clonogenic Glioblastoma Stem-like Cells (GSCs).," *Cancers (Basel)*, vol. 13, no. 23, Nov. 2021, doi: 10.3390/cancers13236001.

[73] R. A. Umans *et al.*, "Transcriptional Regulation of Amino Acid Transport in Glioblastoma Multiforme.," *Cancers (Basel)*, vol. 13, no. 24, p. 6169, Dec. 2021, doi: 10.3390/cancers13246169.

[74] S. Takeuchi *et al.*, "Increased xCT Expression Correlates With Tumor Invasion and Outcome in Patients With Glioblastomas," *Neurosurgery*, vol. 72, no. 1, pp. 33–41, Jan. 2013, doi: 10.1227/NEU.0b013e318276b2de.

[75] J. Lewerenz *et al.*, "The cystine/glutamate antiporter system x(c)(-) in health and disease: from molecular mechanisms to novel therapeutic opportunities.," *Antioxid Redox Signal*, vol. 18, no. 5, pp. 522–55, Feb. 2013, doi: 10.1089/ars.2011.4391.

[76] I. Yamaguchi, S. H. Yoshimura, and H. Katoh, “High cell density increases glioblastoma cell viability under glucose deprivation via degradation of the cystine/glutamate transporter xCT (SLC7A11),” *Journal of Biological Chemistry*, vol. 295, no. 20, pp. 6936–6945, May 2020, doi: 10.1074/jbc.RA119.012213.

[77] N. Scheefhals and H. D. MacGillavry, “Functional organization of postsynaptic glutamate receptors.,” *Mol Cell Neurosci*, vol. 91, pp. 82–94, Sep. 2018, doi: 10.1016/j.mcn.2018.05.002.

[78] S. F. Traynelis *et al.*, “Glutamate receptor ion channels: Structure, regulation, and function,” *Pharmacological Reviews*, vol. 62, no. 3. pp. 405–496, Sep. 2010. doi: 10.1124/pr.109.002451.

[79] D. L. Egbenya, E. Aidoo, and G. Kyei, “Glutamate receptors in brain development,” *Child’s Nervous System*, vol. 37, no. 9. Springer Science and Business Media Deutschland GmbH, pp. 2753–2758, Sep. 01, 2021. doi: 10.1007/s00381-021-05266-w.

[80] L. F. Abbott and S. B. Nelson, “Synaptic plasticity: taming the beast.,” *Nat Neurosci*, vol. 3 Suppl, pp. 1178–83, Nov. 2000, doi: 10.1038/81453.

[81] A. Citri and R. C. Malenka, “Synaptic Plasticity: Multiple Forms, Functions, and Mechanisms,” *Neuropsychopharmacology*, vol. 33, no. 1, pp. 18–41, Jan. 2008, doi: 10.1038/sj.npp.1301559.

[82] V. N. Murthy, “Synaptic plasticity: step-wise strengthening.,” *Curr Biol*, vol. 8, no. 18, pp. R650-3, Sep. 1998, doi: 10.1016/s0960-9822(07)00414-9.

[83] C. C. Petersen, R. C. Malenka, R. A. Nicoll, and J. J. Hopfield, “All-or-none potentiation at CA3-CA1 synapses.,” *Proc Natl Acad Sci U S A*, vol. 95, no. 8, pp. 4732–7, Apr. 1998, doi: 10.1073/pnas.95.8.4732.

[84] D. R. Lucas and J. P. Newhouse, “The toxic effect of sodium L-glutamate on the inner layers of the retina.,” *AMA Arch Ophthalmol*, vol. 58, no. 2, pp. 193–201, Aug. 1957, doi: 10.1001/archopht.1957.00940010205006.

[85] J. W. Olney, “Brain lesions, obesity, and other disturbances in mice treated with monosodium glutamate.,” *Science*, vol. 164, no. 3880, pp. 719–21, May 1969, doi: 10.1126/science.164.3880.719.

[86] A. Lau and M. Tymianski, “Glutamate receptors, neurotoxicity and neurodegeneration.,” *Pflugers Arch*, vol. 460, no. 2, pp. 525–42, Jul. 2010, doi: 10.1007/s00424-010-0809-1.

[87] S. Rothman, “Synaptic release of excitatory amino acid neurotransmitter mediates anoxic neuronal death.,” *J Neurosci*, vol. 4, no. 7, pp. 1884–91, Jul. 1984, doi: 10.1523/JNEUROSCI.04-07-01884.1984.

[88] M. Y. Globus, R. Busto, E. Martinez, I. Valdés, and W. D. Dietrich, “Ischemia induces release of glutamate in regions spared from histopathologic damage in the rat.,” *Stroke*, vol. 21, no. 11 Suppl, pp. III43-6, Nov. 1990, [Online]. Available: http://www.ncbi.nlm.nih.gov/pubmed/2237984

[89] M. Arundine and M. Tymianski, “Molecular mechanisms of glutamate-dependent neurodegeneration in ischemia and traumatic brain injury.,” *Cell Mol Life Sci*, vol. 61, no. 6, pp. 657–68, Mar. 2004, doi: 10.1007/s00018-003-3319-x.

[90] O. Hardiman *et al.*, “Amyotrophic lateral sclerosis.,” *Nat Rev Dis Primers*, vol. 3, p. 17071, Oct. 2017, doi: 10.1038/nrdp.2017.71.

[91] P. J. Shaw and P. G. Ince, “Glutamate, excitotoxicity and amyotrophic lateral sclerosis.,” *J Neurol*, vol. 244 Suppl 2, no. S2, pp. S3-14, May 1997, doi: 10.1007/BF03160574.

[92] Z. Zhang *et al.*, “Roles of Glutamate Receptors in Parkinson’s Disease.,” *Int J Mol Sci*, vol. 20, no. 18, Sep. 2019, doi: 10.3390/ijms20184391.

[93] F. Blandini, R. H. Porter, and J. T. Greenamyre, “Glutamate and Parkinson’s disease.,” *Mol Neurobiol*, vol. 12, no. 1, pp. 73–94, Feb. 1996, doi: 10.1007/BF02740748.

[94] W. Dauer and S. Przedborski, “Parkinson’s disease: mechanisms and models.,” *Neuron*, vol. 39, no. 6, pp. 889–909, Sep. 2003, doi: 10.1016/s0896-6273(03)00568-3.

[95] P. R. Sanberg and G. A. Johnston, “Glutamate and Huntington’s disease.,” *Med J Aust*, vol. 2, no. 9, pp. 460–5, Oct. 1981, doi: 10.5694/j.1326-5377.1981.tb112939.x.

[96] F. M. Ribeiro, R. G. W. Pires, and S. S. G. Ferguson, “Huntington’s Disease and Group I Metabotropic Glutamate Receptors,” *Mol Neurobiol*, vol. 43, no. 1, pp. 1–11, Feb. 2011, doi: 10.1007/s12035-010-8153-1.

[97] R. Wang and P. H. Reddy, “Role of Glutamate and NMDA Receptors in Alzheimer’s Disease.,” *J Alzheimers Dis*, vol. 57, no. 4, pp. 1041–1048, 2017, doi: 10.3233/JAD-160763.

[98] M. R. Hynd, H. L. Scott, and P. R. Dodd, “Glutamate-mediated excitotoxicity and neurodegeneration in Alzheimer’s disease.,” *Neurochem Int*, vol. 45, no. 5, pp. 583–95, Oct. 2004, doi: 10.1016/j.neuint.2004.03.007.

[99] J. v Andersen, A. Schousboe, and A. Verkhratsky, “Astrocyte energy and neurotransmitter metabolism in Alzheimer’s disease: Integration of the

glutamate/GABA-glutamine cycle.," *Prog Neurobiol*, vol. 217, p. 102331, Oct. 2022, doi: 10.1016/j.pneurobio.2022.102331.

[100] H. S. Walton and P. R. Dodd, "Glutamate-glutamine cycling in Alzheimer's disease.," *Neurochem Int*, vol. 50, no. 7–8, pp. 1052–66, Jun. 2007, doi: 10.1016/j.neuint.2006.10.007.

[101] M. F. Sørensen *et al.*, "High expression of cystine–glutamate antiporter xCT (SLC7A11) is an independent biomarker for epileptic seizures at diagnosis in glioma," *J Neurooncol*, vol. 138, no. 1, pp. 49–53, May 2018, doi: 10.1007/s11060-018-2785-9.

[102] J. Choi, B. Stradmann-Bellinghausen, E. Yakubov, N. E. Savaskan, and A. Régnier-Vigouroux, "Glioblastoma cells induce differential glutamatergic gene expressions in human tumor-associated microglia/macrophages and monocyte-derived macrophages.," *Cancer Biol Ther*, vol. 16, no. 8, pp. 1205–13, Aug. 2015, doi: 10.1080/15384047.2015.1056406.

[103] B. Kerner, "Glutamate Neurotransmission in Psychotic Disorders and Substance Abuse.," *Open Psychiatr J*, vol. 3, pp. 1–8, Jan. 2009, doi: 10.2174/1874354400903010001.

[104] R. M. Tordera *et al.*, "Enhanced anxiety, depressive-like behaviour and impaired recognition memory in mice with reduced expression of the vesicular glutamate transporter 1 (VGLUT1).," *Eur J Neurosci*, vol. 25, no. 1, pp. 281–90, Jan. 2007, doi: 10.1111/j.1460-9568.2006.05259.x.

[105] A. Oni-Orisan, L. v Kristiansen, V. Haroutunian, J. H. Meador-Woodruff, and R. E. McCullumsmith, "Altered vesicular glutamate transporter expression in the anterior cingulate cortex in schizophrenia.," *Biol Psychiatry*, vol. 63, no. 8, pp. 766–75, Apr. 2008, doi: 10.1016/j.biopsych.2007.10.020.

[106] L. Musazzi *et al.*, "Acute stress increases depolarization-evoked glutamate release in the rat prefrontal/frontal cortex: the dampening action of antidepressants.," *PLoS One*, vol. 5, no. 1, p. e8566, Jan. 2010, doi: 10.1371/journal.pone.0008566.

[107] A. B. Fallgren and R. E. Paulsen, "A microdialysis study in rat brain of dihydrokainate, a glutamate uptake inhibitor.," *Neurochem Res*, vol. 21, no. 1, pp. 19–25, Jan. 1996, doi: 10.1007/BF02527667.

[108] H. Benveniste, J. Drejer, A. Schousboe, and N. H. Diemer, "Elevation of the extracellular concentrations of glutamate and aspartate in rat hippocampus during transient cerebral ischemia monitored by intracerebral microdialysis.," *J Neurochem*, vol. 43, no. 5, pp. 1369–74, Nov. 1984, doi: 10.1111/j.1471-4159.1984.tb05396.x.

[109] C. D. Dürst *et al.*, "High-speed imaging of glutamate release with genetically encoded sensors," *Nat Protoc*, vol. 14, no. 5, pp. 1401–1424, May 2019, doi: 10.1038/s41596-019-0143-9.

[110] K. Takikawa *et al.*, "High-throughput development of a hybrid-type fluorescent glutamate sensor for analysis of synaptic transmission.," *Angew Chem Int Ed Engl*, vol. 53, no. 49, pp. 13439–43, Dec. 2014, doi: 10.1002/anie.201407181.

[111] S. Namiki, H. Sakamoto, S. Iinuma, M. Iino, and K. Hirose, "Optical glutamate sensor for spatiotemporal analysis of synaptic transmission.," *Eur J Neurosci*, vol. 25, no. 8, pp. 2249–59, Apr. 2007, doi: 10.1111/j.1460-9568.2007.05511.x.

[112] J. S. Marvin *et al.*, "An optimized fluorescent probe for visualizing glutamate neurotransmission.," *Nat Methods*, vol. 10, no. 2, pp. 162–70, Feb. 2013, doi: 10.1038/nmeth.2333.

[113] R. Abele, K. Keinanen, and D. R. Madden, "Agonist-induced isomerization in a glutamate receptor ligand-binding domain. A kinetic and mutagenetic analysis.," *J Biol Chem*, vol. 275, no. 28, pp. 21355–63, Jul. 2000, doi: 10.1074/jbc.M909883199.

[114] C. Coates, S. Kerruth, N. Helassa, and K. Török, "Kinetic Mechanisms of Fast Glutamate Sensing by Fluorescent Protein Probes.," *Biophys J*, vol. 118, no. 1, pp. 117–127, Jan. 2020, doi: 10.1016/j.bpj.2019.11.006.

[115] S. Okumoto, L. L. Looger, K. D. Micheva, R. J. Reimer, S. J. Smith, and W. B. Frommer, "Detection of glutamate release from neurons by genetically encoded surface-displayed FRET nanosensors.," *Proc Natl Acad Sci U S A*, vol. 102, no. 24, pp. 8740–5, Jun. 2005, doi: 10.1073/pnas.0503274102.

[116] N. Helassa *et al.*, "Ultrafast glutamate sensors resolve high-frequency release at Schaffer collateral synapses," *Proc Natl Acad Sci U S A*, vol. 115, no. 21, pp. 5594–5599, May 2018, doi: 10.1073/pnas.1720648115.

[117] S. A. Hires, Y. Zhu, and R. Y. Tsien, "Optical measurement of synaptic glutamate spillover and reuptake by linker optimized glutamate-sensitive fluorescent reporters," *Proc Natl Acad Sci U S A*, vol. 105, no. 11, pp. 4411–4416, Mar. 2008, doi: 10.1073/pnas.0712008105.

[118] P. A. Rea, "Plant ATP-binding cassette transporters.," *Annu Rev Plant Biol*, vol. 58, pp. 347–75, 2007, doi: 10.1146/annurev.arplant.57.032905.105406.

[119] A. L. Davidson and J. Chen, "ATP-binding cassette transporters in bacteria.," *Annu Rev Biochem*, vol. 73, pp. 241–68, 2004, doi: 10.1146/annurev.biochem.73.011303.073626.

[120] K. Hollenstein, D. C. Frei, and K. P. Locher, “Structure of an ABC transporter in complex with its binding protein,” *Nature*, vol. 446, no. 7132, pp. 213–216, Mar. 2007, doi: 10.1038/nature05626.

[121] R. C. Willis and C. E. Furlong, “Purification and properties of a periplasmic glutamate-aspartate binding protein from Escherichia coli K12 strain W3092.,” *J Biol Chem*, vol. 250, no. 7, pp. 2574–80, Apr. 1975, [Online]. Available: http://www.ncbi.nlm.nih.gov/pubmed/1091635

[122] Y. Hu, C.-P. Fan, G. Fu, D. Zhu, Q. Jin, and D.-C. Wang, “Crystal structure of a glutamate/aspartate binding protein complexed with a glutamate molecule: structural basis of ligand specificity at atomic resolution.,” *J Mol Biol*, vol. 382, no. 1, pp. 99–111, Sep. 2008, doi: 10.1016/j.jmb.2008.06.091.

[123] J. D. Dattelbaum, “Analysis of allosteric signal transduction mechanisms in an engineered fluorescent maltose biosensor,” *Protein Science*, vol. 14, no. 2, pp. 284–291, Feb. 2005, doi: 10.1110/ps.041146005.

[124] Invitrogen, “Chapter 2. Thiol-Reactive Probes.,” in *The Molecular Probes ™ Handbook. A Guide to Fluorescent Probes and Labeling Technologies.*, 11th-th ed., Life Technologies, 2010, pp. 96–121. [Online]. Available: www.invitrogen.com/probes

[125] A. S. Klymchenko and Yves. Mely, “Chapter Two - Fluorescent Environment-Sensitive Dyes as Reporters of Biomolecular Interactions,” in *Fluorescence-Based Biosensors*, vol. 113, M. C. Morris, Ed. Academic Press, 2013, pp. 35–58. doi: https://doi.org/10.1016/B978-0-12-386932-6.00002-8.

[126] S. Fery-Forgues, J.-P. Fayet, and A. Lopez, “Drastic changes in the fluorescence properties of NBD probes with the polarity of the medium: involvement of a TICT state?,” *J Photochem Photobiol A Chem*, vol. 70, no. 3, pp. 229–243, 1993, doi: https://doi.org/10.1016/1010-6030(93)85048-D.

[127] Y. Mély and G. Duportail, *Fluorescent Methods to Study Biological Membranes*, vol. 13. Berlin: Springer, 2013. doi: 10.1007/978-3-642-33128-2.

[128] C. Jiang *et al.*, “NBD-based synthetic probes for sensing small molecules and proteins: design, sensing mechanisms and biological applications.,” *Chem Soc Rev*, vol. 50, no. 13, pp. 7436–7495, Jul. 2021, doi: 10.1039/d0cs01096k.

[129] H. v. Hsieh, D. B. Sherman, S. A. Andaluz, T. J. Amiss, and J. B. Pitner, “Fluorescence Resonance Energy Transfer Glucose Sensor from Site-Specific Dual Labeling of

Glucose/Galactose Binding Protein Using Ligand Protection," *J Diabetes Sci Technol*, vol. 6, no. 6, pp. 1286–1295, Nov. 2012, doi: 10.1177/193229681200600607.

[130] A. M. Powl, J. N. Wright, J. M. East, and A. G. Lee, "Identification of the hydrophobic thickness of a membrane protein using fluorescence spectroscopy: studies with the mechanosensitive channel MscL.," *Biochemistry*, vol. 44, no. 15, pp. 5713–21, Apr. 2005, doi: 10.1021/bi047338g.

[131] C. F. Chapman, Y. Liu, G. J. Sonek, and B. J. Tromberg, "The use of exogenous fluorescent probes for temperature measurements in single living cells.," *Photochem Photobiol*, vol. 62, no. 3, pp. 416–25, Sep. 1995, doi: 10.1111/j.1751-1097.1995.tb02362.x.

[132] M. Karplus and G. A. Petsko, "Molecular dynamics simulations in biology.," *Nature*, vol. 347, no. 6294, pp. 631–9, Oct. 1990, doi: 10.1038/347631a0.

[133] H. Dana *et al.*, "High-performance calcium sensors for imaging activity in neuronal populations and microcompartments.," *Nat Methods*, vol. 16, no. 7, pp. 649–657, Jul. 2019, doi: 10.1038/s41592-019-0435-6.

[134] R. H. Newman, M. D. Fosbrink, and J. Zhang, "Genetically encodable fluorescent biosensors for tracking signaling dynamics in living cells.," *Chem Rev*, vol. 111, no. 5, pp. 3614–66, May 2011, doi: 10.1021/cr100002u.

[135] E. C. Greenwald, S. Mehta, and J. Zhang, "Genetically Encoded Fluorescent Biosensors Illuminate the Spatiotemporal Regulation of Signaling Networks.," *Chem Rev*, vol. 118, no. 24, pp. 11707–11794, Dec. 2018, doi: 10.1021/acs.chemrev.8b00333.

[136] O. M. H. Salo-Ahen *et al.*, "Molecular Dynamics Simulations in Drug Discovery and Pharmaceutical Development," *Processes*, vol. 9, no. 1, p. 71, Dec. 2020, doi: 10.3390/pr9010071.

[137] J. A. McCammon, B. R. Gelin, and M. Karplus, "Dynamics of folded proteins.," *Nature*, vol. 267, no. 5612, pp. 585–90, Jun. 1977, doi: 10.1038/267585a0.

[138] M. Karplus and J. A. McCammon, "Molecular dynamics simulations of biomolecules.," *Nat Struct Biol*, vol. 9, no. 9, pp. 646–52, Sep. 2002, doi: 10.1038/nsb0902-646.

[139] W. F. van Gunsteren and H. J. C. Berendsen, "Computer Simulation of Molecular Dynamics: Methodology, Applications, and Perspectives in Chemistry," *Angewandte Chemie International Edition in English*, vol. 29, no. 9, pp. 992–1023, Sep. 1990, doi: 10.1002/anie.199009921.

[140] J. M. Walker, *Biomolecular Simulations*, 1st ed., vol. 924. Totowa, NJ: Humana Press, 2013. doi: 10.1007/978-1-62703-017-5.

[141] L. Verlet, "Computer 'Experiments' on Classical Fluids. I. Thermodynamical Properties of Lennard-Jones Molecules," *Physical Review*, vol. 159, no. 1, pp. 98–103, Jul. 1967, doi: 10.1103/PhysRev.159.98.

[142] W. HOCKNEY R., "The potential calculation and some applications," *Methods Comput. Phys.*, vol. 9, p. 136, 1970, Accessed: Jan. 03, 2023. [Online]. Available: https://cir.nii.ac.jp/crid/1570572699951074304.bib?lang=en

[143] A. R. Leach, *Molecular Modelling. Principles and Applications.*, Second. Prentice Hall, 2001.

[144] P. Allen M and J. Tildesley D, *Computer Simulations of Liquids*. New York: Oxford University Press, 1989.

[145] M. J. Abraham *et al.*, "GROMACS: High performance molecular simulations through multi-level parallelism from laptops to supercomputers," *SoftwareX*, vol. 1–2, pp. 19–25, Sep. 2015, doi: 10.1016/j.softx.2015.06.001.

[146] K. Lindorff-Larsen *et al.*, "Improved side-chain torsion potentials for the Amber ff99SB protein force field.," *Proteins*, vol. 78, no. 8, pp. 1950–8, Jun. 2010, doi: 10.1002/prot.22711.

[147] I. S. Joung and T. E. Cheatham, "Determination of alkali and halide monovalent ion parameters for use in explicitly solvated biomolecular simulations.," *J Phys Chem B*, vol. 112, no. 30, pp. 9020–41, Jul. 2008, doi: 10.1021/jp8001614.

[148] A. H. C. Horn, "A consistent force field parameter set for zwitterionic amino acid residues.," *J Mol Model*, vol. 20, no. 11, p. 2478, Nov. 2014, doi: 10.1007/s00894-014-2478-z.

[149] H. J. C. Berendsen, J. R. Grigera, and T. P. Straatsma, "The missing term in effective pair potentials," *J Phys Chem*, vol. 91, no. 24, pp. 6269–6271, Nov. 1987, doi: 10.1021/j100308a038.

[150] R. Briones, C. Blau, C. Kutzner, B. L. de Groot, and C. Aponte-Santamaría, "GROmaps: A GROMACS-Based Toolset to Analyze Density Maps Derived from Molecular Dynamics Simulations.," *Biophys J*, vol. 116, no. 1, pp. 4–11, Jan. 2019, doi: 10.1016/j.bpj.2018.11.3126.

[151] J. C. Meza, "Steepest Descent," *WIREs Comput. Stat.*, vol. 2, no. 6, pp. 719–722, Nov. 2010, doi: 10.1002/wics.117.

[152] G. Bussi, D. Donadio, and M. Parrinello, “Canonical sampling through velocity rescaling.,” *J Chem Phys*, vol. 126, no. 1, p. 014101, Jan. 2007, doi: 10.1063/1.2408420.

[153] H. J. C. Berendsen, J. P. M. Postma, W. F. van Gunsteren, A. DiNola, and J. R. Haak, “Molecular dynamics with coupling to an external bath,” *J Chem Phys*, vol. 81, no. 8, pp. 3684–3690, Oct. 1984, doi: 10.1063/1.448118.

[154] D. J. Evans and G. P. Morriss, “The isothermal/isobaric molecular dynamics ensemble,” *Phys Lett A*, vol. 98, no. 8–9, pp. 433–436, Nov. 1983, doi: 10.1016/0375-9601(83)90256-6.

[155] M. Parrinello and A. Rahman, “Polymorphic transitions in single crystals: A new molecular dynamics method,” *J Appl Phys*, vol. 52, no. 12, pp. 7182–7190, Dec. 1981, doi: 10.1063/1.328693.

[156] T. Darden, L. Perera, L. Li, and L. Pedersen, “New tricks for modelers from the crystallography toolkit: the particle mesh Ewald algorithm and its use in nucleic acid simulations.,” *Structure*, vol. 7, no. 3, pp. R55-60, Mar. 1999, doi: 10.1016/s0969-2126(99)80033-1.

[157] M. Aldeghi, B. L. de Groot, and V. Gapsys, “Accurate Calculation of Free Energy Changes upon Amino Acid Mutation.,” *Methods Mol Biol*, vol. 1851, pp. 19–47, 2019, doi: 10.1007/978-1-4939-8736-8_2.

[158] V. Gapsys, S. Michielssens, D. Seeliger, and B. L. de Groot, “pmx: Automated protein structure and topology generation for alchemical perturbations.,” *J Comput Chem*, vol. 36, no. 5, pp. 348–54, Feb. 2015, doi: 10.1002/jcc.23804.

[159] V. Gapsys, S. Michielssens, J. H. Peters, B. L. de Groot, and H. Leonov, “Calculation of Binding Free Energies,” in *Molecular Modelling of Proteins.*, A. Kukol, Ed. Humana Press, 2015, pp. 173–209. doi: 10.1007/978-1-4939-1465-4_9.

[160] M. Goette and H. Grubmüller, “Accuracy and convergence of free energy differences calculated from nonequilibrium switching processes.,” *J Comput Chem*, vol. 30, no. 3, pp. 447–56, Feb. 2009, doi: 10.1002/jcc.21073.

[161] G. E. Crooks, “Nonequilibrium Measurements of Free Energy Differences for Microscopically Reversible Markovian Systems.,” *J Stat Phys*, vol. 90, no. 5/6, pp. 1481–1487, 1998, doi: 10.1023/A:1023208217925.

[162] HHU, “Ligation calculator.” http://www.insilico.uni-duesseldorf.de/Lig_Input.html (accessed Jan. 05, 2023).

[163] Thermo Fischer, “Thiol-Reactive Probe Labeling Protocol.,” Apr. 10, 2006.

[164] J. Lakowicz, *Principles of Fluorescence Spectroscopy*, 2nd ed. Boston, MA: Springer US, 2006. doi: 10.1007/978-0-387-46312-4.

[165] H. HORIBA Jobin, "A practical guide to time-resolved luminescence lifetime determination using dedicated Time-Correlated Single-Photon Counting systems. A practical guide to time-resolved luminescence lifetime determination using dedicated Time-Correlated Single-Photon Counting systems," Glasgow.

[166] J. N. Weiss, "The Hill equation revisited: uses and misuses.," *FASEB J*, vol. 11, no. 11, pp. 835–41, Sep. 1997, [Online]. Available: http://www.ncbi.nlm.nih.gov/pubmed/9285481

[167] Edinburgh Instruments, *Lifetime measurements on FS5-MCS. User Guide.*, Issue 2.

[168] C. Alleva, "Role of extracellular gate in cation coupling in the glutamate transporter family.," Ph.D, Heinrich-Heine-University Düsseldorf, Jülich, 2020.

[169] A. D. Vogt and E. di Cera, "Conformational selection or induced fit? A critical appraisal of the kinetic mechanism.," *Biochemistry*, vol. 51, no. 30, pp. 5894–902, Jul. 2012, doi: 10.1021/bi3006913.

[170] F. Paul and T. R. Weikl, "How to Distinguish Conformational Selection and Induced Fit Based on Chemical Relaxation Rates.," *PLoS Comput Biol*, vol. 12, no. 9, p. e1005067, Sep. 2016, doi: 10.1371/journal.pcbi.1005067.

[171] J. R. Lakowicz, "Time-Domain Lifetime Measurements," in *Principles of Fluorescence Spectroscopy*, 2nd ed., J. R. Lakowicz, Ed. Boston, MA: Springer US, 2006. doi: 10.1007/978-0-387-46312-4.

[172] W. Becker, *Advanced Time-Correlated Single Photon Counting Techniques*, vol. 81. Berlin, Heidelberg: Springer Berlin Heidelberg, 2005. doi: 10.1007/3-540-28882-1.

[173] M. Engels, "Intracellular chloride concentrations in glial cells under normal or pathological conditions.," Ph.D, Heinrich-Heine-University Düsseldorf, Jülich, 2021.

[174] W. Humphrey, A. Dalke, and K. Schulten, "VMD: visual molecular dynamics.," *J Mol Graph*, vol. 14, no. 1, pp. 33–8, 27–8, Feb. 1996, doi: 10.1016/0263-7855(96)00018-5.

[175] L. Schrödinger, "The PyMOL Molecular Graphics System, Version 1.8." Nov. 2015.

[176] S. van der Walt, S. C. Colbert, and G. Varoquaux, "The NumPy Array: A Structure for Efficient Numerical Computation," *Comput Sci Eng*, vol. 13, no. 2, pp. 22–30, 2011, doi: 10.1109/MCSE.2011.37.

[177] P. Virtanen *et al.*, "SciPy 1.0: fundamental algorithms for scientific computing in Python," *Nat Methods*, vol. 17, no. 3, pp. 261–272, Mar. 2020, doi: 10.1038/s41592-019-0686-2.

[178] M. Waskom, O. Botvinnik, D. O'Kane, and P. Hobson, "Mwaskom/Seaborn: v0.8.1(September 2017)." Zenodo., 2017.

[179] J. D. Hunter, "Matplotlib: A 2D Graphics Environment," *Comput Sci Eng*, vol. 9, no. 3, pp. 90–95, 2007, doi: 10.1109/MCSE.2007.55.

[180] J. V. Nadler, "Aspartate release and signalling in the hippocampus.," *Neurochem Res*, vol. 36, no. 4, pp. 668–76, Apr. 2011, doi: 10.1007/s11064-010-0291-3.

[181] D. Ewers, T. Becher, J.-P. Machtens, I. Weyand, and C. Fahlke, "Induced fit substrate binding to an archeal glutamate transporter homologue.," *Proc Natl Acad Sci U S A*, vol. 110, no. 30, pp. 12486–91, Jul. 2013, doi: 10.1073/pnas.1300772110.

[182] C. Dulla, H. Tani, S. Okumoto, W. B. Frommer, R. J. Reimer, and J. R. Huguenard, "Imaging of glutamate in brain slices using FRET sensors.," *J Neurosci Methods*, vol. 168, no. 2, pp. 306–19, Mar. 2008, doi: 10.1016/j.jneumeth.2007.10.017.

[183] S. Gowrisankaran and I. Milosevic, "Regulation of synaptic vesicle acidification at the neuronal synapse.," *IUBMB Life*, vol. 72, no. 4, pp. 568–576, Apr. 2020, doi: 10.1002/iub.2235.

[184] S. Sakamoto, J. M. M. Caaveiro, E. Sano, Y. Tanaka, M. Kudou, and K. Tsumoto, "Contributions of interfacial residues of human Interleukin15 to the specificity and affinity for its private alpha-receptor.," *J Mol Biol*, vol. 389, no. 5, pp. 880–94, Jun. 2009, doi: 10.1016/j.jmb.2009.04.050.

[185] S. Lin and W. S. Struve, "Time-resolved fluorescence of nitrobenzoxadiazole-aminohexanoic acid: effect of intermolecular hydrogen-bonding on non-radiative decay.," *Photochem Photobiol*, vol. 54, no. 3, pp. 361–5, Sep. 1991, doi: 10.1111/j.1751-1097.1991.tb02028.x.

[186] L. A. Shepard *et al.*, "Identification of a membrane-spanning domain of the thiol-activated pore-forming toxin Clostridium perfringens perfringolysin O: an alpha-helical to beta-sheet transition identified by fluorescence spectroscopy.," *Biochemistry*, vol. 37, no. 41, pp. 14563–74, Oct. 1998, doi: 10.1021/bi981452f.

[187] P. Avouris, W. M. Gelbart, and M. A. El-Sayed, "Nonradiative electronic relaxation under collision-free conditions," *Chem Rev*, vol. 77, no. 6, pp. 793–833, Dec. 1977, doi: 10.1021/cr60310a002.

[188] S. R. Flom and P. F. Barbara, "Proton transfer and hydrogen bonding in the internal conversion of S1 anthraquinones," *J Phys Chem*, vol. 89, no. 21, pp. 4489–4494, Oct. 1985, doi: 10.1021/j100267a017.

[189] P. F. Barbara, P. K. Walsh, and L. E. Brus, “Picosecond kinetic and vibrationally resolved spectroscopic studies of intramolecular excited-state hydrogen atom transfer,” *J Phys Chem*, vol. 93, no. 1, pp. 29–34, Jan. 1989, doi: 10.1021/j100338a011.

[190] D. Dimitrov, H. Takagi, L. Guillaud, N. Saitoh, K. Eguchi, and T. Takahashi, “Reconstitution of Giant Mammalian Synapses in Culture for Molecular Functional and Imaging Studies.,” *J Neurosci*, vol. 36, no. 12, pp. 3600–10, Mar. 2016, doi: 10.1523/JNEUROSCI.3869-15.2016.

[191] H. von Gersdorff and J. G. G. Borst, “Short-term plasticity at the calyx of Held.,” *Nat Rev Neurosci*, vol. 3, no. 1, pp. 53–64, Jan. 2002, doi: 10.1038/nrn705.

[192] G. S. Loving, M. Sainlos, and B. Imperiali, “Monitoring protein interactions and dynamics with solvatochromic fluorophores,” *Trends Biotechnol*, vol. 28, no. 2, pp. 73–83, Feb. 2010, doi: 10.1016/j.tibtech.2009.11.002.

[193] P. Nalbant, L. Hodgson, V. Kraynov, A. Toutchkine, and K. M. Hahn, “Activation of Endogenous Cdc42 Visualized in Living Cells,” *Science (1979)*, vol. 305, no. 5690, pp. 1615–1619, Sep. 2004, doi: 10.1126/science.1100367.

[194] N. Helassa, B. Podor, A. Fine, and K. Török, “Design and mechanistic insight into ultrafast calcium indicators for monitoring intracellular calcium dynamics,” *Sci Rep*, vol. 6, Dec. 2016, doi: 10.1038/srep38276.

[195] R. Dingledine and J. McBain C, “Glutamate and Aspartate Are the Major Excitatory Transmitters in the Brain.,” in *Basic Neurochemistry: Molecular, Cellular and Medical Aspects.*, 6th-th ed., J. Siegel G, W. Agranoff B, and W. Albers R, Eds. Philadelphia: Lippincott-Raven, 1999. Accessed: Jan. 04, 2023. [Online]. Available: https://www.ncbi.nlm.nih.gov/books/NBK20426/

[196] K. N. Westlund and W. D. Willis, “Pain System,” in *The Rat Nervous System*, 4th-th ed., Academic Press, 2015, pp. 703–731. doi: 10.1016/B978-0-12-374245-2.00025-5.

[197] A. Bogorodskiy *et al.*, “Accessing Mitochondrial Protein Import in Living Cells by Protein Microinjection,” *Front Cell Dev Biol*, vol. 9, Jul. 2021, doi: 10.3389/fcell.2021.698658.

Acknowledgments

If I hadn't been surrounded by some incredible people, who in all their actions have nudged and supported me along my way, I could have not done anything of what I did.

Firstly, I would like to acknowledge my thesis supervisor Prof. Dr. Christoph Fahlke, to whom I am grateful for giving me the opportunity to jump into the adorable world of biology and to work in his scientific group in the institute of Biological Information Processes, Molecular and Cellular Physiology (IBI-1).

My special thanks to Dr. Claudia Alleva for her invaluable support, knowledge and help during the moment when I was lost on my scientific way.

I would express my deep gratitude to all the researchers and stuff from the IBI-1 who spent hours for discussions, support and advise me every time I needed, Dr. Thomas Gensch, Prof. Dr. Patricia Hidalgo, Prof. Dr. Jan-Philipp Machtens, Meike Berndt, Arne Franzen, Nadine Jordan, Anita Eckert and Sia Perousakis.

With many thanks to my colleagues Andrei, Andrii, Assala, Bassam, Bart, Bettina, Carène, Claudia, Felix, Francisco, Juan, Markus, Miriam, Nataliia, Piersilvio, Victor, Yulia with whom I shared most of the great time during my Ph.D. Our discussions during the coffee breaks, scientific disputes and weird jokes are underrated.

To my friends Liudmyla, Maryna, Nataliya and Anastasiia, for our long-distance friendship and memories about the wonderful time that we have spent together.

Fran, words cannot express my gratitude for the support, understanding and patience you have shown. It gave me strength when I needed it the most.

Finally, I would like to thank my parents Raisa and Iurii Ryndia. Their personal example and belief in me have kept my spirit strong and motivation high during my whole life. I am grateful to my brother Maksym Ryndia, the first scientist and the greatest motivator in my life, who always help me not to give up and move on.

Схиляю голову перед українським народом за мужність і єдність в боротьбі за незалежність! Слава Україні!

Eidesstattliche Versicherung

Ich versichere an Eides Statt, dass die Dissertation von mir selbstständig und ohne unzulässige fremde Hilfe unter Beachtung der „Grundsätze zur Sicherung guter wissenschaftlicher Praxis an der Heinrich-Heine-Universität Düsseldorf“ erstellt worden ist.

Ort, Datum	Kateryna Ryndia